DOCTORAATSPROEFSCHRIFT

2007 | Faculteit Wetenschappen

Electrical Characterisation of 2,5-Substituted Poly (*p*-Phenylene Vinylene) Derivatives and Their Application in Organic Bulk Heterojunction Solar Cells

Proefschrift voorgelegd tot het behalen van de graad van
Doctor in de Wetenschappen, richting natuurkunde, te verdedigen door:

Martin BRESELGE

Promotor: Prof. dr. Jean V. Manca
Copromotoren: Prof. dr. Patrick Wagner
Prof. dr. Dirk Vanderzande

universiteit hasselt

imec

INSTITUUT VOOR
MATERIAALONDERZOEK

D/2007/2451/61

Nederlandse Samenvatting

De huidige energieopwekking is hoofdzakelijk gebaseerd op fossiele brandstoffen. Momenteel wordt er nog steeds meer steenkool, aardolie en aardgas ontdekt, als er wordt verbruikt. Maar dit verandert niets aan het feit, dat de fossiele brandstofreserves vroeger of later opgebruikt zullen zijn. Hetzelfde argument is op lange termijn ook van toepassing op kernenergie. Onafhankelijk van de beschikbaarheid van fossiele brandstoffen en kernbrandstoffen leidt de tegenwoordige praktijk van de energieproductie tot verdere problemen. Twee van de belangrijkste aspecten zijn de milieuvervuiling door verbrandingsgassen en radioactief afval en de politieke conflicten die veroorzaakt worden door het verschaffen van toegang tot nieuwe brandstofreserves (bijvoorbeeld de Golfoorlogen in Iran, Irak en Koeweit). In het geval van de kernenergie stelt zich de vraag of en hoe het veilige gebruik van kernenergie gegarandeerd kan worden, om de misbruik van kerntechnologie voor kernwapens te voorkomen (bijvoorbeeld momentele situatie in Iran en Noord-Korea).

Propere en veilige alternatieven zijn duurzame energiebronnen. Terwijl waterkracht en windenergie al lang worden gebruikt, worden fotovoltaïsche zonnecellen eerst sinds het begin van de jaren 1980 voor de elektrische energieopwekking toegepast. Sindsdien werd het rendement van zonnecellen continu verbeterd. Helaas is zonne-energie nog steeds duur. Dit word vooral veroorzaakt door de hoge materiaalkosten van de silicium-wafers en de hoge productiekosten (gebruik van hoge temperatuurstappen en een cleanroom). Zonnecellen die op zogenaamde organische halfgeleiders gebaseerd zijn, beloven een goedkoper alternatief.

Organische halfgeleiders zijn al ~50 jaar bekend. Nochtans werd er weinig belangstelling getoond om deze materialen voor zonnecellen of andere devices te gebruiken. De meeste toepassingen vereisen betere elektrische eigenschappen en een langere levensduur. Slechts de laatste ~20 jaren werden organische halfgeleiders aantrekkelijker voor praktische toepassingen, omdat de vooruitgang in het onderzoek tot verbeterde eigenschappen heeft geleid. Ondertussen bestaan er commerciële toepassingen binnen het domein van displays gebaseerd op organische LEDs. Ook binnen het domein van organische zonnecellen ging het vooruit. Het rendement werd duidelijk

verhoogd (momenteel tussen 5% en 6%) en nadert beetje bij beetje het doel van 10%, dat belangrijk is voor economische toepassingen.

De zonnecellen in dit proefschrift zijn gebaseerd op geconjugeerde polymeren en PCBM (een fullereen-derivaat). Halfgeleidende polymeren bieden de mogelijkheid de materiaalkosten te verlagen. Bovendien zijn zij oplosbaar in verschillende solventen. Dat betekent, deze materialen kunnen aangebracht worden m.b.v. goedkope printtechnieken. Daarenboven zijn polymeren plooibaar en kunnen op deze manier naar believen op verschillende gevormde oppervlakten aangebracht worden.

Om het rendement van organische zonnecellen verder te verbeteren, is het belangrijk te begrijpen hoe zij werken. Voor de absorptie van het zonlicht zijn enkel de optische eigenschappen van het polymeer belangrijk. Zodra het licht geabsorbeerd is en de optische energie omgezet is in elektrische energie, bepalen de elektrische eigenschappen van de twee materialen het ladingstransport naar de contacten. In tegenstelling tot anorganische halfgeleiders, die gewoonlijk kristallijn zijn, zijn geconjugeerde polymeren amorf. Dat betekent dat de lange polymeerketens door elkaar liggen. Dus is het ladingstransport in polymeren chaotisch, terwijl in kristallijne halfgeleiders de ladingen zich in zogenaamde banden bewegen. Dit chaotische ladingstransport wordt beschreven door een „hopping"-proces. Dit „hopping"-proces resulteert in een relatief ingewikkelde mathematische beschrijving en een veel lagere ladingsmobiliteit dan voor kristallijne halfgeleiders.

Dit proefschrift houdt zich dan ook bezig met de elektrische karakterisatie van een selectie van nieuwe halfgeleidende polymeren. Meerdere meet- en analysemethoden werden op een aantal PPV-derivaten toegepast. De verschillende meetresultaten werden ten opzichte van de gebruikte methode geïnterpreteerd en in verband gebracht met verschillende materiaaleigenschappen. Er werd aangetoond, dat de klassieke vergelijkingen i.v.m. elektrisch transport die voor anorganische halfgeleiders bekend zijn, niet noodzakelijk ook geschikt zijn voor organische halfgeleiders. Om een ladingsmobiliteit te bepalen die alleen van de materiaaleigenschappen afhangt en niet van de toegepaste methode, is het belangrijk met verschillende effecten rekening te houden. De belangrijkste van deze effecten zijn de

veldafhankelijke mobiliteit, de buitengewoon hoge contactweerstand en in FETs (veldeffect transistoren) de afhankelijkheid van de mobiliteit van de gate-spanning. Alleen als rekening met dezen effecten gehouden wordt, is het mogelijk de resultaten van verschillende experimenten te vergelijken.

Een belangrijk aspect voor de keuze van de opgemeten halfgeleiders was, dat zij gebaseerd zijn op het zelfde geconjugeerde polymeer (PPV); alleen de zijketens waren verschillend en leidden tot een verschillende polariteit. De polariteit is een belangrijke parameter voor de oplosbaarheid van een materiaal. Het referentiemateriaal OC_1C_{10}-PPV is relatief apolair. Dat heeft tot gevolg, dat apolaire solventen zoals chlorobenzeen of tolueen moeten worden gebruikt. Deze solventen zijn nochtans schadelijk voor het milieu. Milieuvriendelijke solventen zoals alcoholen of water zijn heel polair, dat betekent dat zij alleen geschikt zijn om polaire materialen op te lossen. Vandaar is het interessant de apolaire zijketens van OC_1C_{10}-PPV door polaire zijketens te vervangen. In het kader van het IWT-SBO-project "Nanosolar" werd in dit proefschrift aangetoond, dat de toename van de polariteit die van de chemische struktuur van de zijketens verwacht werd inderdaad plaatsvindt. Verder werd onderzocht hoe de verhoogde polariteit en de resulterende dipool-dipool-interactie de eigenschappen van het polymeer beïnvloeden. Het effect van de polariteit op de „ordering" van de polymeren was te klein om een verschil tijdens de metingen te zien. Andere eigenschappen zoals de lengte van de polymeerketens hebben blijkbaar een grotere invloed dan de polariteit. Ook op de ladingsmobiliteit had de polariteit geen significante invloed. Enkel een verandering van de optische absorptie werd bevestigd. Blijkbaar heeft de toegenomen interactie tussen nabijgelegen polymeren en tussen de zijketens en de ruggengraat van het polymeer een effect op de absorptie. Het meest polaire materiaal (diPEO-PPV) heeft een maximale absorptie die bijna twee keer groter is dan voor OC_1C_{10}-PVV. Dit betekent natuurlijk voor zonnecellen, dat een dunne laag diPEO-PPV evenveel licht absorbeert als een dikke laag OC_1C_{10}-PPV.

Door het grote verschil van de polariteit van de polymeren, gedragen mengsels van een polymeer en een fullereen-derivaat zich ook duidelijk verschillend. Deze mengsels zijn nodig om de zogenaamde „bulk heterojunction" zonnecellen te fabriceren, die voorwerp van dit proefschrift

waren. Bulk heterojunction zonnecellen gebruiken een mengsel van een donor- en een acceptormateriaal. Telkens één van de boven beschreven polymeren wordt als donormateriaal gebruikt en één fullereen-derivaat als acceptormateriaal. Voor een goede zonnecel is het belangrijk dat er een fasescheiding tijdens de fabricatie van de film plaatsvindt (typisch ~10nm). Dat betekent, dat er in de film fullereenrijke gebieden ontstaan. De grenslaag tussen deze fullereen-clusters en de polymeermatrix is nodig om het elektron en het „gat" die door de absorptie van het zonlicht ontstaan zijn, te splitsen. Voor een effektive splitsing van alle elektron-gat-paren is een grote interactieoppervlakte nodig. Bovendien moeten de fullereen-clusters een percolatienetwerk vormen omdat anders de elektronen de kathode niet kunnen bereiken. Voor de klassieke combinatie van OC_1C_{10}-PPV en PCBM opgelost in chlorobenzeen, wordt de ideale morfologie voor een verhouding van 1:4 bereikt. Verandert nu de polariteit van het polymeer, bijvoorbeeld door het vervangen van de bestaande zijketens door meer polaire zijketens, verandert natuurlijk ook de ideale verhouding. Voor bepaalde materiaalcombinaties treedt er soms helemaal geen fasescheiding op. Er bestaat natuurlijk de mogelijkheid een ander solvent te gebruiken of andere parameters te veranderen. In dit proefschrift werd de invloed van de polariteit van het polymeer, het fullereen-derivaat en het solvent onderzocht. De morfologie was heel gevoelig voor de polariteit van de opgeloste materialen, maar niet voor de polariteit van het solvent. Een veel belangrijkere parameter is blijkbaar het kookpunt van het solvent. Het kookpunt beïnvloedt hoe snel het solvent verdampt, d.w.z. hoeveel tijd er beschikbaar is om een goede morfologie te vormen. Solventen met gelijkaardig kookpunt zoals chlorobenzeen (181°C), m-dichlorobenzeen (173°C) en o-dichlorobenzeen (180°C) leidden tot een vergelijkbare morfologie. De resultaten voor PEO-PPV waren bijzonder interessant voor zonnecellen. Een mengsel van PEO-PPV:PCBM opgelost in chlorobenzeen vertoonde een ideale morfologie al voor een verhouding van 1:1. Omdat vooral het polymeer de absorptie van de zonnecel bepaalt is het natuurlijk belangrijk zo veel polymeer en zo weinig PCBM als mogelijk te gebruiken. Dus als OC_1C_{10}-PPV door PEO-PPV word vervangen, stijgt de polymeerconcentratie van 20% op 50% voor een film met ideale morfologie.

De resultaten van de elektrische karakterisatie van de polymeren en het morfologieonderzoek leidden tot de conclusie dat de beste zonnecellen voor

een 1:1 verhouding van PEO-PPV en PCBM in chlorobenzeen te verwachten zijn. Dit werd dan ook voor de polaire polymeren experimenteel geverifieërd. De beste PEO-PPV-gebaseerde zonnecel vertoont een kortsluitstroom van dezelfde grootteorde als voor de referentiezonnecel (OC_1C_{10}-PPV:PCBM 1:4), maar een kleinere open spanning en een lagere fill factor. Door middel van simulaties werd bevestigt, dat één oorzaak de kleinere effektieve band gap van het PEO-PPV:PCBM mengsel was. De kleinere effektieve band gap leidt tot een kleinere open ketenspanning V_{OC}. Verder heeft de grote serieweerstand een negatieve invloed op de fill factor van de zonnecellen. Een reductie van de serieweerstand is derhalve cruciaal om de PEO-PPV-gebaseerde zonnecellen te verbeteren. Samenvattend, het is aangetoond dat het aanbrengen van polaire zijketens de diëlektrische permittiviteit van de polymeren doet toenemen, met behoud van de vereiste elektro-optische eigenschappen voor zonnecel-toepassingen. Dit is een belangrijke stap voor de verdere ontwikkeling van organische zonnecellen op basis van milieuvriendlijken solvente.

1. Introduction

Organic semiconductors have been studied since the late 1950s and early 1960s, e.g. organic crystals consisting of naphthalene or anthracene exhibited electroluminescence and photoconductivity [1-4]. These materials were difficult to process, rendering them uninteresting for potential applications. Consequently, organic semiconductors were neglected for a long time, also because of their inferior electric properties and the lack of stability compared with inorganic crystalline materials. In 1977 Shirakawa, MacDiarmid and Heeger discovered that doped polyacetylene becomes highly conductive [5][1]. In the 1980s it was demonstrated that conjugated polymers like poly(*p*-phenylene vinylene) exhibited electroluminescence [6]. Ever since much effort was put in the increase of the charge carrier mobility (see left hand side figure 1.1) and the improvement of device parameters, like the on-off ratio and driving voltage of transistors [7-9]. In the last twenty years, electronic devices based on organic semiconductors have attracted more and more interest. The applications of organic semiconductors range from field-effect transistors [10-33] over organic light-emitting diodes (OLED) [6-9, 34-52] for displays and illumination, to organic solar cells [53-70]. Recently the first commercial products have become available in form of flat panel displays using OLEDs instead of liquid crystals (e.g. Kodak [71], Philips [72], Samsung [73], Sony [74], etc.).

Organic semiconductors offer several advantages over traditional inorganic semiconductors. Low material costs and easy processing, without the need for cleanroom facilities and high-temperature steps, are promising an economic production. Further large area fabrication by role-to-role printing techniques offer the high throughput necessary to produce low-cost electronics and solar cells. Thereby a variety of substrates can be used like traditional wafers, glass, plastic and even paper. Especially the use of flexible substrates facilitates new markets for electronics and solar cells.

[1] Nobel prize in chemistry in 2000

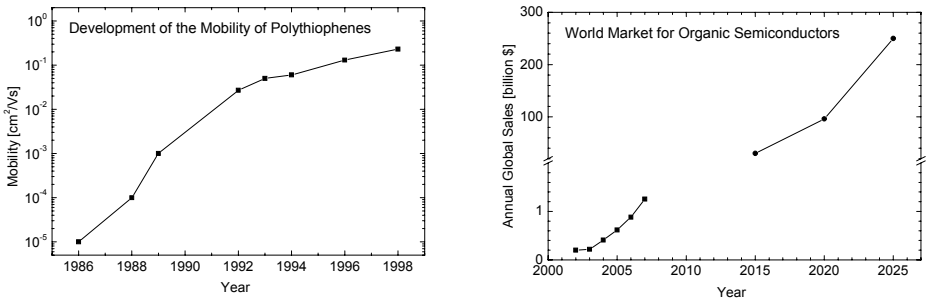

Figure 1.1:
Development of the charge carrier mobility of polythiophenes (left hand side; data was taken from [11, 12, 75]) and the annual global sales of organic semiconductors (right hand side) in the last five years [76] and as projected for the future [77].

The great potential of organic semiconductors and the dynamic development in recent years is reflected in the constantly growing market. From 2001 to 2007, the annual global sales increased from ~200 million US dollars to more than 1.2 billion US dollars [76]. The projection for the next ~20 years suggests, that organic semiconductors will soon become a multibillion dollar industry with annual global sales breaking the 100 billion US dollar barrier around the year 2020 [77]. As mentioned earlier, semiconductors cannot only replace inorganic materials in traditional applications, but they can also create entirely new markets. Although the most important application will be OLEDs in lighting and display technologies, organic solar cells are estimated to contribute ~15% to the annual global market of organic semiconductors by 2020 [77].

1.1. Motivation and Outline

In order to develop electrical devices based on organic semiconductors, a better understanding of the charge carrier transport is crucial. Since most organic semiconductors are amorphous, their conduction mechanism is more complex than for inorganic crystalline materials (see section 1.4). Consequently, the electrical properties of organic semiconductor are not

well-known. For identical materials, many different values can be found in literature. Differences in synthesis and device preparation explain the deviations only partly. In fact it is commonly assumed, that the employed measurement technique has a large influence on the results. This is not surprising since measurement techniques like time-of-flight measurements [78-80], field-effect transistor measurements [7, 14, 16-24, 26, 30, 81-90], Hall measurements [91, 92], etc. require different device geometries and thus effectively probe the material properties under different conditions.

The scope of this work is to characterise several novel poly(*p*-phenylene vinylene) (PPV) derivatives electrically with a variety of measurement techniques to gain a deeper insight how the extracted electrical material properties have to be interpreted and how they relate to the chemical properties of the polymers. One of the most preeminent chemical properties that are influenced by the substitution of side chains is the polarity of the polymer. Conventional PPV derivatives like OC_1C_{10}-PPV (see section 1.3) possess rather apolar side chains. Hence, the use of apolar solvents like toluene, chloroform, chlorobenzene, etc. These solvents are not environmentally friendly, making their substitution an eminent task. On the other hand, harmless solvents like alcohols or water are rather polar. There are several possible routes to make PPVs soluble in these solvents. The PPV derivatives studied in this work address this issue by the substitution of apolar side chains by more polar ones. The increased polarity ensures not only the solubility of the materials in the aforementioned solvents, but becomes of particular importance when blending the polymers with fullerene derivatives. Such blends are required for organic bulk heterojunction solar cells. Chapter 7 and 8 will deal with the morphology of such blends and their influence on the preparation of solar cells. However, the focus of the present work is the electrical characterisation of the pure polymers. In chapter 2 (field-effect transistor measurements), 3 (space-charge limited current measurements) and 4 (impedance spectroscopy) three measurement techniques are presented and the acquired measurement data is analysed by applying several different models. Further, in chapter 5 the electrooptical properties and the polarity of the polymers are studied. Finally, the diverse characterisation methods and results are compared and discussed in chapter 6.

In the remaining sections of this chapter, an introduction is given to organic semiconductors in general, the polymers studied in this work in specific and the immanent charge carrier transport in organic materials.

1.2. Organic Semiconductors

In order to understand the origin of conductivity in organic materials, a short introduction of the physical and chemical background is given in this section.

Very much like the orbitals in atoms, molecules have molecular orbitals, i.e. there are discrete energy levels for the electrons bound to the molecule. Since the most important element for organic compounds is carbon, the following explanation focuses on the case of carbon-carbon bonds (for more information about organic chemistry see [93]). The electronic configuration of a carbon atom is $1s^2 2s^2 2p^2$, with the four electrons of the second energy level governing the chemical behaviour of carbon. However, in carbon-carbon bonds the four electrons are hybridised, resulting in more stable, i.e. lower energy configurations. For the polymers subject to this work, the sp^3 hybridisation (single bond) and the sp^2 hybridisation (double bond) are of particular interest. For the sp^3 hybridisation, one 2s electron is promoted to the empty 2p orbital. The remaining 2s electron and the three 2p electrons are hybridised to four identical sp^3 orbitals. A single bond (σ bond) between two carbon atoms is realised by the overlap of two sp^3 orbitals.

In carbon-carbon double bonds the carbon atoms are in the sp^2 hybrid state, i.e. the 2s orbital hybridises with two 2p orbitals. The result is one remaining 2p orbital and three sp^2 orbitals. The three sp^2 orbitals lie in a plane, with the 2p orbital perpendicular to it. In a double bond one sp^2 orbital of each carbon atom overlaps to form a σ bond. The remaining sp^2 orbitals can bond to other atoms, e.g. hydrogen or carbon. The sides of the 2p orbitals of the two carbon atoms overlap too, to form a π bond. Thus, a double bond consists of a σ bond and a π bond.

The two sp^2 orbitals of the σ bond result in two molecular orbitals with different energy. The orbital with lower energy is denoted with σ (bonding), while the orbital with higher energy is called σ^* (anti-bonding). Correspondingly the p orbitals of the π bond result in the molecular orbitals π

and π*. A schematic drawing of the relative energy levels is given in figure 1.2 (left hand side). The arrows indicate the four electrons participating in a double bond, occupying the lowest possible energy levels. The highest occupied molecular orbital (HOMO) is the π orbital and the lowest unoccupied molecular orbital (LUMO) is the π* orbital.

In the polymers studied in this work the carbon atoms are bonded by alternating double and single bonds. These so-called conjugated double bonds do not behave independently. They are coupled electronically, since the p orbitals of two adjacent single-bonded carbon atoms partial overlap. This means that the π electron density is distributed over a large region within the molecule, i.e. it is delocalised. The delocalisation of π electrons is the origin of conduction in conjugated polymers.

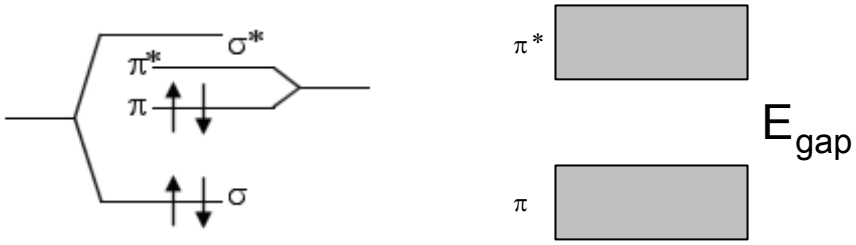

Figure 1.2:
Molecular orbitals of an isolated carbon-carbon double bond (left hand side) and energy bands resulting from split energy levels of a large number of p orbitals (right hand side).

As mentioned before, the molecular orbitals define discrete energy levels for the electrons. However when many atoms interact, the energy levels split. If the number of atoms becomes larger, the individual energy levels begin to form energy bands (right hand side of figure 1.2). The Peierls distortion ensures that at room temperature the resulting bands are separated by a band gap E_{gap} [94]. The two bands behave similar to the valence band and the conduction band in inorganic crystalline semiconductors. Therefore, the terminology of traditional semiconductor physics is often used for better

illustration. However, it is very important to remember that the charge carrier transport in organic semiconductors is of different nature. While in crystalline materials a true band transport is observed, amorphous organic semiconductors usually exhibit a hopping-like transport, which can change to a band-like transport at low temperatures [82]. Before giving a detailed introduction to the charge transport in organic semiconductors, the conjugated polymers employed in this work are briefly described.

1.3. Poly(*p*-Phenylene Vinylene) Derivatives

The conjugated polymers, which were studied in this work, are 2,5-substituted poly(*p*-phenylene vinylene) derivatives (PPVs). As a reference material poly[2-(3',7'-dimethyloctyloxy)-5-methoxy-1-4-phenylenevinylene] (OC_1C_{10}-PPV) was used[2]. The apolar OC_1C_{10}-PPV was compared to three novel PPV derivatives with $(CH_2CH_2O)_3CH_3$ (PEO) side chains. Two of the derivatives had one PEO side chain and either one short or one long alkyl side chain. The PPV with the short OC_1H_3 side chain was poly[2-methoxy-5-(triethoxymethoxy)-1,4-phenylene vinylene] called PEO-PPV. The one with the long OC_9H_{19} side chain was poly[2-(*n*-nonyloxy)-5-(triethoxymethoxy)-1-4-phenylene vinylene] called (PEO-OC_9)-PPV. The third PPV derivative with PEO side chains was the symmetrically substituted poly[2,5-bis-(triethoxymethoxy)-1-4-phenylene vinylene] called diPEO-PPV. A description of the synthesis of the PEOs can be found in [95, 96]. From the chemical structure (see figure 1.3), it is expected that the PEOs are more polar than OC_1C_{10}-PPV, because of the polar ether groups of the side chains. Conjugated polymers with higher polarity are particularly interesting because of the possibility to solubilise them in more polar solvents. Commonly used solvents like chlorobenzene, chloroform, etc. are not environmentally friendly and thus they have to be replaced by more sustainable chemicals before starting large-scale production. Alternative solvents would be alcohols or even water, which are more polar. Following the "like solves like" principle, it is therefore desirable to increase the polarity of the polymers.

[2] OC_1C_{10}-PPV was purchased from Covion

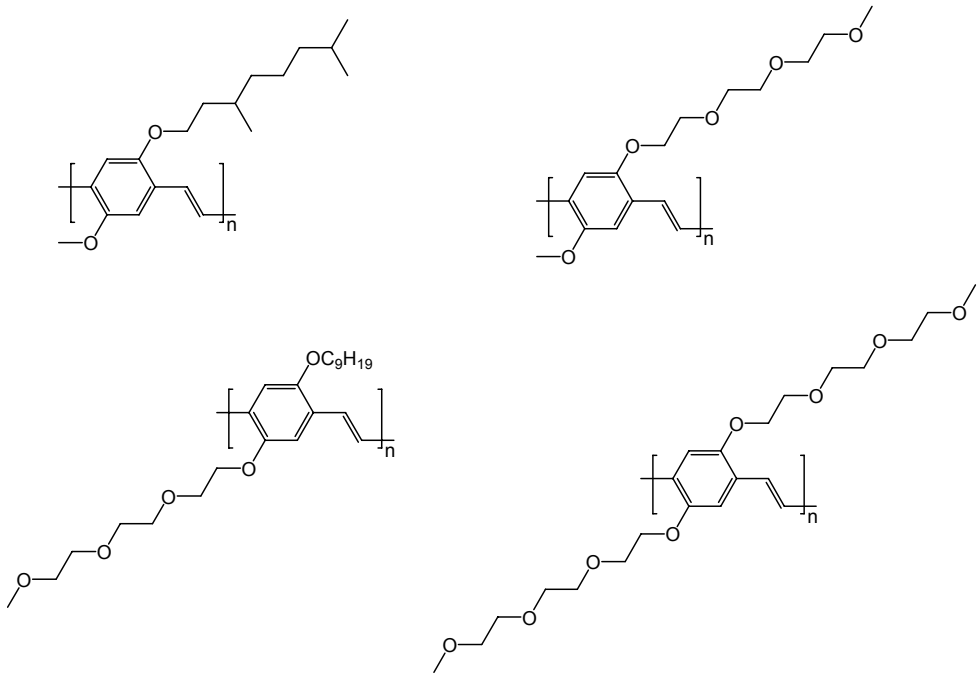

Figure 1.3:
Chemical structures of OC_1C_{10}-PPV (top left hand side), PEO-PPV (top right hand side), (PEO-OC_9)-PPV (bottom left hand side) and diPEO-PPV (bottom right hand side).

Table 1.1 lists several material properties of the studied PPVs as measured by the organic chemistry group of IMO[3]. The weight average molecular mass M_W and the numeric average molecular mass M_N were determined from gel permeation chromatography (GPC). The number of repeating units was calculated by dividing M_N by the molecular mass of one polymer unit. HOMO and LUMO levels were extracted from cyclic voltammetry. Finally, the optical band gap was calculated from absorbance measurements.

[3] Instituut voor Materiaalonderzoek, Diepenbeek, Belgium

Polymer	OC_1C_{10}-PPV	PEO-PPV	(PEO-OC_9)-PPV	diPEO-PPV
M_W [g/mol]	*915 700*	*637 617*	*134 301*	*1 311 950*
M_N [g/mol]	*75 900*	*162 804*	*19 489*	*452 398*
Polydispersity	*12.1*	*3.9*	*6.9*	*2.9*
No. of Units	*263*	*553*	*48*	*1061*
HOMO [eV]	*-5.32*	*-5.05*	*-5.13*	*-5.15*
LUMO [eV]	*-2.74*	*-2.93*	*-2.92*	*-2.97*
Electrochemical Band Gap [eV]	*2.58*	*2.12*	*2.21*	*2.18*
Optical Band Gap [eV]	*2.12*	*2.10*	*2.12*	*2.10*

Table 1.1:
Chemical and optical properties of the four PPV derivatives studied.

It is noted, that there is a large difference in molecular masses between the polymers. The commercially purchased OC_1C_{10}-PPV and diPEO-PPV have a weight average molecular mass of $\sim 10^6$g/mol, while especially (PEO-OC_9)-PPV has a significantly lower value ($\sim 10^5$g/mol). There is also a large difference in polydispersity values, ranging from ~3 for diPEO-PPV to ~12 for OC_1C_{10}-PPV. The large difference in molecular mass is also expressed by the average number of repeating polymer units, which is as low as ~50 for (PEO-OC_9)-PPV and as big as ~1060 for diPEO-PPV.

1.4. Charge Carrier Transport

As already mentioned in section 1.2 the charge carrier transport in amorphous organic semiconductors is a hopping process by nature. In this section a detailed introduction of the charge carrier transport and the theory behind is given.

In metals and traditional inorganic semiconductors, the strong bonding of

adjacent atoms and the long-range order leads to a delocalisation of the charge carriers over the entire crystal. Consequently, the conduction can be described by a band transport. The charge carriers are only hampered by impurities and imperfections in the crystal. At non-zero temperature, the interaction with phonons leads to additional impediment of the charges. Due to the weak van der Waals interaction between organic molecules, transport bands are very narrow and can be easily interrupted in disordered material [43, 82, 87]. Consequently, band-like transport is atypical for organic semiconductors. Instead, charge transport takes place as a hopping of either electrons from LUMO to LUMO level or holes from HOMO to HOMO level of spatially or energetically separated sites. Therefore, the effective charge carrier mobility (intermolecular transport) is orders of magnitude lower than the intrinsic one (intramolecular transport), which is governing the transport on one conjugated segment [97].

The hopping transport was found to be activated by the temperature T and the electric field E. Gill introduced an empirical equation for the charge carrier mobility μ(E, T) [98]:

$$\mu(E,T) = \mu_0 \cdot \exp\left[-\frac{\Delta}{k_B \cdot T} + B \cdot \left(\frac{1}{k_B \cdot T} - \frac{1}{k_B \cdot T_0} \right) \cdot \sqrt{E} \right] \qquad (1.1)$$

with the field-independent mobility μ_0, the zero-field activation energy Δ, the Boltzmann constant k_B and the characteristic parameters B and T_0 which describe the temperature dependence of the mobility. Although the equation describes the field dependence well, it does not explain the origin of such behaviour. In order to give a theoretical derivation the underlying process has to be observed more carefully. Figure 1.4 depicts the situation in an amorphous organic semiconductor. The edge of the valence band (HOMO) and the edge of the conduction band (LUMO) is not a sharp energy value. In fact, it is a distribution of energy levels centred on the corresponding band edges. In this picture, the charge carrier transport is then described as a transition of charge carriers from one energy level to another.

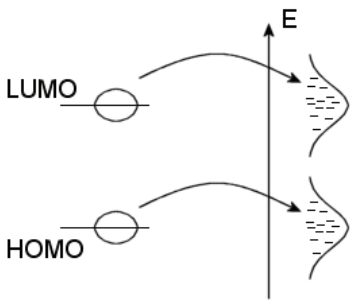

Figure 1.4:
Hopping transport of electric charges in an organic semiconductor.

This tunnelling process can be expressed by the rate W_{ij} for a transition from site j to site i. The probability depends of course on the spatial distance r_{ij} of the two sites and on the energetic difference ε_i-ε_j. If the energetic difference is positive, i.e. energy is required to conduct a hop, the probability is given by a Boltzmann factor, else it is given by the tunnelling probability. The energy is provided by phonons (thermally activated hopping), hence the name phonon-assisted tunnelling. This process was originally proposed by Conwell [99] and Mott [100]. The transition rates were calculate by Miller and Abrahams [101]:

$$W_{ij} = \nu_0 \cdot e^{-2\cdot\Gamma\cdot r_{ij}} \cdot \begin{cases} e^{-\frac{\varepsilon_i-\varepsilon_j}{k_B\cdot T}} & \varepsilon_i > \varepsilon_j \\ 1 & else \end{cases} \tag{1.2}$$

with the phonon frequency ν_0 at which the hopping takes place and the inverse localisation length Γ. Mott remarked, that in the case of huge energy differences of adjacent sites, the hops does not necessarily occur between two direct neighbours, leading to a variable range hopping (VRH) [8, 20, 22, 81, 102]. Bässler proposed, that the distribution of hopping sites has a Gaußian shape (see figure 1.4) [103]. In the Gaußian disorder model (GDM), Bässler [103] derived an expression for the temperature- and field-dependent

mobility:

$$\mu(E,T) = \mu_\infty \cdot \exp\left[-\left(\frac{2\cdot\sigma}{3\cdot k_B \cdot T} \right)^2 + c\left(\left(\frac{\sigma}{k_B \cdot T} \right)^2 - \Xi \right) \cdot \sqrt{E} \right] \tag{1.3}$$

$$\Xi = \begin{cases} \Sigma^2 & for \quad \Sigma \geq 1.5 \\ 2.5 & \Sigma < 1.5 \end{cases}$$

with the zero-field mobility in the infinite temperature limit μ_∞, the width σ of the density of states (DOS), a constant c, which depends on the site spacing and the degree of positional disorder Σ. Equation, (1.3) is in particular useful for high electric fields ranging from 100MV/m to 300MV/m. For lower electric fields the correlated disorder model (CDM) was proposed [104]. The model takes the local ordering due to charge-dipole interactions into account:

$$\mu(E,T) = \mu_\infty \cdot \exp\left[-\left(\frac{3\cdot\sigma}{5\cdot k_B \cdot T} \right)^2 + 0.78 \cdot \left(\left(\frac{\sigma}{k_B \cdot T} \right)^{\frac{3}{2}} - 2 \right) \cdot \sqrt{\frac{q\cdot a\cdot E}{\sigma}} \right] \tag{1.4}$$

with the elementary charge q and the average spacing between sites a.

Blom and Vissenberg showed, that the empiric equation of Gill describes systems well, with a series of ordered high-mobility regions, which are connected by one-dimensional conduction pathways with low mobility [43]. This model takes into account the fact that the local mobility can vary over orders of magnitude. The tunnelling rate $W_{n+1,n}$ from site n to site n+1 employed by Blom and Vissenberg was of the Glauber form [105]:

$$W_{n+1,n} = \nu \cdot \left(1 + e^{\frac{\varepsilon_{n+1} - \varepsilon_n - q\cdot E\cdot a}{k_B \cdot T}} \right)^{-1} \tag{1.5}$$

with the hopping rate v and the average distance a. Assuming an uncorrelated Gaußian disorder of the site energies with width σ the following equation is derived:

$$\mu(E,T) = \frac{\nu \cdot \frac{a}{E}}{1 + 2 \cdot e^{\left(\frac{\sigma}{k_B \cdot T}\right)^2} \cdot \left(e^{\frac{q \cdot E \cdot a}{k_B \cdot T}} - 1\right)^{-1}} \tag{1.6}$$

At low electric fields, the mobility is independent from the field, for higher fields it increases exponentially and finally at very high fields, the drift velocity saturates and the mobility decreases reciprocally with E.

All models described above have in common that for a fixed temperature, e.g. room temperature, the mobility value shows a characteristic exponential field dependence. The expression used in this work to describe the field-dependent mobility summarises this in the following reduced formula (compare with Poole-Frenkel method [106-108]):

$$\mu(E) = \mu_0 \cdot e^{\sqrt{\frac{E}{E_0}}} \tag{1.7}$$

with a characteristic field E_0 describing the field activation and a zero-field mobility μ_0. Note that μ_0 is now a temperature-dependent quantity. As shown in [109] this simplified model agrees well with experimental results.

2. Field-Effect Transistor Characterisation

In this chapter, a short introduction of the working principle of field-effect transistors is given. The two most important parameters of a transistor are the charge carrier mobility and the on-off ratio. However, this chapter focuses on the determination of the mobility, since the on-off ratio is mainly interesting for operating transistors in electronic circuits, which are not the objective of this work. Different theoretical models and approaches to extract the charge carrier mobility are presented. Finally, the results are discussed along with some mentionable effects.

2.1. Theoretical Introduction

Historically the working principle of a field-effect transistor (FET) is known since 1926, when J. E. Lilienfeld filed the first patent[4]. Notably at that time there was no known material system with the necessary properties to manufacture an actually working device. It took as long as the 1960s before the first FETs were produced based on a silicon/silicon oxide interface. For an overview of organic FETs see [11-13, 22]

A FET is a structure where a conducting channel between two electrodes (source and drain) is controlled by an electric field applied between source and gate. One of the most common realisations of a FET is the so-called metal-oxide-semiconductor FET (MOSFET). However, the transistors addressed in this work are realised as thin film transistors (TFT). A TFT unlike a MOSFET has no p-n junction, hence there is no depletion region. Consequently, the threshold voltage V_T of an ideal device is zero [87]. A real device though exhibits a non-zero threshold voltage mainly caused by the existence of traps, surface states and the fact that the metallic source and drain contacts usually do not form Ohmic contacts [83]. The transistors prepared for this work consist of a highly doped silicon wafer (gate), separated from the source and drain contacts by an insulating oxide (SiO_2). The channel between source and drain consists of a p-type semiconducting material. Figure

[4] The original US patent 1,745,175 was filed on October 8th 1926.

2.1 shows a schematic drawing of such a structure.

The transistors were operated in enhancement-mode, i.e. with negative voltage applied between gate and source to accumulate holes in the channel near to the interface with the insulator. Applying a small source-drain voltage V_{SD} (linear regime) a current flows between the two contacts and the channel behaves like a resistor. By varying the gate voltage V_G, more or less charge carriers are accumulated, changing the resistance of the channel. The structure can thus be looked at as a voltage-controlled resistor. If the source-drain voltage is increased, more and more charge carriers are drawn off by the drain, eventually starting to deplete the channel. This point is known as pinch-off [20] and the resistance of the channel is increasing rapidly. Consequently, the current saturates at a constant level and does not change anymore with increasing source-drain voltage (saturation regime). Both regimes are highlighted in the I-V-characteristics of figure 2.2.

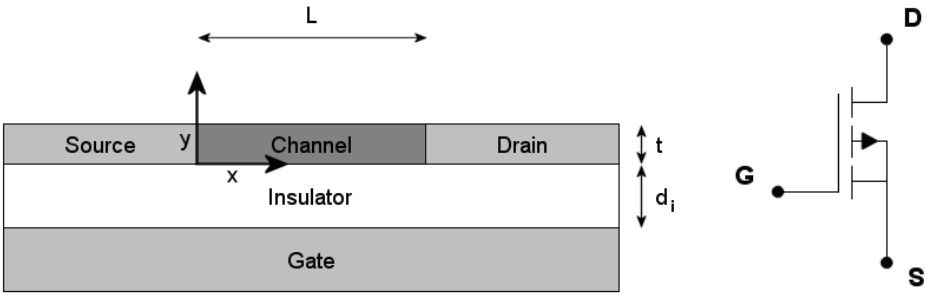

Figure 2.1:
Schematics of a field-effect transistor (left hand side) and electronic symbol of a TFT (right hand side) in enhancement-mode with source (S), drain (D) and gate contact (G). The light grey areas indicate the three contacts, while the dark grey area refers to the polymer filling in the channel.

For an ideal transistor the source-drain current vanishes for $|V_G| < |V_T|$. If the gate voltage is increased beyond the threshold voltage, a conducting channel

is formed and the source-drain current I_{SD} can be expressed as [11-13, 18, 75, 90, 110, 111]:

$$I_{SD} = \frac{W}{L} \cdot c_i \cdot \mu \cdot \left[\left(V_G - V_T \right) \cdot V_{SD} + \frac{1}{2} \cdot V_{SD}^2 \right] \tag{2.1}$$

with channel width W, channel length L, capacitance per area of the oxide c_i and mobility μ. Note, that despite of the commonly used name linear regime, a quadratic term appears in equation (2.1). It is therefore better to use the name triode regime, when referring to this equation. For further explanation and a simplified derivation of the equation, see appendix 10.2.1.

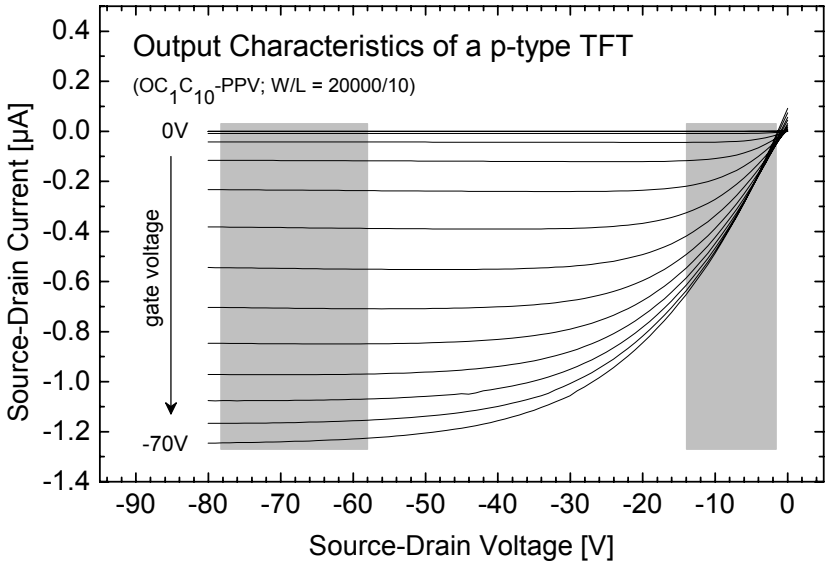

Figure 2.2:
Output characteristics of a p-type TFT in enhancement-mode. The gate voltage was swept in 5V steps. The highlighted areas mark the linear regime (right hand side) and the saturation regime (left hand side).

If the source-drain voltage becomes larger than $|V_G-V_T|$ the channel starts to deplete and the I-V characteristics transits into the saturation regime [8, 11, 12, 19, 21, 75, 85, 111, 112]:

$$I_{SD} = \frac{1}{2} \cdot \frac{W}{L} \cdot c_i \cdot \mu \cdot \left(V_G - V_T\right)^2 \tag{2.2}$$

This equation is based on a qualitative consideration as shown in appendix 10.2.2. Although equation (2.1) and (2.2) were developed for inorganic semiconductors, they describe reasonably the I-V characteristics of organic transistors.

As conducted in the following sections, both equations can be used to extract the FET-mobility of the polymer under investigation.

2.2. Experimental Details

The FET-substrates were purchased from Philips Research. They consisted of an n-type silicon wafer, highly doped with arsenic, to yield a resistivity of (0.001-0.005)Ω·cm. On top of the wafer, an oxide was thermally grown with a thickness of 204nm (as specified by the manufacturer). Using a relative permittivity of 3.9 [113] for the oxide, the capacitance of the oxide per area equates to 16.93nF/cm^2. The actual channel structures were evaporated on the oxide and consisted of a 10nm titanium layer for better adhesion and a 100nm gold layer. On a single chip of size 25mm × 25mm, various geometries were defined. However for the measurements only channels with constant width (W = 20000µm) and a length ranging from 1.5µm to 40µm were used. In figure 2.3 one channel is depicted. In order to contact the gate electrode (silicon wafer) later on, the oxide was removed at two opposite corners of the chip. Source, drain and gate were then contacted with the needles of a micromanipulator.

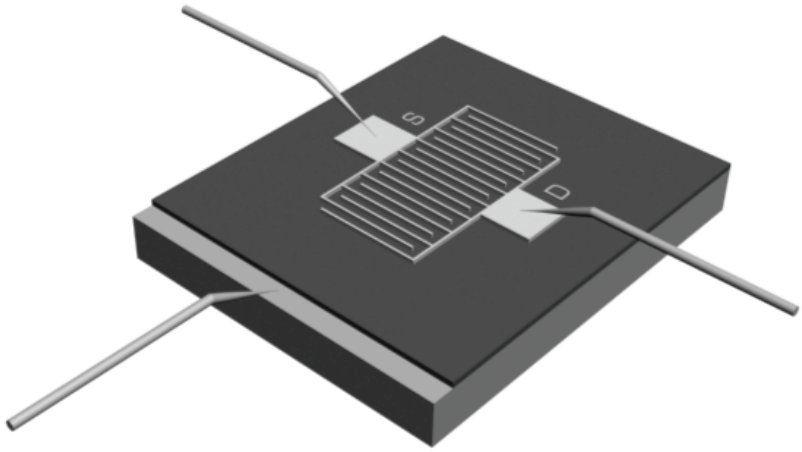

Figure 2.3:
Layout of an organic TFT as used in this work. Source (S), drain (D) and gate electrode were contacted by needles. Note that the drawing is not true to scale.

Before spin coating the polymer film, the substrates were thoroughly cleaned. First, the chips were cleaned with a 1:20 soap solution (Buehler Ultramet 2 Sonic Cleaning Solution). Then they were sonicated for 20 minutes in the same soap solution. After rinsing the samples with deionised water to remove soap residues, they were sonicated for 10 minutes in acetone. The cleaning process was completed by placing the samples for another 10 minutes in boiling isopropanol and blowing them dry afterwards.

Since the chips were protected by a monolayer of hexamethyl-disilazane (HMDS), an additional UV/ozone treatment was required. The samples were placed under a UV lamp for 15 minutes and afterwards transferred directly into the glove box.

The polymer layer was applied by spin coating a thin film from solution. The specific conditions for preparation of the solutions and spin coating are listed in the appendix 10.1.1. The spin coating conditions were usually chosen to yield thin films with a thickness ranging from roughly 30nm to 65nm. After spin coating, the samples were stored in vacuum for several hours to ensure complete evaporation of the solvent.

Prior to the actual measurement the corners of the chip where the oxide was previously removed, were contacted with the needles of a micromanipulator. The needles were connected to a Keithley 2400 in order to measure the resistance and to ensure that the gate was well-connected (constant low resistance). After this pre-test, the source and drain electrodes of a channel were also contacted and an opaque cover was placed on the chip to protect it from ambient light. Shielded cables were used to connect the needles to two Keithley 2400 source meters. The source was connected to the ground (low input) of the two source meters, while drain and gate were connected to the corresponding high inputs. Specific details about sweeping the source-drain voltage and the gate voltage can be found in the corresponding sections below.

2.3. Mobility Extraction from Standard Model

There are several different possibilities to extract the mobility from the linear regime (equation (2.1)) or from the saturation regime (equation (2.2)). In both cases, different assumptions can be made concerning the series resistance [7, 17-19, 86, 114], the field dependence of the mobility (see section 1.4), the gate-voltage dependence [22, 81-83, 107, 110, 111], etc. Depending on the exact assumptions and procedure to extract the mobility, different values can be obtained, thus requiring careful interpretation of the results. For all experiments discussed in this section, the source-drain voltage was swept from 0V to -80V in 1V steps. The gate voltage was varied from 0V to -70V in 5V steps.

2.3.1. Transfer Characteristics of Linear Regime

As mentioned earlier in equation (2.1), the triode regime includes a quadratic term for the source-drain voltage. However, for very small source-drain voltages compared to the gate-voltage the quadratic term can be neglected, leading to the following expression [8, 17, 23, 28, 82, 85, 115]:

$$I_{SD} = \frac{W}{L} \cdot c_i \cdot \mu \cdot \left(V_G - V_T\right) \cdot V_{SD} \tag{2.3}$$

There are two unknown parameters in equation (2.3), the threshold voltage V_T and the mobility μ. In order to determine the mobility the derivative of the source-drain current with respect to the gate voltage is calculated [11, 12, 20, 21, 75, 81, 82, 90]:

$$g_m := \frac{\partial I_{SD}}{\partial V_G} = \frac{W}{L} \cdot c_i \cdot \mu \cdot V_{SD} \tag{2.4}$$

g_m is known as transconductance and depends linearly on the source-drain voltage. By plotting the source-drain current against the gate voltage (transfer characteristics) for a fixed source-drain voltage, the mobility can be determined from the slope of the curve. Note, that in this procedure it is implicitly assumed that the mobility is a constant and that the voltage applied between source and drain equals the voltage that drops across the actual channel.

Figure 2.4 depicts typical output characteristics of the four polymers studied. While the order of magnitude of the source-drain current is the same for OC_1C_{10}-PPV and PEO-PPV, the values for (PEO-OC_9)-PPV and diPEO-PPV are somewhat lower. Furthermore, (PEO-OC_9)-PPV exhibited a derivation from the ideal shape. At the transition from the linear to the saturation regime, an "overshoot" occurs (see figure 2.4). The only significant difference observed between (PEO-OC_9)-PPV and the other PPVs in consequent measurements, was a roughly 10 times higher series resistance than for the other PPVs. This

has to be kept in mind when comparing later the mobility values determined from linear and saturation regime. This series resistance will be discussed in more detail in the following sections.

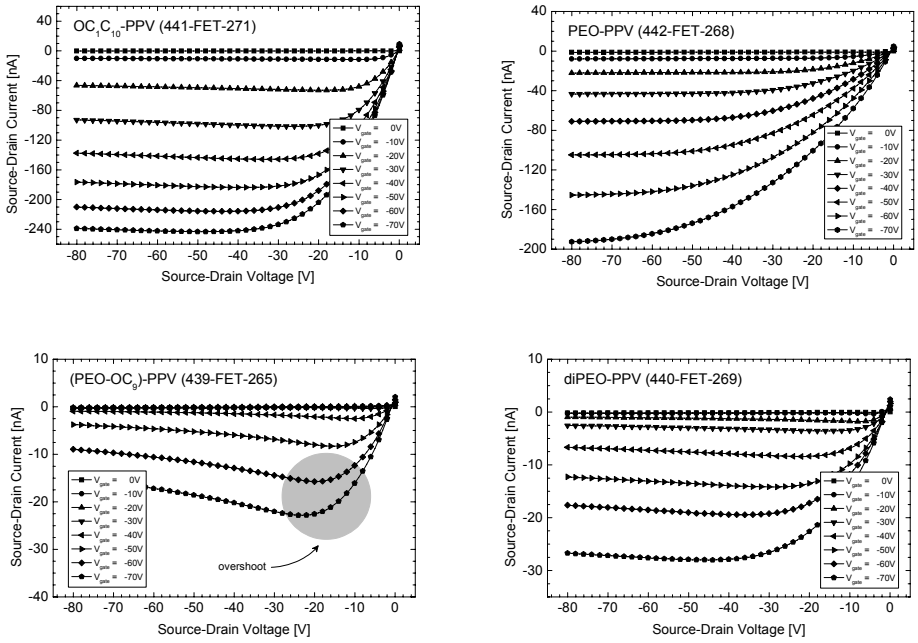

Figure 2.4:
Typical output characteristics for the four polymers studied. The geometry of the channels was identical for all measurements (W/L =20000/40). The samples were measured as-prepared without prior annealing. The code in brackets refers to the internal sample ID.

In order to determine g_m from equation (2.4) the source-drain current was plotted against the gate-voltage for a fixed source-drain voltage. For a given channel, the source-drain voltage was chosen to result in a field of 0.2MV/m. From the slope of the transfer characteristics g_m was obtained by performing a linear fit. Table 2.1 lists the results for the four PPVs. As mentioned earlier no corrections were performed to take series resistance, field dependence or other effects into account. The standard deviation was determined from the

error of the fit parameters.

Polymer	Mobility [10^{-6} cm^2/Vs]	Standard Deviation [10^{-6} cm^2/Vs]
OC_1C_{10}-PPV	*10.59*	*0.04*
PEO-PPV	*1.71*	*0.02*
(PEO-OC_9)-PPV	*4.84*	*0.01*
diPEO-PPV	*0.49*	*0.02*

Table 2.1:
The table lists the uncorrected mobility values as determined from the transconductance g_m. The standard deviation was determined from the error of the fit parameters.

The fits were in general rather accurate, resulting in a relative error between 0.2% and 1.2%. The only exception was diPEO-PPV, which was very difficult to analyse. Consequently, the relative error was as big as ~4%. Given the intricacy of the data extraction, the absolute value of the hole mobility $0.49 \cdot 10^{-6}$cm^2/Vs should be used carefully. The only purchased polymer studied OC_1C_{10}-PPV showed the highest mobility. This is attributed to a generally higher quality of a commercial material produced on large scale compared to an experimental material synthesised in a laboratory in low quantities.

2.3.2. Output Characteristics of Linear Regime

Starting from the same assumptions as in the previous section the mobility can also be determined from the output characteristics. This time the derivative of the source-drain current with respect to the source-drain voltage is calculated [19, 111]:

$$g_d := \frac{\partial I_{SD}}{\partial V_{SD}} = \frac{W}{L} \cdot c_i \cdot \mu \cdot \left(V_G - V_T\right) \tag{2.5}$$

g_d is the conductance of the output characteristic. The conductance depends linearly from the gate voltage. In order to extract the mobility, g_d has to be determined for different gate voltages by performing a linear fit for small source-drain voltages. Plotting these g_d values against the gate voltage enables to calculate the mobility from the slope of the linear curves. The resulting plots are depicted in figure 2.5 for different channel lengths. Over a large range of usually more than 20V, the dependence between conductance and gate voltage was shown to be linear.

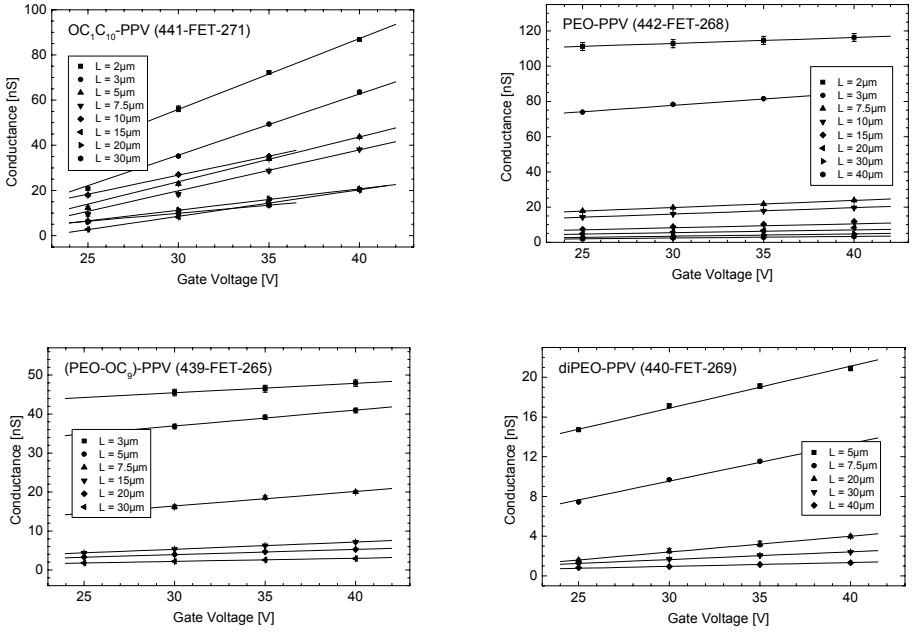

Figure 2.5:
Conductance g_d plotted against gate voltage V_G. In the considered range, g_d depends linearly from V_G. The conductance increases with decreasing channel length L.

In figure 2.6 the extracted mobility values for channels with different length are plotted against the channel length. The obvious dependence can be explained by a simple model, taking the series resistance and all other

contributions to the series resistance into account. Obviously, the relative influence of the series resistance diminishes with increasing channel length, i.e. increasing channel resistance. This has to be reflected by the model.

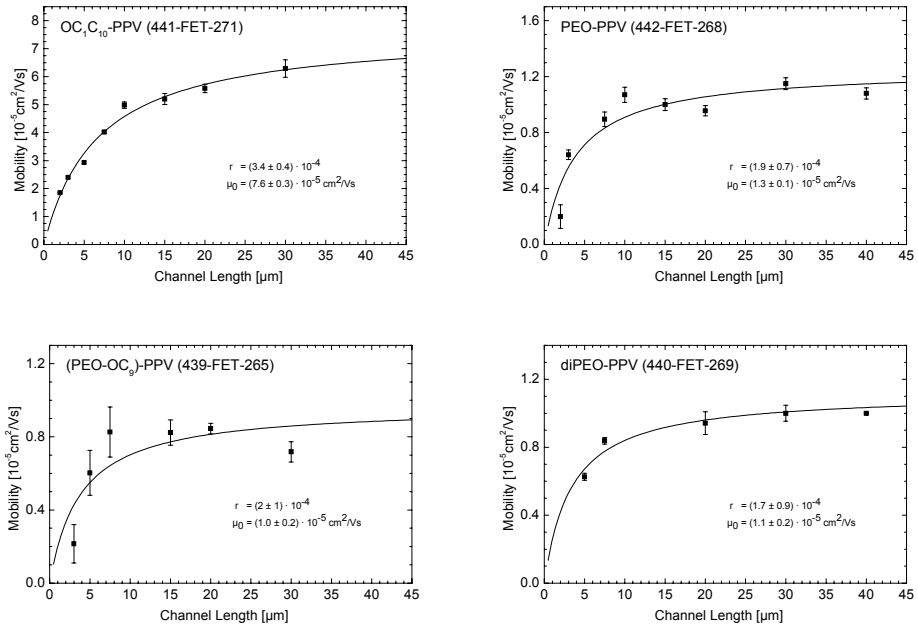

Figure 2.6:
Length-dependent mobility of the four PPVs studied. The measurement data was fitted with the model described below. The curves were calculated based on the displayed fit parameters μ_0 (corrected mobility) and r (ratio of series resistance and sheet resistance).

The total resistance R_{TOT} can be written as the sum of the series resistance R_S and the channel resistance R_{CH}:

$$R_{TOT} = R_S + R_{CH} \tag{2.6}$$

As shown in appendix 10.2.2 this model leads to a simple expression for the

channel length-dependent mobility μ(L):

$$\mu(L) = \mu_0 \cdot \frac{1}{1 + \frac{W}{L} \cdot r} \tag{2.7}$$

with the mobility μ_0 of the polymer film in the channel and ratio r between the series resistance and the sheet resistance. As mentioned above, μ(L) tends to μ_{CH} for increasing channel length, consistent with the observed saturation. In figure 2.6 the mobility is depicted for channels of different length. In the derivation of equation (2.7), it is assumed that the series resistance is the same for all channels. This is not necessarily true in the experiment. Nevertheless, from the fits in figure 2.6 it can be concluded, that the above model describes the measurement results correctly. By fitting equation (2.7) to the measurement data, a mobility value that is corrected for the series resistance can be extracted. Note, that the series resistance and the sheet resistance cannot be determined independently, but only there ratio r.

Polymer	**Mobility** **[10^{-5}cm^2/Vs]**	**r = R_S/R_{SHEET}** **[10^{-4}]**
OC_1C_{10}-PPV	*7.6 ± 0.3*	*3.4 ± 0.4*
PEO-PPV	*1.3 ± 0.1*	*1.9 ± 0.7*
(PEO-OC_9)-PPV	*1.0 ± 0.2*	*2 ± 1*
diPEO-PPV	*1.1 ± 0.2*	*1.7 ± 0.9*

Table 2.2:
The table lists the corrected mobility values for the four studied PPVs. For all polymers, the sheet resistance is roughly four orders of magnitude higher than the series resistance.

The fit results are listed in table 2.2. The corrected hole mobility values of the PEOs are all in the range of $1 \cdot 10^{-5}$cm^2/Vs. Again, the purchased material

OC_1C_{10}-PPV exhibited a significantly higher mobility of $7.6 \cdot 10^{-5} cm^2/Vs$ (compare with table 2.1). However, the ratio between the series resistance and the sheet resistance is more or less the same for all four polymers. The ratio is in the range of 10^{-4}, i.e. the sheet resistance of the channel is roughly four orders of magnitude higher than the series resistance.

Returning to the plots in figure 2.5, it is noted, that the offsets of the linear fits are a measure for the conductance of the channel at zero gate voltage. Hence, the reciprocal value is the total resistance R_{TOT} of the structure. Plotting R_{TOT} against the channel length and assuming again that the series resistance R_S of all channels is the same, the channel resistivity ρ and the series resistance can be extracted by a fit of the following equation:

$$\begin{aligned} R_{TOT} &= R_S + R_{CH} \\ &= R_S + \rho \cdot \frac{L}{W \cdot t} \end{aligned} \tag{2.8}$$

The film thickness t appearing in the equation can be determined by partly removing the film from the FET-chip and measuring the height difference with a surface profiler.

Figure 2.7 shows the total resistance depending on the channel length. From a least-square fit of equation (2.8) both the resistivity ρ and the series resistance R_S can be determined. The results are listed in table 2.3 along with the conductivity σ and the charge carrier concentration p. The charge carrier concentration was determined from the relation:

$$\sigma = q \cdot p \cdot \mu \tag{2.9}$$

with the elementary charge q. Since the conductivity and the mobility were determined under the same circumstances, i.e. identical applied voltages and are both corrected for R_S the determined value constitutes a reasonable quantity.

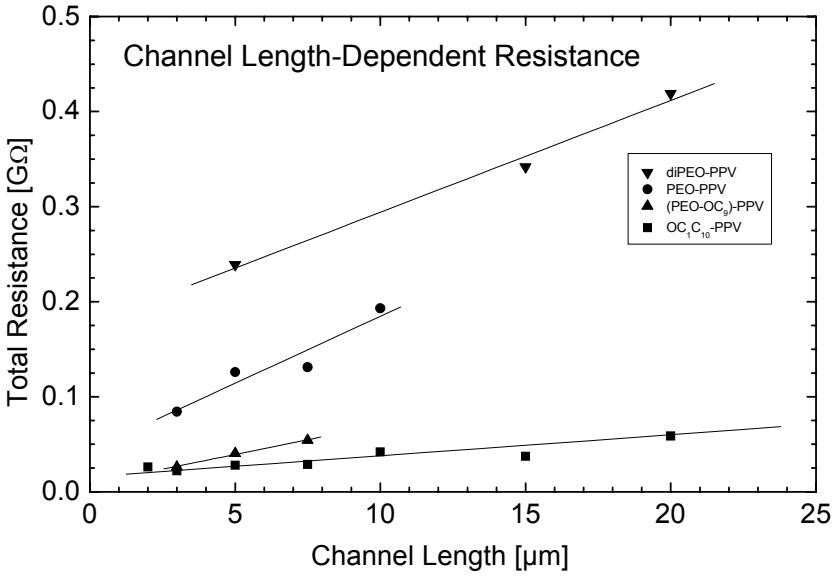

Figure 2.7:
Total resistance of a channel plotted against the channel length. The resistivity of the polymer can be extracted from the slope of the fitted curve, while the offset is a measure for the series resistance.

Again, the PEOs exhibited similar material parameters, while the purchased OC_1C_{10}-PPV was significantly more conductive. The charge carrier concentration of $\sim 10^{17} cm^{-3}$ for all polymers lies within the range, expected from a doped semiconductor. Notably the series resistance of PEO-PPV and diPEO-PPV are much larger then for the other two materials. In general it seems that the series resistance can vary over a large range, probably also for a single material. Consequently, the errors of the fitting parameters were quite large, since the applied model assumed implicitly a constant value for R_S. It is not entirely clear whether the absolute value of R_S is more material related or if it is a problem of preparation. However, diPEO-PPV samples have shown to be more problematic than the other PPVs, suggesting a material related origin of the large series resistance.

Polymer	ρ [kΩ·m]	σ [10^{-4} S/m]	p [10^{17} cm^{-3}]	R_S [MΩ]
OC_1C_{10}-PPV	*1.4 ± 0.2*	*6.8 ± 0.8*	*5.7 ± 0.7*	*16 ± 4*
PEO-PPV	*12.9 ± 3*	*0.8 ± 0.2*	*3.7 ± 0.9*	*44 ± 20*
(PEO-OC_9)-PPV	*8.3 ± 0.6*	*1.21 ± 0.09*	*8 ± 2*	*8 ± 3*
diPEO-PPV	*14 ± 6*	*0.7 ± 0.3*	*4 ± 2*	*120 ± 90*

Table 2.3:
Resistivity ρ, conductivity σ, charge carrier density p and series resistance R_S.

2.3.3. Transfer Characteristics of Saturation Regime

Finally, the mobility can also be extracted from the saturation regime. For a fixed source-drain voltage, the mobility and threshold voltage can be determined directly from a parabolic fit of the transfer characteristics according to equation (2.2). In appendix 10.2.2 it was pointed out that the gradual channel approximation does not hold true anymore in the saturation regime. Consequently, the electric field is varying along the channel, i.e. mobility values extracted from the saturation regime generally have to be interpreted as a mean mobility, averaged over different fields [81, 83].

In figure 2.8 the transfer characteristics of two typical samples is depicted. The curve on the left hand side exhibits an almost perfect parabolic behaviour over the entire measurement range. The plot on the right hand side however deviates from the ideal shape for larger $|V_G|$. As will be discussed in section 2.4 the deviation origins from the gate voltage dependence of the mobility. In order to apply equation (2.2) the fitting range thus has to be restrict to the regime where the parabolic approximation holds true. Further, measurement points below the threshold voltage were excluded too.

The transfer characteristics displayed in figure 2.8 were obtained by transposing the data of the previous section (see figure 2.1) for a specific source-drain voltage in the saturation regime. For the 40µm channel the last data point at V_{SD} = -80V was taken, leading to an arbitrary chosen electric field of 2MV/m. Note, that this is ten times higher than the field at which the

mobility values of section 2.3.1 where determined. Since it is already well-known that the mobility varies exponentially with the electric field, the source-drain voltage at which the transfer characteristics were analysed was reduced for shorter channels to ensure a constant field. For the shortest characterised channel with a length of 1.5µm, this leads to a source-drain voltage of -3V. Such a small voltage usually lies not anymore in the saturation regime. Hence, these measurement points are excluded from the subsequent analysis.

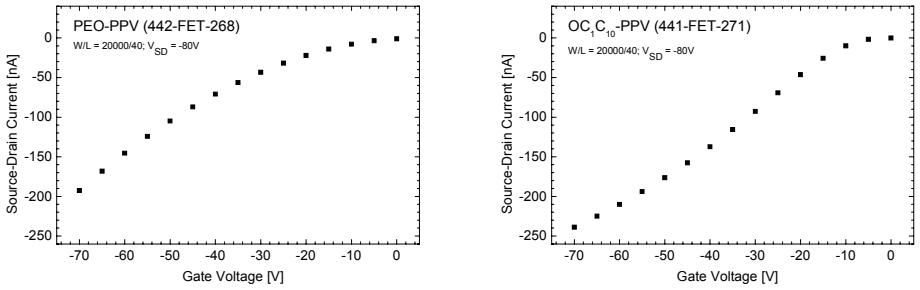

Figure 2.8:
Transfer characteristics of two different samples. The curve on the left hand side exhibits an almost ideal parabolic behaviour as expected from equation (2.2). The curve on the right hand side however shows a significant deviation for large $|V_G|$.

In figure 2.9 the extracted mobility values are plotted against the channel length. Applying the model of the previous section to correct for the series resistance leads to the channel mobility μ_0. Although the source-drain voltages of the shorter channels lie outside the saturation regime, they are in good agreement with the applied model.

Table 2.4 lists the model parameters as obtained from the fit in figure 2.9. Notably the mobility values are comparable with the values extracted in section 2.3.2 from the linear regime. For OC_1C_{10}-PPV the value is even smaller by a factor of ~2. This is surprising since it is usually considered that the lower charge carrier concentration in the linear regime leads to mobility values,

which are smaller by orders of magnitude [7, 19]. However, it has to be kept in mind that both extraction methods are based on different assumptions.

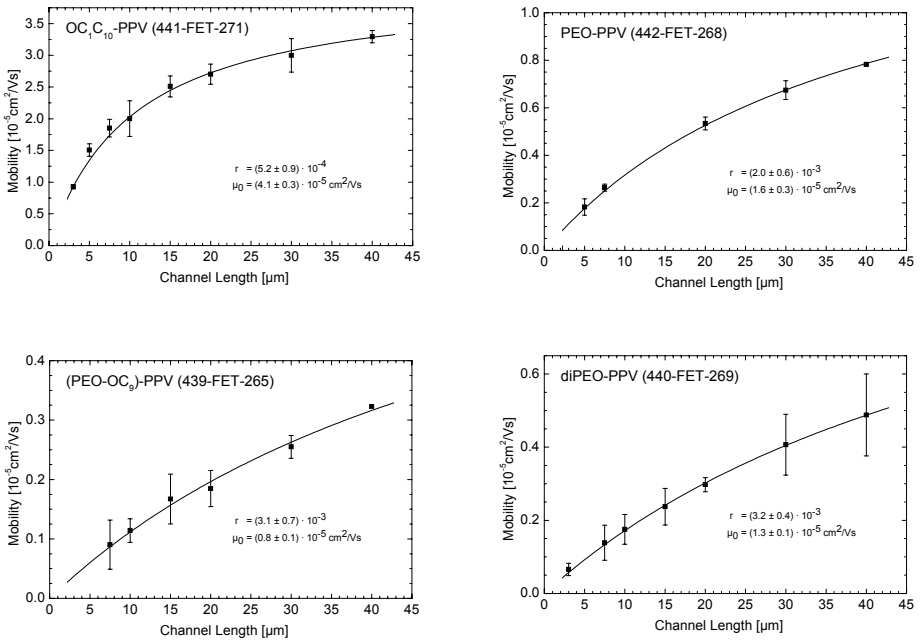

Figure 2.9:
Length-dependent mobility of the four PPVs studied. The measurement data was fitted with the model described in section 2.3.2. The curves were calculated based on the displayed fit parameters μ_0 (corrected mobility) and r (ratio of series resistance and sheet resistance).

Thus, the results are not directly comparable. For instance, the field dependence of the mobility was entirely neglected in section 2.3.1 while in this section it was ensured to keep the electric field constant. However, the chosen value of 2MV/m was completely arbitrary. Further, to mention it again, mobility values extracted from the saturation regime are averaged values, while in the linear regime the gradual channel approximation holds true.

Polymer	Mobility $[10^{-5}cm^2/Vs]$	$r = R_S/R_{SHEET}$ $[10^{-3}]$
OC_1C_{10}-PPV	*4.1 ± 0.3*	*0.52 ± 0.09*
PEO-PPV	*1.6 ± 0.3*	*2.0 ± 0.6*
(PEO-OC_9)-PPV	*0.8 ± 0.1*	*3.1 ± 0.7*
diPEO-PPV	*1.3 ± 0.1*	*3.2 ± 0.4*

Table 2.4:
The table lists the corrected mobility values for the four studied PPVs. The mobility of the purchased material OC_1C_{10}-PPV is higher than the mobility values of the PEOs. For all polymers, the sheet resistance is roughly three orders of magnitude higher than the series resistance.

The extracted ratio between series resistance and sheet resistance was in the range of 10^{-3}, i.e. the sheet resistance is 1000 times bigger than the series resistance. This is ten times less than in the linear regime. If the series resistance is mainly determined by the contact resistance, it should decrease for higher voltages [116]. However, at the same time the sheet resistance changes too, because in the saturation regime the channel is partly depleted. Thus, the sheet resistance is not the same as for the bare channel without a gate voltage. Therefore, it is difficult to predict how the ratio of series resistance and sheet resistance relates between linear and saturation regime.

2.4. Extraction of Electrical Properties from Transfer Characteristics

The previously described methods take neither the field dependence nor the gate-voltage dependence of the mobility into account. The consequences of this shortcoming are discussed later in chapter 6. Further, the series resistance is artificially introduced afterwards by virtue of equation (2.7). In this section, a more elaborate model is introduced to address both the series resistance and the gate voltage-dependent mobility from the very beginning.

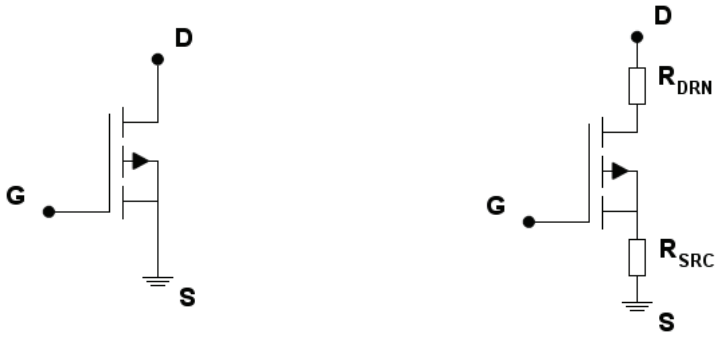

Figure 2.10:
The schematics show the equivalent circuits for an ideal TFT (left hand side) and a channel with contacts on the source side R_{SRC} and the drain side R_{DRN} (right hand side) in series.

This extended model is based on the transfer characteristics. Starting from the simplified equation (2.3) for the linear regime, a gate-voltage-dependent mobility $\mu(V_G)$ is introduced and the voltage drop at the series resistance discussed earlier is included. Figure 2.10 shows the equivalent circuit used so far (left hand side) and the equivalent circuit of the extended model (right hand side). All contributions to the series resistance of the source side R_{SRC} and the drain side R_{DRN} are combined in the parameter R_S. If the gate voltage is much larger than the source-drain voltage, the drop of the gate voltage across R_{SRC} can be neglected. Equation (2.3) leads then to the following expression:

$$I_{SD} = \frac{W}{L} \cdot c_i \cdot \mu(V_G) \cdot (V_G - V_T) \cdot (V - I_{SD} \cdot R_S) \qquad (2.10)$$

with the applied voltage V and the voltage drop $I_{SD} \cdot R_S$ across all series resistances combined. This equation can be solved for the source-drain current I_{SD}:

$$I_{SD} = \frac{\frac{W}{L} \cdot c_i \cdot \mu\left(V_G\right) \cdot \left(V_G - V_T\right) \cdot V}{1 + \frac{W}{L} \cdot c_i \cdot \mu\left(V_G\right) \cdot \left(V_G - V_T\right) \cdot R_S} \tag{2.11}$$

In order to fit this equation to the measurement data an expression for $\mu(V_G)$ is needed. A semi-empirical dependence of the mobility from the gate voltage is given by [83]:

$$\mu\left(V_G\right) = \alpha \cdot \left(V_G - V_T\right)^{\beta} \tag{2.12}$$

Note, that this equation is only true mathematically, since β is usual a fraction. Furthermore, this means it is only applicable for gate voltages greater than the threshold voltage.

A non-empirical approach is the following equation, which links the gate voltage dependence for a given temperature T to the trap concentration [83]:

$$\mu\left(V_G\right) = \mu_{00} \cdot \frac{N_C}{N_T} \cdot \left(\frac{V_G - V_T}{V_0} \right)^{\frac{T_C}{T} - 1} \tag{2.13}$$

with the zero-field mobility μ_{00} in the case of a trap-free material, the effective density of states N_C at the band edge and N_T, V_0 and T_C describing the distribution of traps [83]. The characteristic voltage V_0 is defined as:

$$V_0 = \frac{q \cdot N_T}{c_i} \tag{2.14}$$

A comparison of equation (2.12) with (2.13) shows that α is given by:

$$\alpha = \frac{\mu_0}{V_0^{\beta}} \tag{2.15}$$

Hence, in a fit it is impossible to separate the contribution of μ_0 and V_0 to α without further information (e.g. mobility at different temperatures). Equation (2.12) was therefore used for the fit. Note, that the unit of α depends on the value of β.

Combining equation (2.11) and (2.12) one finally obtains:

$$I_{SD} = \frac{\frac{W}{L} \cdot c_i \cdot \alpha \cdot \left(V_G - V_T\right)^{\beta+1} \cdot V}{1 + \frac{W}{L} \cdot c_i \cdot \alpha \cdot \left(V_G - V_T\right)^{\beta+1} \cdot R_S} \tag{2.16}$$

There are four unknown parameters in this equation. Reference [117] proposes a differential approach to extract these parameters one at a time. However, it appears that a direct fit of this non-linear equation yields stable and reliable results. Given the difficulties of determining the derivative numerically makes the direct fit even more appealing.

Initial measurements showed that the leakage current through the insulating layer can be quite significant (50% to 100%), especially for channels that are more conductive. Since this effect is not considered in equation (2.10), it is import to reduce this side effect. Therefore all measurements were performed at rather short channels, hence the surface L·W of the channel contributed less to the leakage current. In contrast to the preceding sections, the source-drain voltage was not swept this time. Instead, it was kept at a fixed value, usually -0.5V. A channel length of either 1.5µm ((PEO-OC_9)-PPV and diPEO-PPV) or 2µm (OC_1C_{10}-PPV and PEO-PPV) yields an electric field comparable to the 0.2MV/m of section 2.3.1. Further, the small electric fields ensure that the obtained mobility values represent the field-independent part of µ(E). The gate voltage was swept from 0V to -70V in 1V steps.

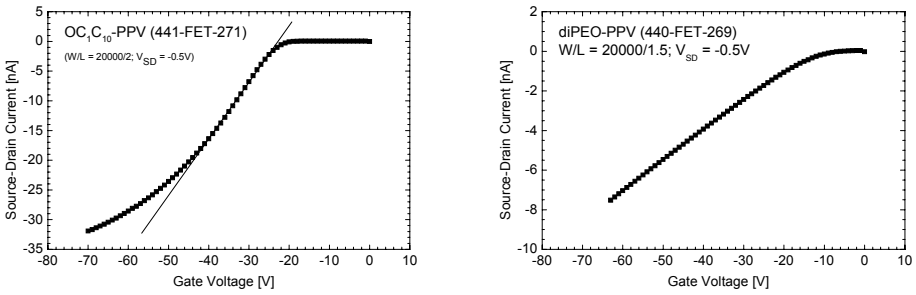

Figure 2.11:
Typical transfer characteristics of the linear regime for a sample with rather large threshold voltage (left hand side) and for a sample with negligible threshold voltage (right hand side). For the OC_1C_{10}-PPV sample, the gate voltage dependence of the mobility becomes noticeable for larger $|V_G|$ (deviation from the linear curve).

Figure 2.11 shows two transfer characteristics of the linear regime. The plot on the left hand side exhibits a rather large absolute value of the threshold voltage of around -20V. The plot on the right hand side shows a sample with an almost negligible threshold voltage. In order to fit equation (2.16) all points below the threshold voltage are excluded, since the model assumes that there is no conducting channel present for smaller gate voltages, hence no current flow. Further SI units are used without prefixes. This is important in order to apply the semi-empirical model of equation (2.12) for the gate voltage dependence of the mobility.

Table 2.5 lists the results of the least-square fits of equation (2.16). The prefactor α is a measure for the mobility. However, the unit depends on the exact value of the exponent β. At a gate voltage of $|V_G-V_T| = 1V$ it equals the mobility at that voltage. The exponent β, which is related to the trap concentration, is usually smaller than one. The quasi-linear dependence of the gate voltage behaviour mentioned in reference [81, 85, 111, 118] was not confirmed. Therefore, it is concluded that the exact gate voltage dependence is characteristic for the investigated polymer. Comparing the values with the results of the previous sections shows that taking the gate voltage into account, the mobility values are significantly lower.

Polymer	α [10^{-7} $cm^2/Vs/V^{\beta}$]	β	V_T [V]	R_S [MΩ]
OC_1C_{10}-PPV	*11.8 ± 0.6*	*0.85 ± 0.02*	*-33.69 ± 0.09*	*12.80 ± 0.08*
PEO-PPV	*0.41 ± 0.01*	*0.730 ± 0.002*	*20.79 ± 0.07*	*70.311 ± 0.002*
(PEO-OC_9)-PPV	*0.100 ± 0.003*	*0.570 ± 0.009*	*-1.31 ± 0.10*	*7.22 ± 0.05*
diPEO-PPV	*2.5 ± 0.2*	*0.46 ± 0.03*	*-7.4 ± 0.2*	*15 ± 1*

Table 2.5:
The fitting parameters of equation (2.16) are listed for the four PPVs under investigation. The prefactor α is a measure for the mobility, while β is linked to the trap concentration. Note, that the threshold voltage V_T can be either positive or negative. The series resistance R_S is usually quite high in the range of several MΩ.

As mentioned above the gate voltage dependence is caused by the rather high trap concentration. When the gate voltage is increased, more charges are accumulated in the channel, gradually occupying the traps. As a result, charge carriers drifting from source to drain are less likely to be trapped, hence the mobility increases [22, 81-83, 107, 110].

Further table 2.5 lists the threshold voltage. As mentioned in the introduction 2.1 and in the appendix 10.2.1 the threshold voltage can be either positive or negative and is not directly linked to a physical quantity. The series resistance R_S is usually quite large in the range of several MΩ.

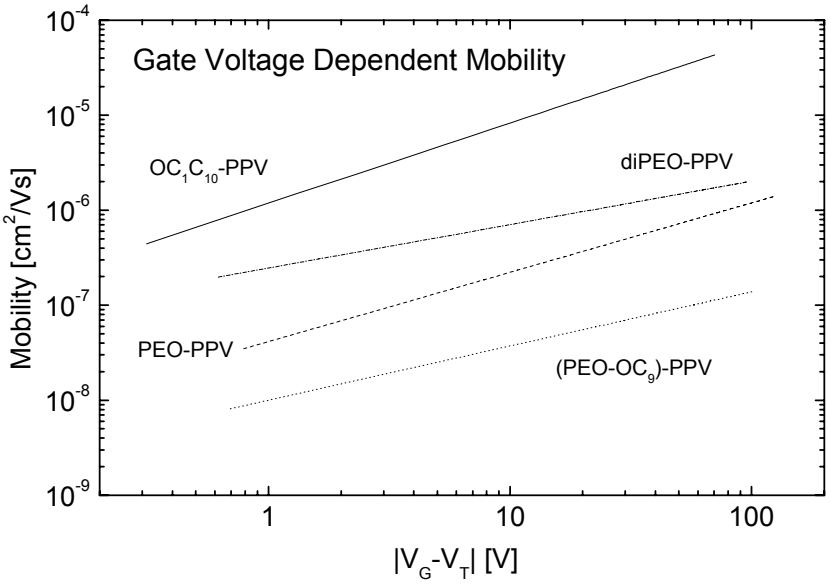

Figure 2.12:
Gate voltage-dependent mobility of the four PPVs studied, as calculated from the parameters of table 2.5 and equation (2.12).

Figure 2.12 depicts the gate voltage-dependent mobility as calculated from the parameters of table 2.5 and equation (2.12). When characterising FETs, typically gate voltages from 0V to -70V are applied. The plot shows that in this range the mobility can vary by one or even two orders of magnitude. This is one reason why different mobility values for the same polymer are reported in literature.

So far, it was assumed that the mobility values determined for a source-drain voltage of -0.5V is the field-independent part of the mobility. In order to confirm this, the same measurements as above were performed again for different source-drain voltages ranging from -0.1V to -1V. While for OC_1C_{10}-PPV and diPEO-PPV indeed no field dependence was observed, PEO-PPV and (PEO-OC_9)-PPV exhibited an exponential dependence on the applied field E. Since the mobility is mainly given by the prefactor α, the

following model was assumed (compare with equation (1.7)):

$$\alpha\left(E\right) = \alpha_0 \cdot e^{\sqrt{E/E_0}} \tag{2.17}$$

with the characteristic field E_0 which describes the degree of field dependence and the zero-field value α_0 (field-independent part). This simplified model holds true only for a certain range. For higher fields the mobility reaches a maximum and decreases again (see equation (1.6)).

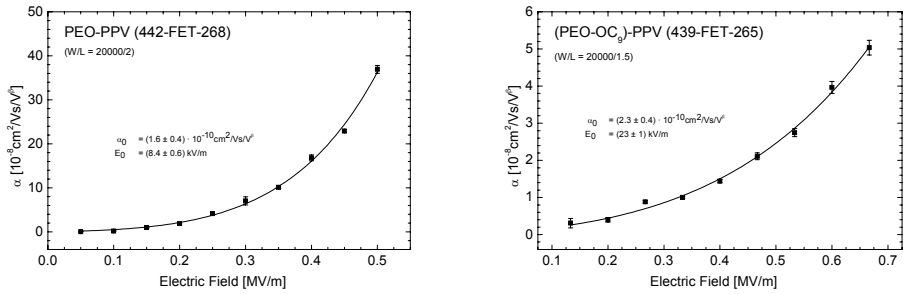

Figure 2.13:
Field dependence of mobility as observed for PEO-PPV and (PEO-OC_9)-PPV. The curves represent a least-square fit of equation (2.17).

Table 2.6 lists the results of a least-square fit of equation (2.17). The prefactor α_0 is in the range of 10^{-10}cm^2/Vs/V$^\beta$. Hence, the zero-field mobility is even smaller than the values of table 2.5. The characteristic electric field E_0 lies in the range of tens of kV/m.

Polymer	**α_0 [10^{-10} cm^2/Vs/V$^\beta$]**	**E_0 [kV/m]**
PEO-PPV	*1.6 ± 0.4*	*8.4 ± 0.6*
(PEO-OC_9)-PPV	*0.8 ± 0.1*	*23 ± 1*

Table 2.6:
Zero-field "mobility" α_0 and characteristics electric field E_0.

2.5. Additional Effects

2.5.1. Bias Stress

So far, it was always assumed that the polymer under investigation is not changing during the measurement. However, it was observed that the transfer characteristics can significantly shift upon continuous stressing of the polymer by applying a voltage. It is believed that this is due to the removal of mobile charges from the channel by trapping [27, 119]. Figure 2.14 shows the transfer characteristics for two different PPVs on successive measurements. In both cases the sample was measured every ~260s. Between the first and the last measurement 45min had passed. The plot on the left hand side shows a polymer with a rather small bias-stress effect, while the plot on the right hand side shows OC_1C_{10}-PPV, which exhibited a strong bias-stress effect. The behaviour of (PEO-OC_9)-PPV was shared by the other two PEOs. Therefore, the following analysis applies to OC_1C_{10}-PPV only.

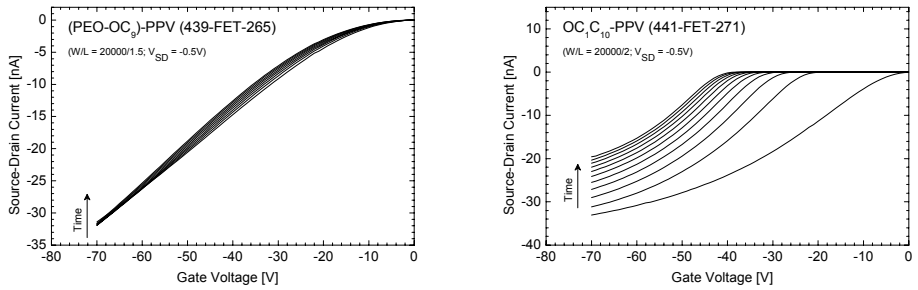

Figure 2.14:
Typical transfer characteristics of two PPVs. The plot on the left hand side shows only a small bias-stress effect upon repeated measurements. However, the plot on the right hand side shows a very strong effect when biasing the sample, most obviously pronounced by a shift of the threshold voltage.

If the bias-stress was caused by a trapping of charges, the process should be completely reversible. As described in reference [27] depending on the material, i.e. the energetic level of the traps, it can take even several days in

darkness to reverse the bias-stress. The left hand side of figure 2.15 compares the transfer characteristics obtained by successively measuring the sample with a curve that was acquired 4.5h after the last measurement. It clearly shows that the process is slowly reversed. The right hand side of figure 2.15 shows the mobility parameter α as extracted from the measurement curves by applying the model described by equation (2.16). In the considered range, the mobility parameter decreases linearly with continuing bias-stress. However, from the I-V curves (left hand side of figure 2.15) it is expected that the mobility stabilises after a while. The grey circle denotes the mobility determined from the measurement 4.5h after the initial stressing. Since applying both gate voltages and source-drain voltages is part of the measurement process, the samples are continuously stressed during characterisation. Hence, the determined mobility value can vary. However, even for OC_1C_{10}-PPV which was most sensitive to bias-stress, the mobility parameter α changed only by a factor of two. Nevertheless, in order to avoid bias-stress effects, it is proposed to use pulsed measurements, which reduce the time a voltage is applied [27].

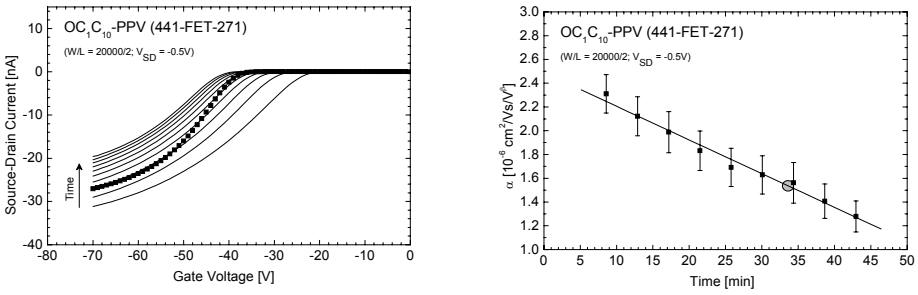

Figure 2.15:
The left hand side compares the transfer characteristics measured successively (solid lines) and 4.5h after the last measurement (squares). The right hand side shows the effect of bias-stress on the mobility parameter α. The circle denotes the mobility after partial recovery from the bias-stress (4.5h later).

2.5.2. Light Dependence

In the previous section it has been shown, that biasing a transistor can lead to a shift of the transfer characteristic. Consequently, the mobility dropped linearly in the considered range. It was furthermore pointed out that the recovery process is very slow in darkness. This process can be dramatically accelerated upon illumination. Instead of hours or days, the recovery occurs in seconds or minutes [27, 85, 119]. The following measurements were performed on samples that were already electrically characterised prior to the measurements. Thus at the beginning of the experiment they already had been excessively stressed. The channel was continuously illuminated with white light during the measurement. The light is expected to assist the release of trapped charge carriers [27, 85], thus influencing the mobility. Upon illumination, the absorbed light generates electron-hole pairs (excitons). Unlike in blended films of donor and acceptor materials, the only way for these excitons to dissociate is to recombine with trapped charges, leaving a free mobile charge behind. Since the film thicknesses lie in the range of 30nm to 60nm, the excitons are generated throughout the entire layer. The rather high diffusion coefficient [27] ensures that the excitons are distributed evenly in the entire film, thus also in the vicinity of the insulating layer, where the charge transport takes place. In the previous measurements, which were all performed in darkness, a static situation was present. Once a gate voltage was applied, a given number of charge carriers were accumulated in the channel and partially occupied the traps. Hence, the mobility increased with increasing gate voltage. Under illumination, however the process is dynamical. Trapped charges are continuously released, enabling the traps to capture new charges, hence hindering their transport and therefore reducing the mobility.

Figure 2.16 depicts the effect of the process described above. The illumination was increased from 0% to 100% (~7129lx, measured with a photodiode Siemens BPW21). The mobility decreases with increasing illumination. The curve progression was fitted with an empirical exponential model:

$$\alpha(I) = \alpha_0 \cdot e^{-\frac{I}{I_0}} \tag{2.18}$$

with the mobility parameter α_0 in darkness and characteristic illuminance I_0. Note, that the bias-stress discussed in the previous section and the observed light dependence share the same origin, i.e. the high concentration of traps. However, the two effects can be clearly distinguished from each other since the first is linear in the considered regime and the latter is exponential. Furthermore, figure 2.6 indicates, that even a low intensity is sufficient to accelerate the release of trapped charges, leading to a recovery of the stressed material.

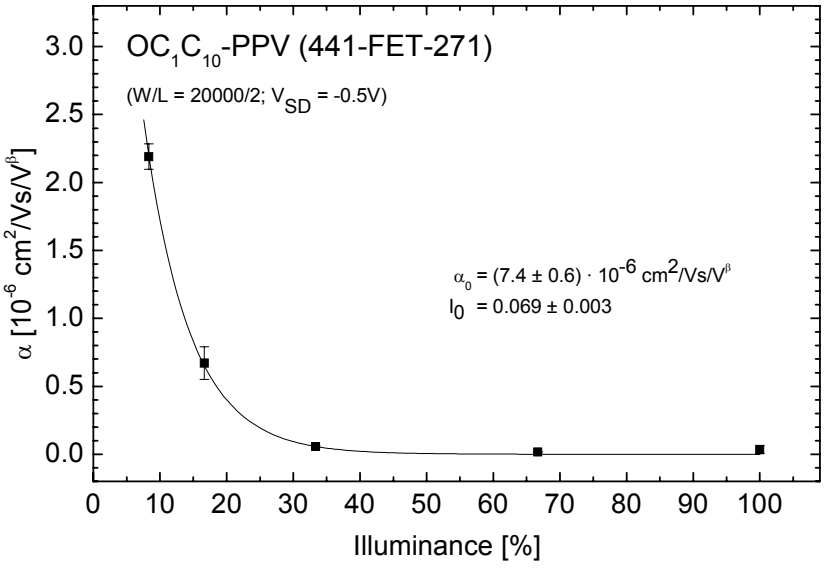

Figure 2.16:
Light dependence of the mobility parameter α as extracted from the transfer characteristics of the linear regime.

Consequently, it is expected that this effect will not be observed for polymers, which exhibited only a small bias stress effect as shown for the PEOs in the previous section. Accordingly there was no clear light dependence observed for the PEOs and the mobility remained almost constant (compare with reference [115]).

2.5.3. Annealing of Contacts

While measuring the samples it was observed that the series resistance can be very high for particular polymers. Further from I-V curves, it was noticed that the contacts were not symmetrical (see figure 2.17). In order to enhance the reproducibility and reduce the series resistance of the contacts, the polymer films were annealed on a hotplate

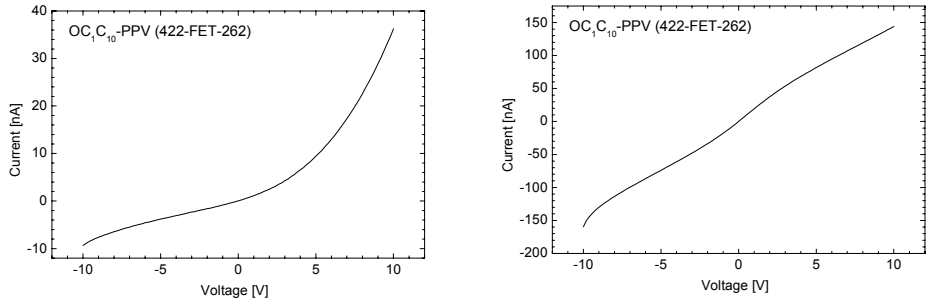

Figure 2.17:
I-V curves of an OC_1C_{10}-PPV sample before annealing (left hand side) and after annealing (right hand side). The as-prepared sample exhibits Schottky-like behaviour, while the annealed sample has a more Ohmic I-V curve.

The annealing temperature was chosen to be well above the glass transition temperature of the polymers. For these experiments, the samples were annealed at 150°C for 15 minutes. The mobility values of this section were determined from the transfer characteristics of the saturation regime (section 2.3.3). The source-drain voltage was again chosen to obtain a constant field of 2MV/m for the different channel lengths. The mobility values were corrected for the series resistance but not for the gate voltage dependence.

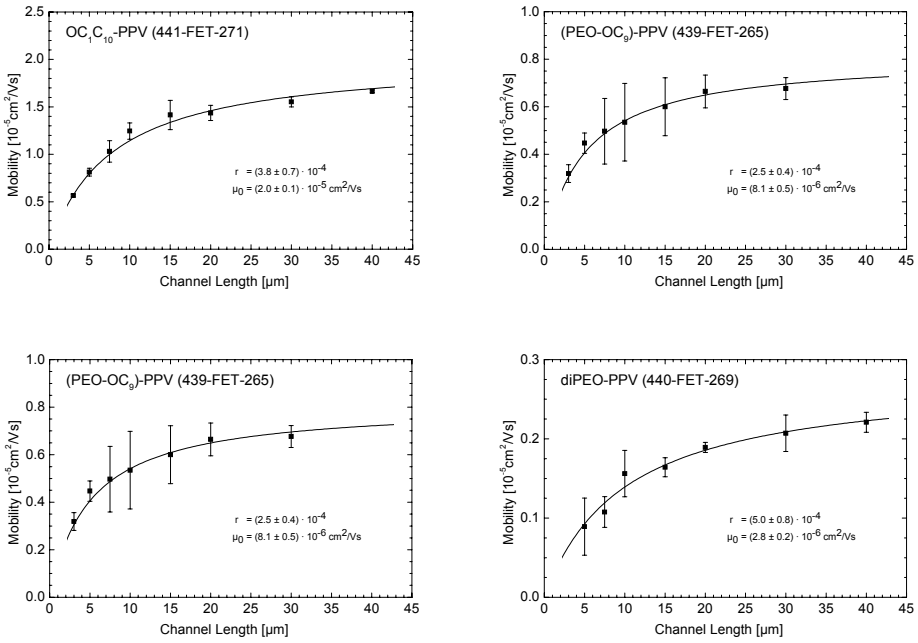

Figure 2.18:
Length-dependent mobility values of the four studied PPVs after annealing of the films at 150°C for 15 minutes. The mobility values were determined from the transfer characteristics in the saturation regime.

Figure 2.18 shows the length-dependent mobility values along with a fit of equation (2.7). The corrected mobility value μ_0 and the ratio r of series resistance and sheet resistance are listed in table 2.7 for both the annealed samples and the as-prepared samples.

The mobility values of the four PPVs decreased significantly. Except for (PEO-OC_9)-PPV, where the mobility remained the same within one standard deviation. This is rather surprising, considering that the polymer chains had the opportunity to align in the channel (for a more detailed discussion see section 5.2). The decrease of the mobility raises the question, whether the polymer structure remained intact at such an elevated temperature.

Polymers	annealed		as-prepared	
	Mobility [10^{-5} cm^2/Vs]	**r = R_S/R_{SHEET} [10^{-4}]**	**Mobility [10^{-5} cm^2/Vs]**	**r = R_S/R_{SHEET} [10^{-4}]**
OC_1C_{10}-PPV	*2.0 ± 0.1*	*3.8 ± 0.7*	*4.1 ± 0.3*	*5.2 ± 0.9*
PEO-PPV	*0.20 ± 0.06*	*5.1 ± 0.4*	*1.6 ± 0.3*	*20 ± 6*
(PEO-OC_9)-PPV	*0.81 ± 0.05*	*2.5 ± 0.4*	*0.8 ± 0.1*	*31 ± 7*
diPEO-PPV	*0.28 ± 0.02*	*5.0 ± 0.8*	*1.3 ± 0.1*	*32 ± 4*

Table 2.7:
Corrected mobility values of annealed samples and as-prepared samples. The mobility decreased after annealing as well as the resistance ratio r

The ratio r between series resistance and sheet resistance drops by a factor 4 to 12 for the PEOs. This indicates that indeed the contacts were improved by annealing. For OC_1C_{10}-PPV an improvement was not detectable within the standard deviation.

3. Space-Charge Limited Current Measurements

In this chapter, sandwich structures are characterised by means of I-V measurements. Such devices are expected to exhibit a space-charge limited current (SCLC). The mobility of the polymer and the built-in voltage can then be extracted by applying the Mott-Gurney law. First, the basic theory is explained and then it is extended to a field-dependent mobility. Finally, the experimental results are presented and discussed.

A major advantage of SCLC measurements performed on sandwich structures is, that the geometry is close to that of solar cells, which are ultimately the objective of the present work. Both the film thickness and the direction of current flow (perpendicular to the polymer film instead of in-plane for FETs) are identical to the condition found in solar cells. Therefore, it is assumed that the extracted material parameters are closer to the effective parameters of real devices.

3.1. Theoretical Introduction

For the following derivation of an expression for the space-charge limited current, a one-dimensional situation is assumed with two parallel planar electrodes. The space in between the electrodes is filled with the polymer under investigation. The work functions of the electrodes are chosen in such a way that the positive electrode can inject charges (in this case holes) into the HOMO of the polymer, while the other electrode collects these charges but does not inject electrons, i.e. a hole-only device is assumed. Figure 3.1 depicts the layout (left hand side) and the equivalent circuit (right hand side) of such a structure.

Note, that the assumptions made above, are very similar to the situation in a thermionic vacuum tube, from which the concept of space-charge limited current origins.

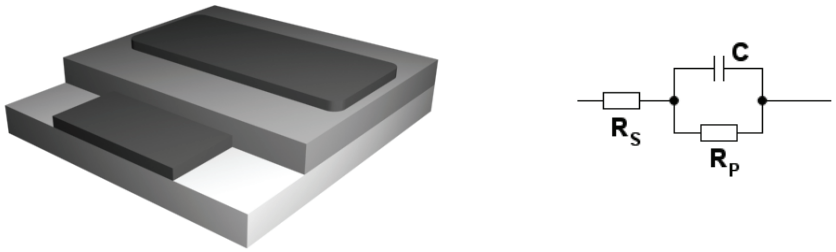

Figure 3.1:
Device layout (left hand side) and equivalent circuit (right hand side) of the sandwich structures studied in this chapter. The device consists of a substrate (white), two electrodes (dark grey) and the polymer under investigation (light grey). The intersection of the two electrodes defines a capacitor with capacity C and resistance R_P. The series resistance R_S depicted in the equivalent circuit represents all additional voltage drops.

The Poisson equation relates the charge concentration ρ and the permittivity ε of the polymer to the divergence of the electric field:

$$\frac{dE}{dx} = \frac{\rho}{\varepsilon} \tag{3.1}$$

In the ideal case, there are no traps, then the current density j is given by:

$$j = \rho \cdot \mu \cdot E \tag{3.2}$$

Combining equation (3.1) and (3.2) to eliminated ρ one obtains:

$$\frac{dE}{dx} = \frac{j}{\varepsilon \cdot \mu} \cdot \frac{1}{E} \quad \Leftrightarrow \quad \mu \cdot E \, dE = \frac{j}{\varepsilon} dx \tag{3.3}$$

Indefinite integration of the equation yields an expression for the electric field:

$$E(x) = \sqrt{\frac{2 \cdot j}{\varepsilon \cdot \mu} \cdot x} \tag{3.4}$$

In order to determine the potential and thus the voltage, the previous equation has to be integrated again from the injecting electrode x = 0 to the collecting electrode x = d (thickness of polymer film). Solving the result for the current density finally yields the Mott-Gurney law [37, 54, 120, 121]:

$$j = \frac{9}{8} \cdot \varepsilon \cdot \mu \cdot \frac{V^2}{d^3} \tag{3.5}$$

Note, that during the derivation of this equation it was explicitly assumed that the mobility does not depend on the field (see integration of equation (3.3) over dE). This is in general not true and discussed in section 3.3. Further, it was assumed that there are no traps. In a less ideal case, this means that in the Poisson equation the trap density has to be taken into account. For equation (3.5), this means that the mobility value is unique for the given material, i.e. trap concentration. The real mobility value μ_0 for the ideal case would then be given by:

$$\mu_0 = \frac{n_0(x) + n_T(x)}{n_0(x)} \cdot \mu \tag{3.6}$$

with the trap concentration $n_T(x)$ and the concentration of free charge carriers $n_0(x)$ [64, 108].

The voltage V in equation (3.5) is usually not equal to the applied voltage, since several voltage drops before and after the channel must be taken into account. This includes the series resistance of the electrodes and the contact

resistance. These voltage drops are described by the series resistance R_S of the equivalent circuit in figure 3.1 (right hand side). Thus, the voltage in equation (3.5) is replaced by $V\text{-}V_0$, where V_0 represents the voltage drop across R_S.

$$j = \frac{9}{8} \cdot \varepsilon \cdot \mu \cdot \frac{(V - V_0)^2}{d^3} \tag{3.7}$$

3.2. Experimental Details

The samples consisted of a polymer film sandwiched between two palladium electrodes. The three layers were prepared on a glass substrate, which was cleaned the same way as the FET-chips in chapter 2. Below a short summary of the six cleaning steps:

- manual cleaning with a 1:20 soap solution
- ultrasonic bath for 20 minutes in the same solution
- rinsing with deionised water
- ultrasonic bath for 10 minutes in acetone
- 10 minutes cleaning in boiling isopropanol
- UV/ozone treatment for 15 minutes

After cleaning the glass substrate, the bottom electrodes were evaporated. Figure 3.2 shows the layout of the electrodes. First two stripes of palladium with a width of 2.5mm were evaporated (left hand side). Then after spin coating, the polymer the top electrodes were evaporated (right hand side). For further details, see appendix 10.1.2.

The polymer layer was applied by spin coating a thin film from solution. The specific conditions for preparation of the solutions and spin coating are listed in the appendix 10.1.2. The spin coating conditions were chosen to yield

reasonably thick films to avoid shorted devices.

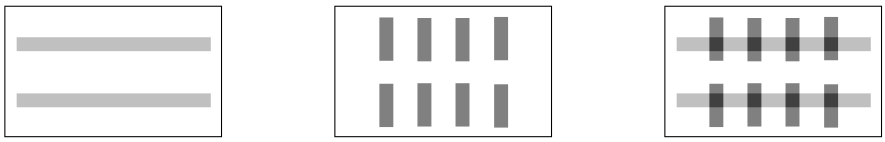

Figure 3.2:
Layout of the bottom electrodes (left hand side) and top electrodes (middle). The intersections of the electrodes (right hand side) define eight capacitors with a surface area of 2.5mm × 2.5mm each.

After spin coating, the samples were transferred into the evaporator again. During evacuation to a base pressure of 10^{-6}mbar, remaining solvent could evaporate, hence no additional storage in vacuum was necessary. Figure 3.2 (middle) depicts the layout of the top electrodes. The intersection of one top electrode with the corresponding bottom electrode defined a capacitor with the previously spin coated polymer film as dielectric (see right hand side of figure 3.2). The eight capacitors had a surface of 2.5mm × 2.5mm and a spacing given by the thickness of the polymer film. Note, that because of the large ratio between the lateral dimension ($\sim 10^{-3}$m) and the spacing ($\sim 10^{-7}$m) the structure can be treated as a parallel plate capacitor with a homogeneous electric field.

Before performing the actual measurement, chlorobenzene was used to remove the polymer from the four ends of the palladium stripes. Then silver paste was applied on the four ends of the bottom electrode and the eight pads of the top electrode to ensure good contact. For the measurement, the sample was placed in a holder and both locked in position and contacted with spring contact probes. Then holder and sample were placed in a metallic box for electrical shielding and in order to protect it from ambient light. Subsequently every two electrodes defining a capacitor were coaxially connected to a Keithley 2400 sourcemetre. The voltage was swept from -10V to +10V in 0.2V steps and the resulting current was acquired.

3.3. Impact of Field Dependence on SCLC

Equation (3.5) holds only true for a constant mobility μ. However, it was already noted in the previous chapter that the mobility is field-dependent. Since the voltage and thus the electric field are swept during measurement, applying equation (3.5) renders wrong results.

3.3.1. Empiric Approach

The most commonly adopted approach [107, 108] to incorporate the field dependence is by replacing the constant mobility μ by expression (1.7):

$$j = \frac{9}{8} \cdot \varepsilon \cdot \mu_0 \cdot e^{\sqrt{\frac{V-V_0}{d \cdot E_0}}} \cdot \frac{\left(V - V_0\right)^2}{d^3} \tag{3.8}$$

Of course, this is not correct since in the derivation of the Mott-Gurney law it was explicitly assumed that μ does not dependent on the electric field. To assess the validity of this empiric approach, it was compared with other methods of accounting the field dependence.

3.3.2. Extended Approach

The derivation of the Mott-Gurney law holds true until equation (3.3). However when calculating the indefinite integral the field dependence of μ is now taken into account:

$$\int \mu\left(E\right) \cdot E \, dE = \int \frac{j}{\varepsilon} \, dx \tag{3.9}$$

If expression (1.7) is assumed for μ (E), both integrals can be calculated:

$$2 \cdot E_0 \cdot \mu_0 \cdot e^{\sqrt{\frac{E}{E_0}}} \cdot \left[E \cdot \left(\sqrt{\frac{E}{E_0}} - 3 \right) + 6 \cdot E_0 \cdot \left(\sqrt{\frac{E}{E_0}} - 1 \right) \right] = \frac{j}{\varepsilon} \cdot x \qquad (3.10)$$

Following the previous derivation, this equation has to be solved for the electric field E(x) and then integrated from the injecting to the collecting electrode. However, equation (3.10) cannot be solved analytically. Therefore, two alternative approaches are proposed.

Going back to equation (3.9) the definite integral is calculated:

$$\int_0^{E_C} \mu(E) \cdot E \, dE = \int_0^d \frac{j}{\varepsilon} \, dx \qquad (3.11)$$

and solved for the current density j:

$$j = \frac{2 \cdot E_0 \cdot \varepsilon \cdot \mu_0}{d} \cdot \left[e^{\sqrt{\frac{E_C}{E_0}}} \left\{ E_C \cdot \left(\sqrt{\frac{E_C}{E_0}} - 3 \right) + 6 \cdot E_0 \cdot \left(\sqrt{\frac{E_C}{E_0}} - 1 \right) \right\} + 6 \cdot E_0 \right] \qquad (3.12)$$

If the electric field at the collecting electrode E_C was known, the measurement data could be fitted directly to equation (3.12). As a first attempt, it is assumed that the electric field at the collecting electrode is equal to the average electric field:

$$E_C = \frac{V - V_0}{d} \qquad (3.13)$$

Then the current density can be written as a function of the applied voltage V. However, this average field approach underestimates E_C, because the electric

field increases from the injecting electrode to the collecting electrode and reaches its maximum at the collecting electrode. Thus averaging the electric field yields a value that is smaller than the true value of E_C. In reference [122], an analytical expression for the electric field at the collecting electrode is derived (for details see appendix 10.2.4):

$$E_C = \frac{V - V_0}{d} \cdot \left(1 + \frac{1}{\frac{d \ln j}{d \ln V}} \right) \tag{3.14}$$

Here and in equation (3.13) the applied voltage V is again corrected for possible voltage drops before and after the channel.

In the following section, all three approaches are applied to the measurement data of diPEO-PPV and the most suitable one is then used for the remaining PPVs.

3.4. Comparison of Extraction Methods

The measurement data of a sandwich structure prepared from diPEO-PPV was first fitted to the empiric model (see figure 3.3). For the permittivity, the value from table 5.1 was used. The thickness of the film and thus the spacing of the capacitor was 108nm (see table 10.4). From a least-square fit of equation (3.8), an offset voltage V_0 of ~2.2V was obtained. Since both electrodes were made of the same material, the offset is mainly addressed to the series resistance of the palladium electrodes. Therefore, V_0 must be interpreted as an average voltage drop, since the actual voltage drop would depend on the applied voltage V and the ratio between film resistance and series resistance. The characteristic electric field E_0 which describes the field dependence of the mobility lies in the range of 37MV/m, hence the field dependence is quite low compared to the values for other PPVs determined in the previous chapter (see table 2.6). It is suspected that this is the reason why in section 2.4 no field dependence was observed for diPEO-PPV. The applied electric field then was only 0.5MV/m compared to up to ~100MV/m now. The hole mobility of $6.2 \cdot 10^{-7} cm^2/Vs$ is of the same order of magnitude as the value determined

from FET measurements. However, it must be noted that for the FET measurements the current flow was in the plane of the polymer film, whereas now the current flow is perpendicular to the film plane. Hence, mobility values are not necessarily comparable, especially when ordering of the polymer chains or even crystallisation is expected [85]. Further, the characterised films have a thickness, which is at least one order of magnitude lower than the studied FET structures.

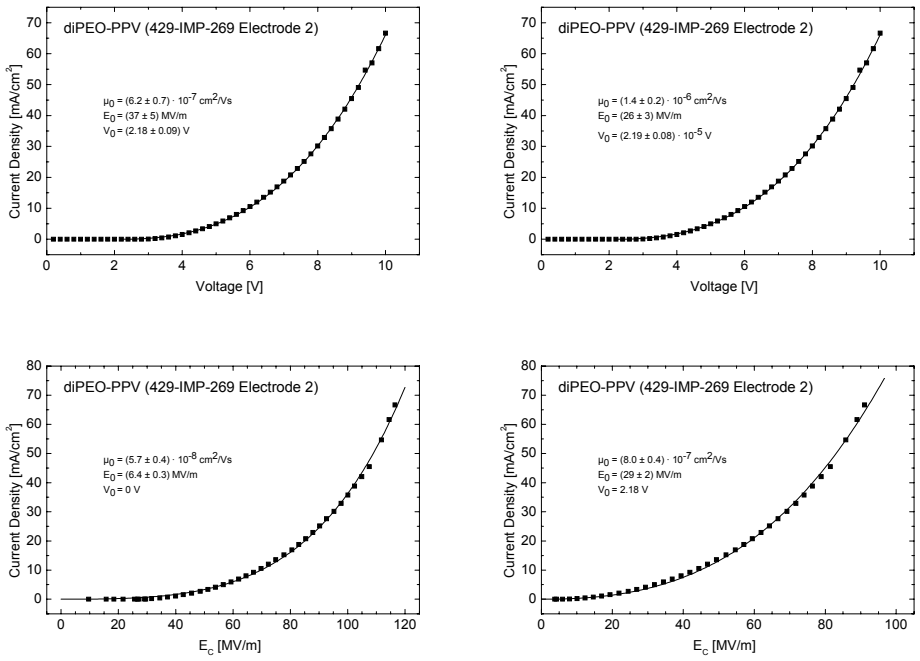

Figure 3.3:

Comparison of the fit results for the four discussed extraction methods. While the empiric approach (upper left plot) and the average field approach (upper right plot) give comparable offset voltages V_0, the latter overestimates the mobility. The approach with corrected E_C (lower left plot) and V_0=0V in contrast underestimates the mobility. Using the same approach and the offset voltage of the empiric approach finally gives a result, which is comparable with the empiric approach.

Next, the approaches with an extended treatment of the field-dependent mobility are fitted to the data (see figure 3.3). Figure 3.4 depicts a comparison of the three different approaches to calculate the electric field at the collecting electrode E_C. As already explained, equating E_C with the average electric field (see equation (3.13)) underestimates the electric field, especially for larger voltages. Using the analytical expression for E_C (see equation (3.14)) without taking the offset voltage V_0 into account overestimates E_C, because the voltage drop across the series resistance is neglected. Finally correcting the value of E_C also for the voltage drop V_0, gives correct results over the entire voltage range.

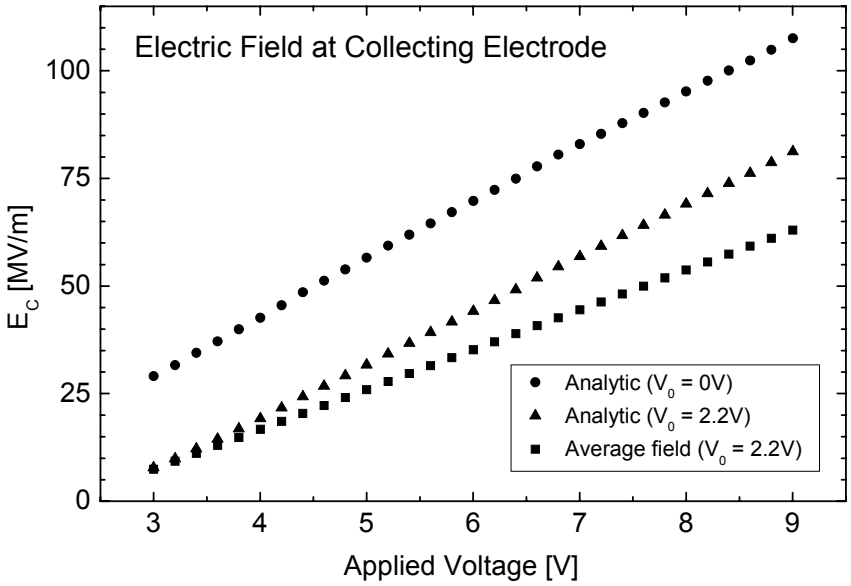

Figure 3.4:

Comparison of the electric field at the collecting electrode E_C for three different approaches. Taking the average field (squares) underestimates the electric field especially for larger voltages. Using the analytical approach without taking the offset voltage into account (circles) overestimates the electric field. Finally, the analytical approach in combination with the offset voltage (triangles) gives correct results for the entire voltage range

Note, that the offset voltage cannot be extracted from the analytical approach in reference [122], therefore the same value as obtained from the empiric approach was used.

Table 3.1 lists the results of all approaches employed. While the average field approach yields within one standard deviation an identical offset voltage V_0 as the empiric approach, the mobility is significantly larger. This was expected, since E_C is underestimated, resulting in an overestimation of the mobility ($j \sim \mu_0 \cdot E_C$). The characteristic electric field E_0 is expected to be comparable in both cases, because it is independent from the assumed value of E_C. This is confirmed by the fit results.

Next, the corrected value of equation (3.14) is used for E_C. First, the offset voltage V_0 is neglected, since it cannot be extracted from the model itself. The overestimation of E_C consequently leads to an underestimation of the mobility and the characteristic field. Finally, the same approach is employed by using the offset voltage as obtained from the empiric approach. The extracted mobility value is slightly higher than the one from the empiric model.

Method	**μ_0 [10^{-7} cm^2/Vs]**	**E_0 [MV/m]**	**V_0 [V]**
Empiric	*6.2 ± 0.7*	*37 ± 5*	*2.18 ± 0.09*
Average field	*14 ± 2*	*26 ± 3*	*2.19 ± 0.08*
Analytical V_0 = 0V	*0.57 ± 0.04*	*6.4 ± 0.3*	*0*
Analytical V_0 = 2.2V	*8.0 ± 0.4*	*29 ± 2*	*2.18*

Table 3.1:
Comparison of the four different approaches employed to extract the mobility μ_0, the characteristic electric field E_0 and the offset voltage V_0.

It is concluded that the empiric approach yields reasonably good results for all fit parameters. However, for more precise values and smaller relative errors, it is suggested to refit the measurement data with the analytical expression for E_C, corrected for the previously determined offset voltage.

3.5. Experimental Results

3.5.1. Field-Dependent Mobility

The method suggested in the previous section is now applied to the measurements of the other three PPV derivatives. In summary, first the empiric model is fitted to extract the offset voltage V_0. Then this voltage is used to fit equation (3.12) with equation (3.14) used as expression for the electric field at the collecting electrode. The derivative appearing in equation (3.14) is calculated numerically from the measurement data, thus introducing a rather high noise level for the x-axis (E_C). Nevertheless, figure 3.5 shows a general good agreement between measurement data (squares) and fit result (curves). The mobility values ranged from $\sim 0.3 \cdot 10^{-6} cm^2/Vs$ for PEO-PPV

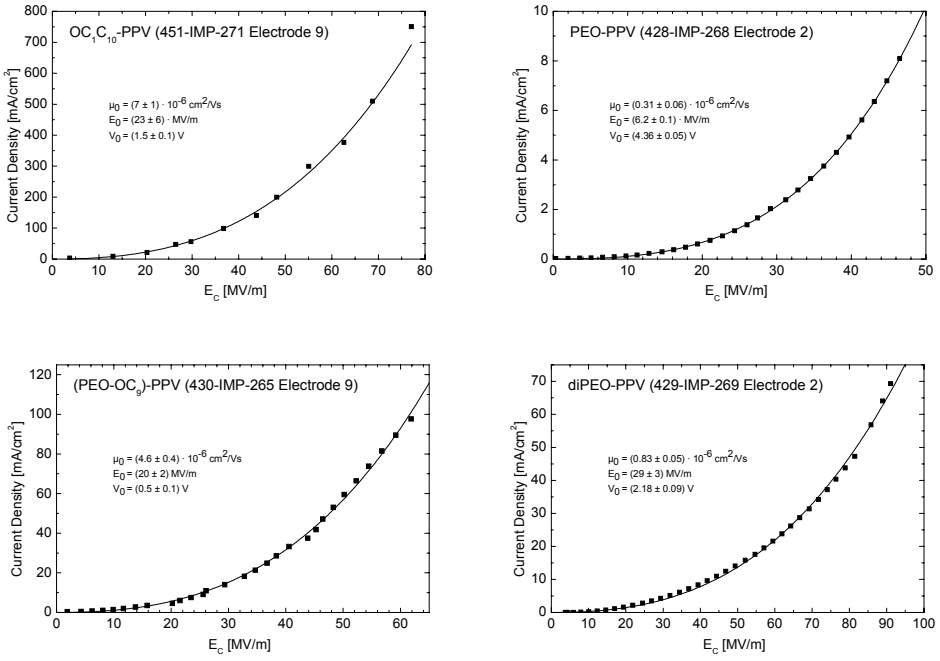

Figure 3.5:
Measured current density (squares) and fit (curves) for the PPVs studied.

to $7 \cdot 10^{-6} cm^2/Vs$ for OC_1C_{10}-PPV. The latter exhibited as only commercially purchase material the highest mobility. This is consistent with the results of chapter 2, which were obtained from FET measurements. The other two PPVs were in between, where diPEO-PPV ($\sim 0.8 \cdot 10^{-6} cm^2/Vs$) was more comparable with PEO-PPV and (PEO-OC_9)-PPV ($4.6 \cdot 10^{-6} cm^2/Vs$) was in the range of OC_1C_{10}-PPV.

The characteristic field E_0, which is a measure for the field dependence of the mobility, was significantly higher than the values determined from FET measurements. Instead of several kilovolts per metre, the values were all in the range of megavolts per metre. Notably the value for PEO-PPV was somewhat lower then for the other PPVs (~6MV/m instead of some 20MV/m). A comparison with FET measurements suggests that the transport is less dispersive perpendicular to the spin coated film than in-plane. However, an alignment of the polymer is expected in-plane, rather than perpendicular. Thus if the charge transport is not isotropic, it is expected to be hindered in perpendicular direction, leading to a smaller mobility value. Since the measurement results contradict this interpretation, it is concluded, that the observed difference between FET measurements and SCLC measurements is not caused by the different directions of charge transport.

Therefore, it is proposed that the observed effect is attributed to the total distance the charges cover when drifting from one electrode to the other [43]. Note, that the covered distance of the charge carriers in these devices is given by the film thickness (~ 100nm) in contrast to the channel length for FET

Polymer	**μ_0 [10^{-6} cm^2/Vs]**	**E_0 [MV/m]**	**V_0 [V]**
OC_1C_{10}-PPV	*7 ± 1*	*23 ± 6*	*1.5 ± 0.1*
PEO-PPV	*0.31 ± 0.06*	*6.2 ± 0.1*	*4.36 ± 0.05*
(PEO-OC_9)-PPV	*4.6 ± 0.4*	*20 ± 2*	*0.5 ± 0.1*
diPEO-PPV	*0.83 ± 0.05*	*29 ± 3*	*2.18 ± 0.09*

Table 3.2:
Zero-field mobility μ_0, characteristic electric field E_0 and offset voltage V_0 as obtained from the above-described fitting procedure.

structures (several micrometres).

The extracted offset voltages ranged from ~0.5V to ~4.4V. The variation of the values reflects the position of the devices on the substrate relative to the point where the palladium electrodes were contacted, which determines the absolute value of the series resistance.

4. Impedance Spectroscopy

In this chapter, the sandwich structures of the previous chapter are characterised by means of impedance spectroscopy. After an introduction to the theoretical background of the measurement technique, several material parameters are extracted. First, the field-dependent mobility is calculated, both from the negative differential susceptance and from the impedance directly. The second approach yields also information about the degree of dispersion.

Since impedance spectroscopy is performed on the identical devices as the SCLC measurements, the two techniques share the same advantages, i.e. the device layout is close to the structure of actual devices as organic LEDs, solar cells, etc. and the charge transport is perpendicular to the spin coated film.

4.1. Introduction

Figure 3.1 (right hand side) shows the equivalent circuit of an ideal sandwich device known as Randle's circuit. Two planar electrodes form a capacitor with capacitance C and the polymer under investigation as dielectric. Since the polymer is not completely insulating, a resistor R_P is placed in parallel to the capacitor. Further, all occurring series resistances are combined in R_S. Upon applying an AC voltage with circular frequency ω, the device exhibits an impedance Z given by the following equation:

$$Z = R_s + \frac{1}{\frac{1}{R_P} + i \cdot \omega \cdot C} \tag{4.1}$$

with the imaginary unit i. Equivalently the AC response of the device can also be described by the admittance Y:

$$Y = \frac{1}{Z} = G + i \cdot B \tag{4.2}$$

Decomposing the complex admittance into real part and imaginary part, the conductance G and the susceptance B are obtained. For the given equivalent circuit, it can be easily shown that plotting the imaginary part against the real part yields a semicircle (see right hand side of figure 4.1). The semicircle has two roots at R_S (high frequencies) and R_P+R_S (low frequencies). From the circular frequency at the maximum $\omega_{max,}$ the capacitance C can be calculated:

$$C = \frac{1}{\omega_{\max} \cdot R_P} \tag{4.3}$$

Knowing this, all three parameters appearing in the equivalent circuit can be extracted. However, it is more accurate to fit equation (4.1) directly to the measurement data and thus making use of all data points rather than only the two roots and the maximum.

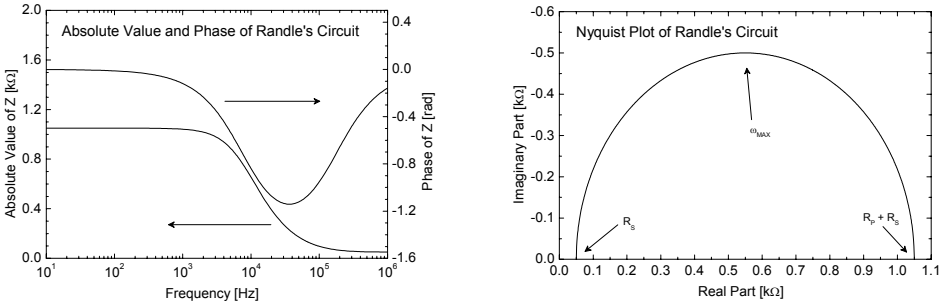

Figure 4.1:
Absolute value and phase (left hand side) and Nyquist plot (right hand side) of an ideal sandwich structure with R_S = 50Ω, R_P = 1kΩ and C = 20nF.

The charge carrier mobility of the polymer under investigation can be extracted by different methods. First, it is demonstrated that the mobility can be determined from the negative differential susceptance. Then it is shown that a first-principle approach can also be applied.

4.2. Negative Differential Susceptance

4.2.1. Theoretical Introduction

As pointed out by equation (4.2), the admittance Y is an equivalent description of the devices' AC response. In reference [120], it is proposed to extract the charge carrier mobility from the negative differential susceptance –ΔB:

$$-\Delta B = -B + \omega \cdot C_{ref} \tag{4.4}$$

As shown in reference [120] there are several reasonable choices for the references capacitance C_{ref}, among which the capacitance of the device measured at the negative value of the built-in voltage. In this work, the capacitance at a bias voltage of 0V was used. Since the material of both electrodes is identical (palladium), the two choices coincided for the studied devices.

Plotting the negative differential susceptance against the frequency, a maximum can be located at a frequency ν_{max}. The maximum originates from different responses of the charge carriers to the AC voltage. For frequencies smaller than $\nu_{max,}$ the charge carriers increase the capacitance of the device, while for frequencies bigger than ν_{max}, the charge carriers lag behind, leading to a negative inductive contribution. The frequency of the maximum corresponds to a characteristic time τ_{max}:

$$\tau_{\max} = \frac{1}{\nu_{\max}} \tag{4.5}$$

This characteristic time is related to the transit time of the charges in the DC case. In literature [34, 120], a correction factor of 0.56 is usually applied:

$$\tau_{DC} \approx 0.56 \cdot \tau_{\max} \tag{4.6}$$

In case of non-dispersive transport, τ_{DC} is equal to τ_{max}, hence the correction factor would be one. In section 4.3.2, the correction factor will be calculated from a first-principle approach. Once the transit time is known, the mobility can be calculated from its very definition:

$$\mu_{DC} = \frac{d^2}{\tau_{DC} \cdot V} \tag{4.7}$$

with the applied bias voltage V and the thickness d of the polymer film.

4.2.2. Experimental Details

As already mentioned the same devices as in chapter 3 were characterised. However instead of connecting the electrodes to a sourcemetre, they were connected to an impedance spectrometer (HP 4284A). For several fixed DC bias voltages ranging from 0V up to 10V, the frequency of an AC voltage was swept from 20Hz to 1MHz. The effective value of the AC voltage was set to 50mV. Note, that in order to apply the described method, the AC voltage should be negligible compared to the bias voltage. To ensure a good signal to noise ratio, the integration time was set to the highest value available and the signal was averaged over several measurements (usually up to 9). Dedicated software (Princeton Applied Research ZSimpWin 3.10) was used to fit a Nyquist plot of the measurement data to Randle's circuit. From the extracted parameters R_S, R_P and C, only the series resistance was used for the further calculations. In order to take voltage drops across the series resistance into account, R_S was subtracted from the real part of the impedance. For the susceptance this lead to a corrected value of:

$$B' = -\frac{\mathrm{Im}(Z)}{\left[\mathrm{Re}(Z) - R_S\right]^2 + \mathrm{Im}(Z)^2} \tag{4.8}$$

The fitted capacitance of the 0V case was used together with the previous expression to calculate the negative differential susceptance from equation (4.4). In order to extract an accurate value for the maximum, a third order polynomial fit was constrained to an interval around the maximum. The determined frequency was then converted into the characteristic time and corrected by equation (4.6) to give the DC transit time. Finally, the mobility was calculated from expression (4.7). Note, that for V the applied voltage was used, since the voltage drop at R_S was already taken into account by using B' rather than B.

4.2.3. Results

Figure 4.2 shows an example plot of the negative differential susceptance of diPEO-PPV. Around the maximum, a third order polynomial fit was applied to determine ν_{max}. The maximum is well pronounced and shifts as expected for larger bias voltages to bigger frequencies. If the voltage is set too high, the transit time becomes shorter than 0.56µs, which corresponds to the maximal applicable frequency 1MHz. Thus, it is important to choose the device geometry and the bias voltage properly to ensure a transit time that lies within the measurement range. However, even then it is not guaranteed, that the negative differential susceptance exhibits a maximum. For the PEO-PPV sample, for instance no maximum was observed. A possible reason is discussed later in section 4.3.4.

Figure 4.3 depicts the measured mobility values of the remaining three PPVs. The curves indicate a least-square fit of equation (1.7). Table 4.1 lists the resulting fit parameters. While the values for the characteristic electric field are comparable with the results of SCLC measurements (see table 3.2), the mobility values of the two PEOs seem to overestimate the mobility by two orders of magnitude. An explanation is given later in section 4.3.4. The mobility of OC_1C_{10}-PPV however is in the range of the SCLC result.

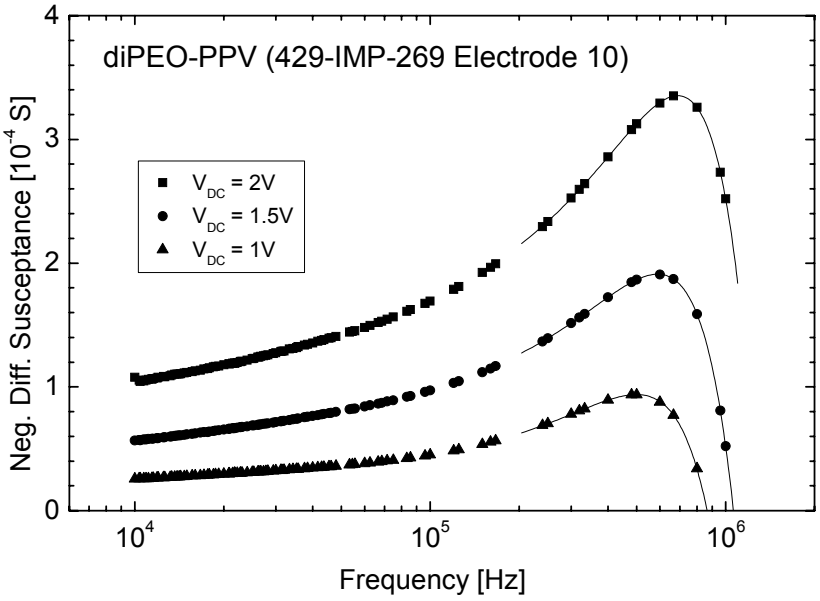

Figure 4.2:

Negative differential susceptance of diPEO-PPV for three different bias voltages. The curves indicate a third order polynomial fit around the maximum.

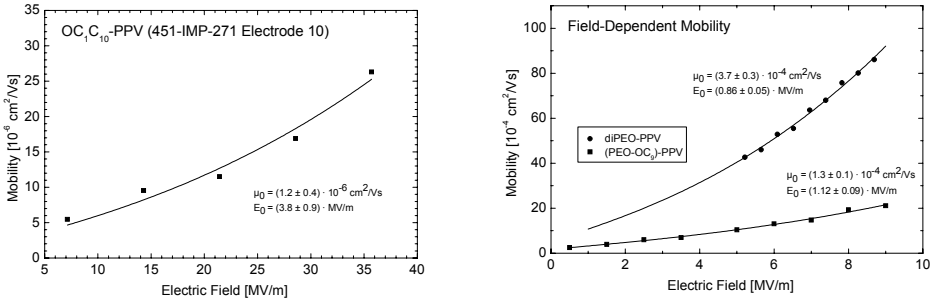

Figure 4.3:

Field-dependent mobility of OC_1C_{10}-PPV (left hand side) and two PEOs (right hand side). The curves indicate a least-square fit of equation (1.7).

Polymer	μ_0 [cm^2/Vs]	E_0 [MV/m]
OC_1C_{10}-PPV	*(1.2 ± 0.4) · 10^{-6}*	*3.8 ± 0.9*
(PEO-OC_9)-PPV	*(1.3 ± 0.1) · 10^{-4}*	*1.12 ± 0.09*
diPEO-PPV	*(3.7 ± 03) · 10^{-4}*	*0.86 ± 0.05*

Table 4.1:
Fit parameters for the three PPVs, which exhibited a maximum in the negative differential susceptance.

From the results it can be concluded, that the presented extraction technique does not yield fully reliable mobility values. A better approach is discussed in the following section.

4.3. First-Principle Approach

In the previous section, the mobility was extracted via the negative differential susceptance. As discussed the applied method has several downsides. Especially the assumption that the correction factor is identical for all materials is questionable, since it describes the degree of dispersion of the charge transport. Hence, it should vary from material to material. In this section, an alternative approach is pointed out.

4.3.1. Theoretical Introduction

In reference [123], a derivation is given for the impedance of a sandwich device. The derivation assumes a large DC voltage with a small AC perturbation. By separating DC and AC contribution a partial differential equation is obtained, which can be solved to yield an analytical expression for the impedance [123, 124]:

$$Z(\Omega) = \frac{\tau_{DC}}{C_{geo}} \cdot \frac{1}{\Omega^3} \cdot \left[\tfrac{9}{8} \cdot i \cdot \tilde{\mu}^2(\Omega) \cdot \left\{ 1 - e^{-\frac{4}{3} \cdot i \cdot \frac{\Omega}{\tilde{\mu}(\Omega)}} \right\} + \tfrac{3}{2} \cdot \tilde{\mu}(\Omega) \cdot \Omega - i \cdot \Omega^2 \right] \quad (4.9)$$

with the DC transit time τ_{DC} and the geometric capacitance C_{geo}. Further, the normalised circular frequency is defined as:

$$\Omega = \omega \cdot \tau_{DC} \tag{4.10}$$

Finally, a normalised mobility is introduced by the expression:

$$\tilde{\mu}(\Omega) = \frac{\mu(\Omega)}{\mu_{DC}} \tag{4.11}$$

For a detailed derivation see appendix 10.2.5 and reference [123]. In order to evaluate equation (4.9) an empiric model for the normalised mobility is used [123, 124]:

$$\tilde{\mu}(\Omega) = 1 + M \cdot (i \cdot \Omega)^{1-\alpha} \tag{4.12}$$

M and α are two parameters, which describe the degree of dispersion. For non-dispersive transport M vanishes and α equals 1. Hence, the normalised mobility is unity.

4.3.2. Effect of Dispersive Transport

In section 4.2 it was mentioned that a correction factor has to be applied in order to convert the characteristics time τ_{max} of the negative differential susceptance to the DC transit time. The factor 0.56 normally used in literature [34, 120], can be determined from the analytical expression (4.9) of the impedance.

For the following simulation a device was assumed with a relative permittivity of 3, a electrode surface of 25mm^2 and a film thickness of 100nm, resulting in

a geometric capacitance of ~6.6nF. Further, a DC transit time of 1µs was assumed. The impedance was then evaluated from equation (4.9) and the negative differential susceptance -ΔB was determined. For the calculation of -ΔB, the geometric capacitance was used as reference capacitance. Then the maximum of –ΔB was numerically determined and the resulting frequency (i.e. characteristic time τ_{max}) was compared to the DC transit time, yielding the correction factor.

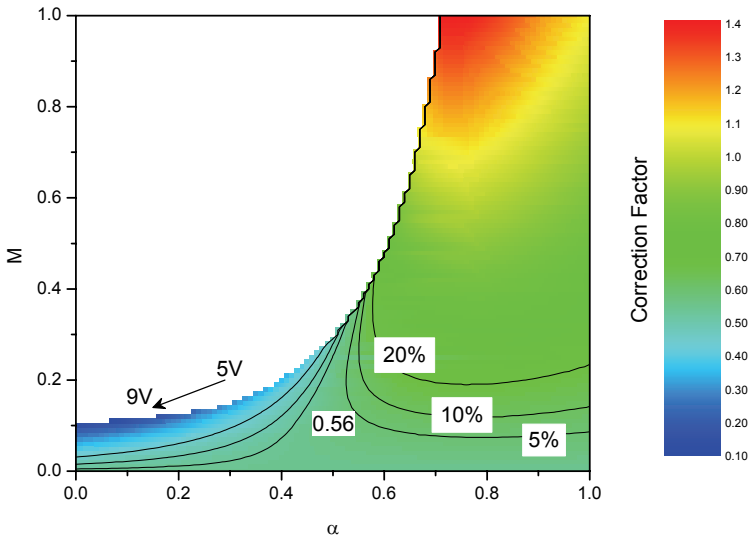

Figure 4.4:
Correction factor for a transit time of 1µs. The contour lines show a deviation of 5%, 10% and 20% from the value usually used (0.56). The arrow indicates the change of the dispersion parameters of PEO-PPV when increasing the DC voltage (see

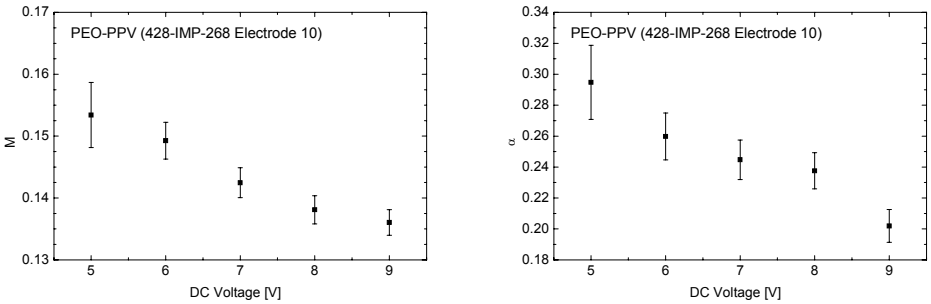

figure 4.6 in section 4.3.4).

Figure 4.4 maps the determined correction factor for different pairs of M and α. The position of the "standard" correction factor is indicated by a label. Further, the contour lines for a deviation of 5%, 10% and 20% from this value are shown. From the map, it is evident that the assumed correction factor is only viable for a small range of dispersion parameters. In order to test to what extend the determined correction factors depend on the initial DC transit time, the same calculation was repeated for transit times of 0.01μs, 0.1μs, 10μs and 100μs. The difference of the largest and smallest value for a given pair of M and α relatively to the value for the 1μs calculation was always less than 0.1%. Hence, the result discussed above is valid for a large range of transit times, extending over five orders of magnitude.

Note, that the white part of figure 4.4 denotes a region where the numerical calculation of the negative differential susceptance and the determination of the maximum become instable. Therefore, no values are available for that area.

4.3.3. Experimental Details

The same devices as in section 4.2 were used. As the model assumes an Ohmic contact, the real part of the impedance was corrected for the series resistance. The values used were obtained from the fits of the Nyquist plot. In order to calculate the geometric capacitance the relative permittivity values of table 5.1 were used. The real and imaginary parts of equation (4.9) were

simultaneously fitted.

4.3.4. Results

Figure 4.5 shows the Nyquist plot (left hand side) and real and imaginary part of the impedance (right hand side). The impedance is already corrected for the series resistance. The curves show the result of the least-square fit. It can be seen that the curves describe the measurement data well.

The extracted fit parameters are listed in table 4.2.

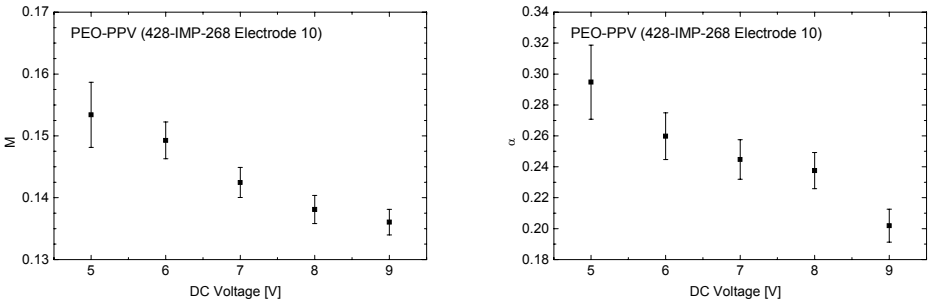

Figure 4.6 depicts the dispersion parameters for several DC bias voltages. Both parameters decrease slightly when increasing the voltage. As mentioned in one of the previous sections the arrow in figure 4.4 indicates the changing correction factor of PEO-PPV, when sweeping the DC bias voltage. Although the dispersion

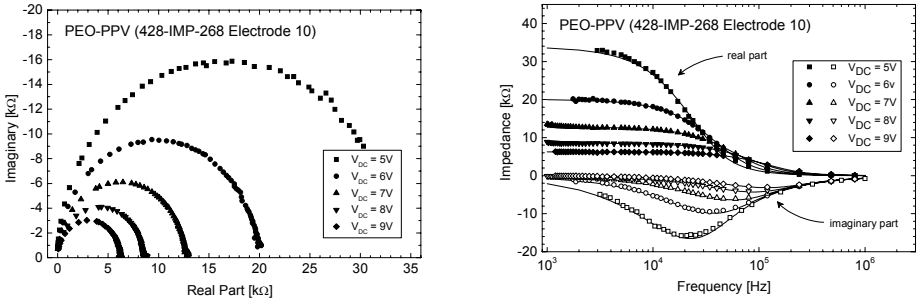

Figure 4.5:

Nyquist plot of the impedance of PEO-PPV for different DC voltages (left hand side). The parallel resistance decreases with increasing voltage, thus scaling the semicircle to smaller size. The real part (filled symbols) and the imaginary part (open symbols) of the impedance in frequency domain are depicted (right hand side). The curves indicate a least-square fit of equation (4.9).

parameters of PEO-PPV are in the non-accessible area of the simulation, it can be concluded, that the correction factor differs significantly from the "standard" value. Hence, the problems when trying to determine the mobility from the negative differential susceptance.

Polymer	**M**	**α**	**μ_0 [10^{-6} cm^2/Vs]**	**E_0 [MV/m]**
OC_1C_{10}-PPV	*0.23 – 0.25*	*0 – 0.06*	*2.6 ± 0.3*	*2.2 ± 0.1*
PEO-PPV	*0.13 – 0.16*	*0.20 – 0.30*	*5.1 ± 0.8*	*0.52 ± 0.04*
(PEO-OC_9)-PPV	*0.12 – 0.15*	*0.10 – 0.17*	*1.1 ± 0.1*	*1.3 ± 0.1*
diPEO-PPV	*0.09 – 0.15*	*0 – 0.06*	*1.3 ± 0.1*	*1.0 ± 0.1*

Table 4.2:
Dispersion parameters M and α, zero-field mobility μ_0 and characteristic electric field E_0. The listed values of the dispersion parameters describe the range for the different DC voltages from 5V to 9V.

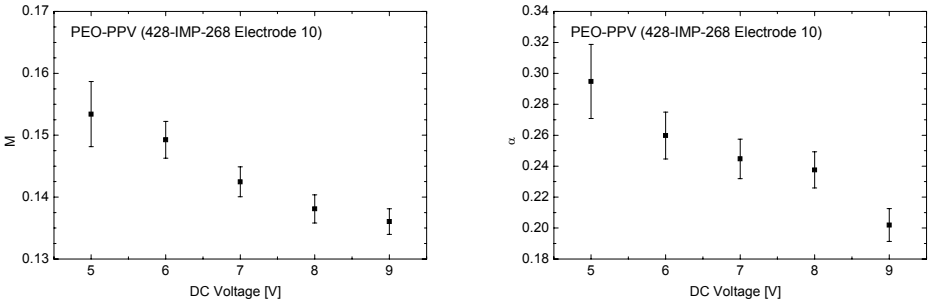

Figure 4.6:
Dispersion parameters M (left hand side) and α (right hand side) for different DC voltages. Both parameters decrease slightly when increasing the voltage.

In figure 4.7, the DC transit time (left hand side) and the mobility are shown. The transit time exhibits the expected decay with increasing voltage. The mobility values were fitted with equation (1.7) to determine the field-independent mobility and the characteristic electric field E_0. Figure 4.8 shows the corresponding plots for all four PPVs. Note, that the measurements of OC_1C_{10}-PPV were performed at much higher fields than for the PEOs. Table 4.2 lists all fit parameters. The mobility values are in the range of $10^{-6}cm^2/Vs$

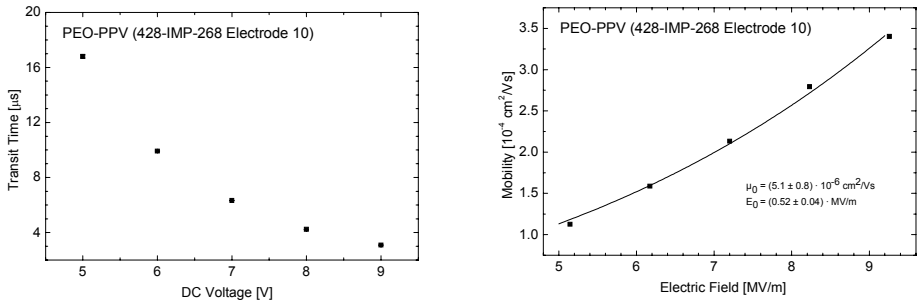

Figure 4.7:
Transit time (left hand side) and field-dependent mobility (right hand side) for PEO-PPV. The mobility increases exponentially as described by equation (1.7). The curve describes a least-square fit of the data.

and the characteristic electric field lies in the range of ~0.5MV/m to ~2MV/m. While the mobility values are comparable to the SCLC results, the characteristic electric field is about a factor of 10 smaller. Except for PEO-PPV the dispersion parameter α is rather small. For some materials and bias voltages, it was even zero. The other dispersion parameter M varied only slightly for different DC bias voltages. This is with the exception of diPEO-PPV, which exhibited the smallest M values, hence a variation of M in the order of the absolute value determined. Further, it was noticed that PEO-PPV gave the highest zero-field mobility and the strongest field dependence. This is in contrast to the results of chapter 3, where PEO-PPV showed a much smaller mobility. The comparatively high dispersion parameter α could be an

explanation, why only PEO-PPV exhibits such a strong deviation from previous results.

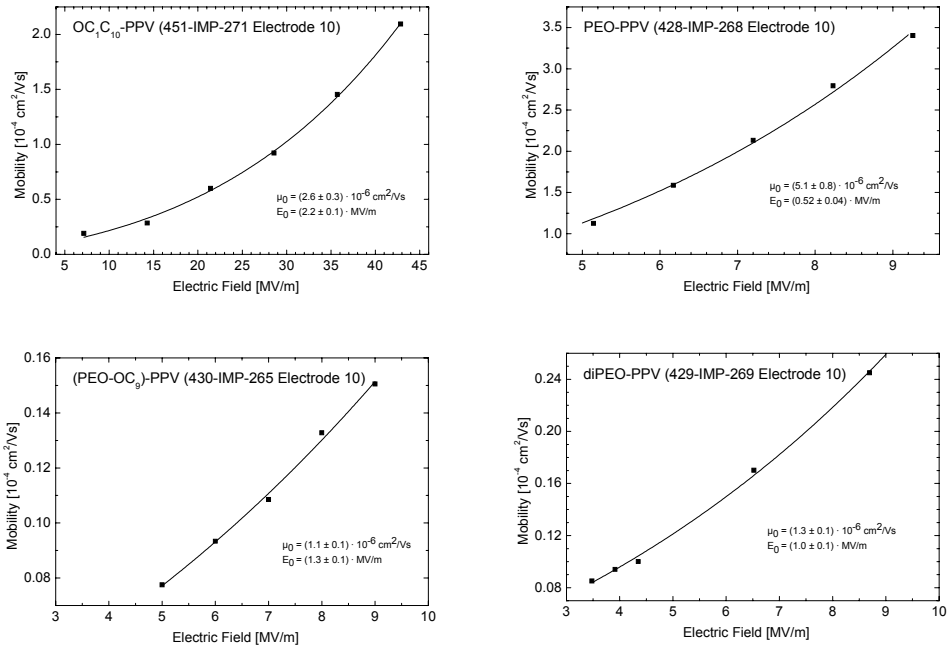

Figure 4.8:
Field-dependent mobility of the four PPVs studied. The curves indicate a least-square fit of equation (1.7).

5. Electrooptical Characterisation and Polarity of PPVs

Another interesting material parameter is the polarity. The polarity is important for the solubility of the material in different solvents. For large-scale industrial production, it is required to use environmentally friendly solvents like alcohols or even water. Since these solvents are very polar, polymers with a high polarity are desirable ("like dissolves like"). Further, the polarity is linked with the relative permittivity. Increasing the polarity, i.e. relative permittivity, therefore decreases the exciton dissociation energy in solar cells, by reducing the Coulomb attraction of the electron-hole pair. In this chapter, the relative permittivity is determined and its impact on the ordering behaviour in polymer films is studied by XRD measurements. Further the optical absorption of the polymers is also characterised in order to assess there usability in solar cells.

5.1. Relative Permittivity

In order to determine the polarity of the four PPVs, the relative permittivity was determined. The permittivity is linked by the Clausius-Mosotti equation with the polarisability [125], hence a measure for the polarity of the polymers. From the chemical structure (see figure 1.3), it is expected that the different side chains of the four PPVs have a significant influence on the polarity.

The capacitance was determined by impedance spectroscopy of sandwich devices similar to the devices studied in the previous chapter. Once the geometric capacity C of the sandwich device is known, the relative permittivity ε_r can easily be calculated from the following equation:

$$C = \varepsilon_0 \cdot \varepsilon_r \cdot \frac{A}{d} \tag{5.1}$$

with the permittivity of vacuum ε_0, the surface A of the capacitor and the

thickness d of the polymer film, i.e. the spacing of the device. In order to increase the accuracy of the extraction method, several devices with varying geometry, i.e. different A/d ratios, where characterised.

5.1.1. Experimental Details

The devices were prepared similarly to the devices of the previous section. However, the bottom electrode consisted of ITO and the top electrode of aluminium. Further the layout depicted in figure 3.2 (right hand side) was replaced by an arrangement with four different widths for the contacts (3mm, 5mm, 7mm and 10mm). The impedance was measured for a bias voltage of 0.8V and an AC voltage of 50mV. The capacitance was then extracted from the imaginary part B of the admittance Y and the circular frequency of the AC voltage:

$$C(\omega) = \frac{B(\omega)}{\omega} \tag{5.2}$$

From the constant part of the plot, the capacitance was determined. Plotting the capacitance values against the ratio A/d of the electrode surface A and the spacing d, the relative permittivity is extracted from the slope of a least-square fit.

5.1.2. Results

Figure 5.1 shows a plot of the capacitance for several A/d ratios. The lines indicate a least-square fit of equation(5.1). The permittivity is then obtained directly from the slope of the curves. The extracted relative permittivity values are given in the plot. The rather apolar OC_1C_{10}-PPV exhibited with ~3 the lowest relative permittivity. Replacing the $OC_{10}H_{21}$ side chain by a PEO side chain, the relative permittivity increases significantly to ~4. Extending the OCH_3 side chain to an OC_9H_{19} side chain increases the relative permittivity only slightly to ~4.1. However, the two values are equal within one standard deviation. Finally, substituting the same side chain by another PEO side chain

further increases the relative permittivity to ~5.5.

It can be concluded that the subsequent substitution of OC_nH_{2n+1} side chains by PEO side chains leads to a significant increase of the polarity of the molecule, i.e. the relative permittivity of the material.

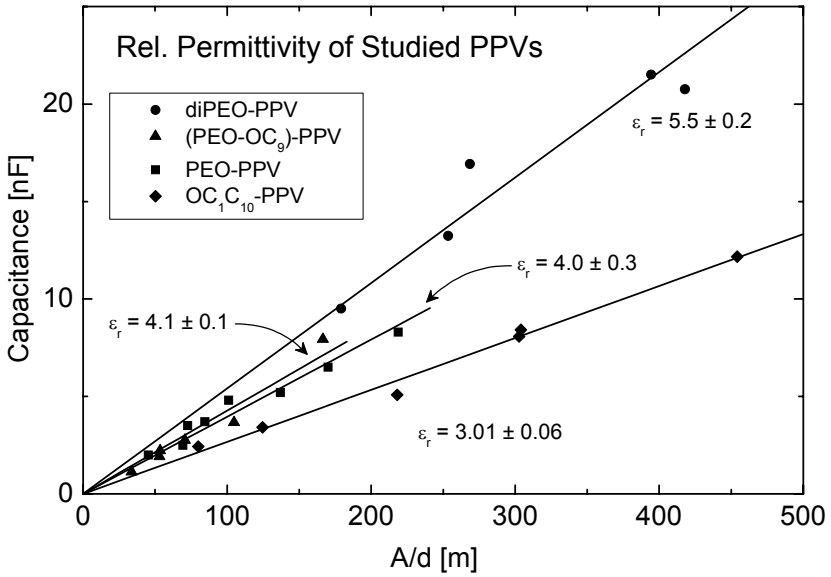

Figure 5.1:
Capacitance of the four studied PPVs depending on the device geometry A/d. The relative permittivity is extracted from the slope of a linear least-square fit.

5.1.3. Theoretical Comparison

In order to assess the validity of the results, it was tried to determine the permittivity theoretically. First, a simple approach was followed, by splitting the polymer and the side chains into their constituting groups. This so-called additive group method is described in reference [126]. The polymer backbone was therefore split into a *p*-phenylene ring, with two double bonded CH groups attached. Further, the side chains were split into the individual oxygen, CH,

CH_2 and CH_3 groups. Then the group contribution V_i to the molar volume V and P_i to the molar dielectric polarisation P was multiplied by the number of occurrences of the group and summed up. The relative permittivity was then calculated by applying the Lorentz-Lorentz equation:

$$\frac{\varepsilon_r - 1}{\varepsilon_r + 2} = \frac{\sum_i P_i}{\sum_i V_i} \tag{5.3}$$

Table 5.1 lists the calculated values along with the measured values. The calculated values do not confirm the observed trend of the measurement. In fact, the values look rather random. Looking at equation (5.3) it is noted that the increasing molar dielectric polarisation is compensated by the increasing molar volume, hence the relative permittivity remains more or less unchanged.

Polymer	Calculation	Measurement
PPV	*2.8*	-
OC_1C_{10}-PPV	*2.5*	*3.01*
PEO-PPV	*2.8*	*4.0*
(PEO-OC_9)-PPV	*2.6*	*4.1*
diPEO-PPV	*2.7*	*5.5*

Table 5.1:
Comparison of the calculated and measured relative permittivity. While the measurement shows a clear trend, the calculations yield rather arbitrary values. As reference, the bare PPV without any side chains was included in the calculations.

Calculating only the molar dielectric polarisation also does not reproduce the observed trend of the measurement. Additional first-principle calculations performed at Silicos[5] lead to the same problems.

It was therefore concluded that additional properties like molecular weight, poly dispersity, ordering, etc. have a strong effect on the macroscopic polarisation and are difficult to predict by taking only the microscopic chemical structure into account.

5.2. Ordering Behaviour of PPVs in Films

In the previous section, it was demonstrated that the relative permittivity increases significantly when adding PEO side chains. It is expected that the increased polarity has an influence on the ordering of the polymer chain through dipole-dipole interaction. In order to study this behaviour x-ray diffraction (XRD) measurements were performed.

5.2.1. Experimental Details

In order to obtain a detectable signal, the polymer film had to be rather thick. To ensure a thick layer in the micrometre range, the polymer solutions were therefore drop cast. Further n-Si (100) substrates were used instead of glass. The crystalline nature of the substrates leads to a well-known background signal, making it easier to analyse the measurement data. The preparation of the samples was identical to the sandwich devices. Although the preparation was done in a nitrogen atmosphere, the measurement itself took place under ambient conditions. The samples were measured at several temperatures, ranging from 30°C to 225°C. The wavelength of the X-rays was 0.154nm.

5.2.2. Results

Figure 5.2 shows the XRD spectra of the four PPVs for several temperatures. Around an angle of $\theta = 2°$ a refraction peak appears, which is increasing at elevated temperatures. The maximum is reached at roughly 170°C. For even higher temperatures, the peak decreases again, probably due to the

[5] Silicos NV (http://www.silicos.com)

decomposition of the polymers. Note, that the height of the peak is a measurement of the intensity of the refracted beam. However, since the intensity depends on the probed volume, the measurement results of samples with different thicknesses and surface areas are not directly comparable. Instead, the position and the width of the peaks were compared. The peak position is linked by Bragg's law with the spacing between the "crystal" planes d. The width is an indication for the size of the ordered domains, which caused the refraction.

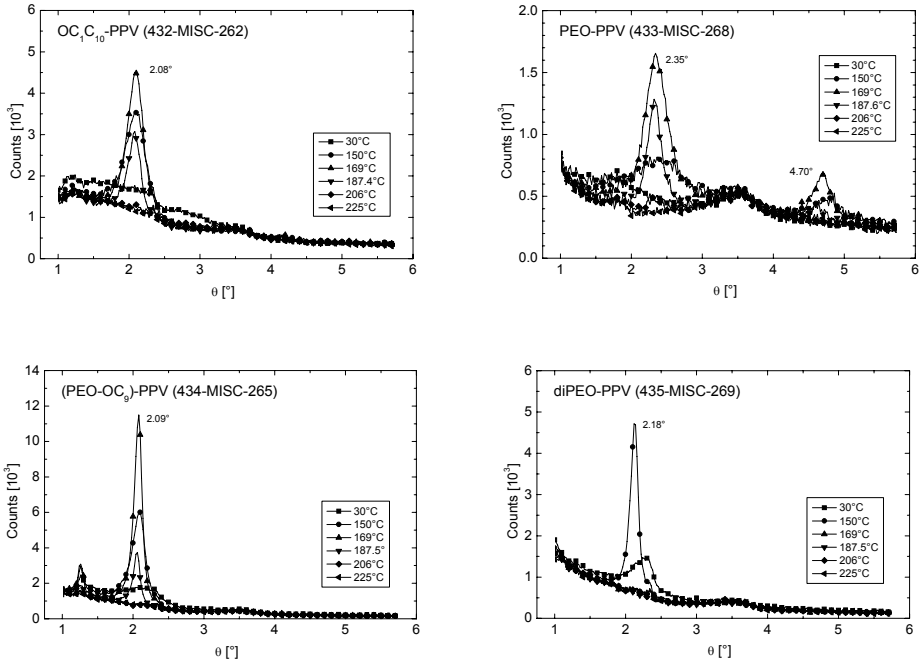

Figure 5.2:

XRD spectra of the four studied PPVs for different temperatures. The peak height increases up to a temperature of ~170°C. For higher temperatures, it decreases again, probably due to decomposition of the polymers. Note that for PEO-PPV a higher order refraction peak was observed.

Table 5.2 lists the extracted parameters. The position was averaged over the results of the different temperatures. While OC_1C_{10}-PPV and (PEO-OC_9)-PPV yielded a similar spacing of the "crystal" planes of around 2.1nm, diPEO-PPV and PEO-PPV showed smaller values of ~2.0nm and ~1.9nm. The width of the peak as obtained from a Gaußian least-square fit increases with increasing temperature. However, at temperatures above ~170°C the peak decreases again, probably due to decomposition of the polymers. The widths in table 5.2 refer to the temperature at which the refraction peak reaches its maximum (usually 169°C).

Polymer	**Thickness [µm]**	**Peak Position [°]**	**d [nm]**	**Peak Width [°]**
OC_1C_{10}-PPV	*2.4*	*2.08*	*2.12*	*0.26*
PEO-PPV	*3.9*	*2.35*	*1.88*	*0.30*
(PEO-OC_9)-PPV	*1.3*	*2.09*	*2.11*	*0.12*
diPEO-PPV	*5.0*	*2.18*	*2.02*	*0.38*

Table 5.2:
Film thickness, position of the first order refraction peak, calculated spacing of the "crystal" planes and width of the peak at the temperature when it reaches the maximum height (usually 169°C).

Figure 5.3 (left hand side) shows a comparison of the peak widths listed in table 5.2 with the relative permittivity. The plot shows a clear trend, which is only interrupted by the value for (PEO-OC_9)-PPV. However, the width is increasing for larger relative permittivity values, which is opposite to the expectation for a dipole-dipole induced ordering. Therefore, another parameter must be more influential than the polarity of the polymer. When plotting the same data against the number of repeating units of the polymer chains, an even more convincing trend is observed (see right hand side of figure 5.3). Obviously, the chain length has a large influence on the ordering of the polymers. (PEO-OC_9)-PPV, which has the shortest chains, exhibits the smallest width, i.e. the largest ordered domains. On the other hand, diPEO-PPV, the

polymer with the longest chains shows the largest width, i.e. the smallest ordered domains. This effect is addressed to the fact that shorter polymers can align more easily. From the two plots it is concluded, that the large differences of molecular mass screen any possible effect of the polarity of the polymers. In section 6.3.1 it will be discussed, whether this effect has also an influence on the charge carrier mobility.

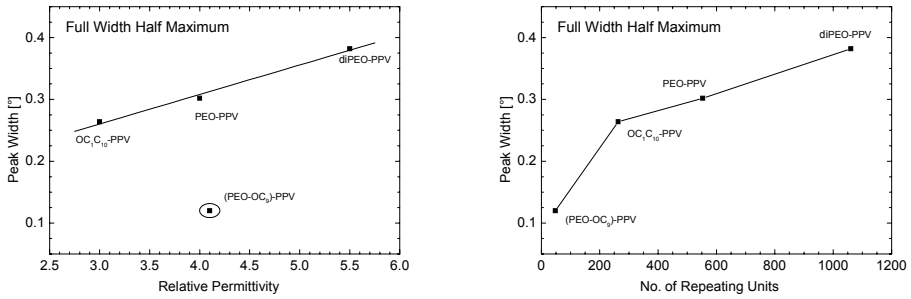

Figure 5.3:
Peak width of table 5.2 plotted against the relative permittivity (left hand side) and the number of repeating units of the polymers (right hand side). The plots suggest that the ordering behaviour depends strongly on the chain length.

5.3. Optical Properties of Polymers

One of the most important properties for solar cells is the absorption coefficient α of the active layer. In order to harvest as much light as possible and yet keeping the film thickness small, a high absorption coefficient is required. In this section, the absorption coefficient of the four studied PPVs is determined by means of reflection and transmission measurements.

5.3.1. Theoretical Background

From the reflection R and the transmission T, the absorption A can be calculated:

$$A = 1 - R - T \tag{5.4}$$

Following Beer's law, the light intensity I decreases exponentially when penetrating a material:

$$I(d) = I_0 \cdot e^{-\alpha \cdot d} \tag{5.5}$$

with the intensity I_0 of the incident light, the penetration depth d and the absorption coefficient α. The relative value of the initial intensity is given by 1 - R (incident intensity corrected for the reflected light). The intensity at depth d, where d is the film thickness, equals T. Hence solving equation (5.5) for the absorption one obtains:

$$\alpha = \frac{1}{d} \cdot \ln\left(\frac{1-R}{T}\right) \tag{5.6}$$

Note, that this equation does not consider multiple reflections. Thus, it tends to overestimate the absorption coefficient.

5.3.2. Experimental Details

The characterised films were spin coated on glass substrates. For a detailed description of the preparation, see appendix 10.1.3. The measurements were performed under ambient conditions. The wavelength-dependent reflection and transmission was measured in 10nm steps from 280nm to 1200nm. Prior to the measurement the lamp (OL 750-L) was given 15 minutes to heat up. For calibration, a white reference target was placed at the output of an integrating sphere. In order to take the absorption of the sample substrate into account, the transmission of a clean glass substrate was first measured, to serve as a reference. To measure the transmission the glass substrate was replaced by the actual sample. Thus using the reference measurement, the transmission of the polymer film was probed. For the reflection measurement, the sample was mounted on a cone, to ensure that transmitted light was not

backscattered. The reference target was then replaced by the sample.

5.3.3. Measurement Results

When calculating the absorption coefficient, it was noticed that the values dropped below zero for large wavelength. In order to correct for this measurement artefact all curves were shifted to a zero baseline, assuming that for larger wavelength the absorption should vanish.

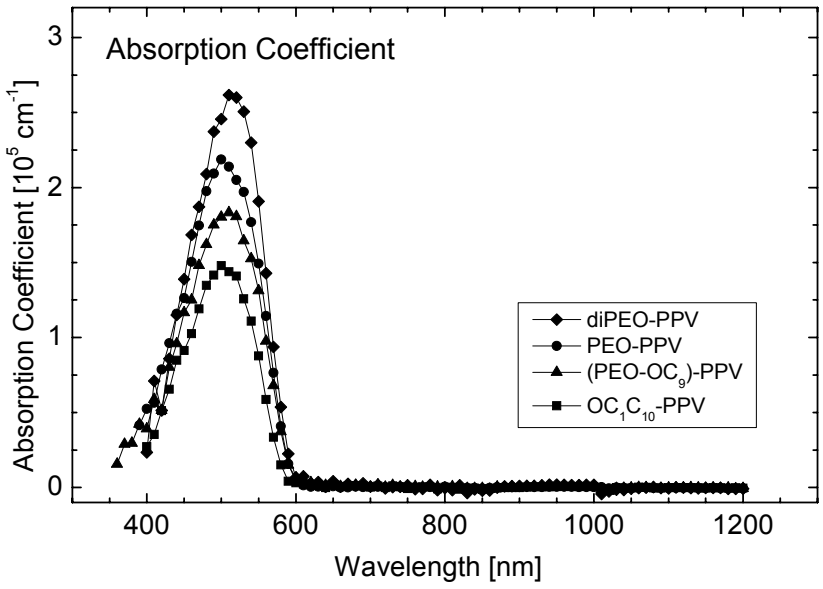

Figure 5.4:
Absorption coefficient of the four studied PPVs. Notably the peak absorption of diPEO-PPV is almost twice as big as for OC_1C_{10}-PPV.

Figure 5.4 shows the result for the four PPVs studied. Notably the peak of the absorption varied almost by a factor of two between the reference material OC_1C_{10}-PPV and diPEO-PPV. It is not clear, which property of the polymer structure induces this large difference. The optical band gap of the four PPVs is

~2.1eV (see table 1.1) which corresponds to a wavelength of ~590nm (onset of the absorption in figure 5.4). Therefore, the optical behaviour should be similar. However, the absorption coefficient was determined from a solid film, hence intermolecular interactions cannot be neglected and may lead to a different optical behaviour due to different side chain interactions. Further, the optical properties can be influenced by strong electron donating or withdrawing side chains [109], as present in the PEOs (compare relative permittivity)[127, 128].

The increased absorption of the PEOs leads to two possible design suggestions. The film thickness of PEO-based solar cells can be reduced without loosing light compared to OC_1C_{10}-PPV-based devices or the absorption of a film of a given thickness can be increased compared to OC_1C_{10}-PPV. In both cases, the performance of PEO-based solar cells should benefit from the improved optical properties.

6. Comparison of Electrical Characterisation Results

In chapter 2, 3 and 4 three different measurement techniques were used to determine the charge carrier mobility. Furthermore, several extraction methods were applied to calculate various material parameters. As a result, a variety of values for the same parameters was obtained for each polymer. In this chapter, all results obtained so far, are summarised and compared. Finally a suggestion is made, how to interpret and evaluate the different values.

6.1. Comparison of FET Results

There are several means of extracting the charge carrier mobility and other parameters from FET measurements. In chapter 2, the mobility was extracted either from the linear regime or from the saturation regime. Depending on the applied model, different assumptions and idealisations were made.

6.1.1. Comparison of Mobility Values

Table 6.1 summarises the mobility values for four different approaches. Extracting the mobility from the transconductance g_m in the linear regime (first column of table 6.1), showed to be the least accurate method, although the linear fit resulted in a very small error. Nevertheless, neglecting the series resistance, field dependence and gate voltage dependence of the mobility, it is assumed that the extracted mobility values are moot.

The second column of table 6.1 lists the results obtained from the conductance in the linear regime. Again, neither the field dependence nor the gate voltage dependence of the mobility was taken into account. However, the values were corrected for the series resistance. This extraction technique is particularly interesting, because it yields additional information like the resistivity, the charge carrier density and the series resistance.

The third column of table 6.1 summarises the results extracted from a parabolic fit of the transfer characteristic in the saturation regime. The only

difference compared to the previously described approach was the selected regime (saturation vs. linear regime). Although the charge carrier concentration is higher in the saturation regime than in the linear regime, the mobility values were comparable to $\mu_{lin}^{g_d}$. The determined value of $4.1 \cdot 10^{-5} cm^2/Vs$ is in good agreement with values found in other works that use the same measurement technique (e.g. $3 \cdot 10^{-5} cm^2/Vs$ in [112]). This comparison substantiates the validity of the results.

OC_1C_{10}-PPV showed the highest mobility for both approaches, followed by PEO-PPV and diPEO-PPV, which had an equally large mobility within one standard deviation. Finally, (PEO-OC_9)-PPV yielded the lowest mobility.

Polymer	$\mu_{lin}^{g_m}$ **[10^{-6} cm^2/Vs]**	$\mu_{lin}^{g_d}$ **[10^{-5} cm^2/Vs]**	μ_{sat}^{trans} **[10^{-5} cm^2/Vs]**	α_{lin}^{trans} **[10^{-7} $cm^2/Vs/V^{\beta}$]**
OC_1C_{10}-PPV	*10.59 ± 0.04*	*7.6 ± 0.3*	*4.1 ± 0.3*	*11.8 ± 0.6*
PEO-PPV	*1.71 ± 0.02*	*1.3 ± 0.1*	*1.6 ± 0.3*	*0.41 ± 0.01*
(PEO-OC_9)-PP	*4.84 ± 0.01*	*1.0 ± 0.2*	*0.8 ± 0.1*	*0.100 ± 0.003*
diPEO-PPV	*0.49 ± 0.02*	*1.1 ± 0.2*	*1.3 ± 0.1*	*2.5 ± 0.2*

Table 6.1:
Comparison of mobility values extracted from different FET measurements. The subscript indicates the extraction regime (lin = linear and sat = saturation). The superscript refers to the extraction method (g_m = transconductance, g_d = conductance and "trans" = transfer characteristic).

The fourth column of table 6.1 shows the mobility parameter α of the gate voltage-dependent mobility as determined from the linear regime of the output characteristics. The value is not directly comparable with the mobility, however it nearly conserves the previously mentioned "ranking", with OC_1C_{10}-PP yielding the highest value and (PEO-OC_9)-PPV the lowest. Only the positions of PEO-PPV and diPEO-PPV were interchanged.

6.1.2. Comparison of Series Resistance and Sheet Resistance

All prepared samples exhibited a rather large series resistance R_S. As mentioned in the previous section, it was crucial to correct the mobility values for R_S. Table 6.2 lists the ratio between R_S and the sheet resistance of the channel. The first two columns of table 6.2 show the results obtained from the conductance (section 2.3.2). The results from the fit (first column) reasonably agree with the results calculated from the resistivity, the film thickness and the series resistance. Note, that the errors of the calculated values are rather large, due to the big error of the values for the series resistance (see table 2.3).

Polymer	$r_{g_d}^{fit} = \frac{R_S}{R_{SHEET}}$ **[10^{-4}]**	$r_{g_d}^{calc} = \frac{R_S}{R_{SHEET}}$ **[10^{-4}]**	$r_{sat}^{fit} = \frac{R_S}{R_{SHEET}}$ **[10^{-4}]**
OC_1C_{10}-PPV	*3.4 ± 0.4*	*4 ± 1*	*5.2 ± 0.9*
PEO-PPV	*1.9 ± 0.7*	*1.6 ± 0.8*	*20 ± 6*
(PEO-OC_9)-PPV	*2 ± 1*	*0.6 ± 0.2*	*31 ± 7*
diPEO-PPV	*1.7 ± 0.9*	*4 ± 4*	*32 ± 4*

Table 6.2:
Comparison of the ratio r between the series resistance R_S and the sheet resistance R_{SHEET} of the channel. The subscript indicates the extraction method, either from the conductance g_d or the transfer characteristic in the saturation regime. The superscript specifies whether the value was obtained from a fit or from calculations.

The last column finally gives a comparison of the results extracted from the saturation regime. As mentioned in the previous section the mobility values stayed unchanged between the linear and the saturation regime. Conversely the ratio of R_S and R_{SHEET} increased by one order of magnitude for all PEOs. R_{SHEET} is expected to change, because the channel is partially depleted in the saturation regime. At the same time, the series resistance is changing too. Due to the increased charge carrier concentration in the saturation regime, the

contact resistance, i.e. R_S is expected to decreases. Both effects combined, leads to the observed change of the ratio r.

6.2. Comparison of Different Measurement Techniques

In the previous section, only the mobility values determined from FET measurements were compared. In this section, the results obtained from different measurement techniques are evaluated.

6.2.1. Comparison of Mobility Values

For the comparison of the different measurement techniques, one representative extraction method was chosen for each measurement technique. For the FET measurements, the results obtained from the conductance were taken (see section 2.3.2). Alternatively, the results extracted from the saturation regime could have been taken, since the mobility values were comparable. Only the mobility values calculated from the transconductance are not suitable, because as already pointed out they are less reliable. For the impedance spectroscopy values, the first-principle approach was used (see section 4.3), which circumvents the use of an

Polymer	**μ_{SCLC} [10^{-6} cm^2/Vs]**	**μ_{IMP} [10^{-6} cm^2/Vs]**	**μ_{FET} [$10^{-5}cm^2/Vs$]**
OC_1C_{10}-PPV	*7 ± 1*	*2.6 ± 0.3*	*7.6 ± 0.3*
PEO-PPV	*0.31 ± 0.06*	*5.1 ± 0.8*	*1.3 ± 0.1*
(PEO-OC_9)-PPV	*4.6 ± 0.4*	*1.1 ± 0.1*	*1.0 ± 0.2*
diPEO-PPV	*0.83 ± 0.05*	*1.3 ± 0.1*	*1.1 ± 0.2*

Table 6.3:
Comparison of the mobility values obtained from SCLC measurements (first column), impedance spectroscopy (second column) and FET measurements (last column).

"empiric" correction factor.

Table 6.3 lists these results together with the results of the SCLC measurements. Comparing the SCLC result of OC_1C_{10}-PPV with the literature value of $0.5 \cdot 10^{-6} cm^2/Vs$ [121], a large difference of one order of magnitude is noticed. This difference is attributed to the voltage drop at the series resistance of the device. In [121] this voltage drop is neglected, while it was taken into account in the present work. A comparison with the results of diPEO-PPV in table 3.1 shows that neglecting this voltage drop can lead indeed to a mobility value that is one order of magnitude smaller.

Except for PEO-PPV, the mobility values extracted from SCLC measurements and impedance spectroscopy were of the same order of magnitude. Note, that both measurements were performed on the same sandwich structures. However, the observed variation of the mobility of PPVs with different side chains was not the same. So far, OC_1C_{10}-PPV showed always the highest mobility. However, for the impedance results PEO-PPV exhibited the highest mobility. To explain the difference, it is noted that only the impedance results explicitly consider the effect of dispersive charge transport, as described by the parameters M and α. Especially α showed to be bigger for PEO-PPV than for the other PPVs (see table 4.2). Further, the material exhibited a larger field dependence than the remaining polymers. Hence, measurement techniques, which do not take both effects into account, might underestimate the mobility value of PEO-PPV relative to the other three PPVs studied. Finally, the last column of table 6.3 lists the FET results. The mobility showed to be one order of magnitude higher than for the two previous measurement techniques. This is attributed to the fact, that the field dependence of the mobility was neglected. Consequently, the listed values do not represent the zero-field mobility and therefore overestimate the mobility.

6.3. Dependence of Mobility from Material Parameters

Several material parameters are expected to influence the mobility. A very polar material for instance, can lead to a local alignment of polymer chains through dipole-dipole interactions, resulting in a higher mobility [109, 129,

130]. Further, it was demonstrated, that the mobility can depend on the molecular weight of the polymer [131]. Finally, in reference [132] it was concluded that the geometry of the molecular structure also influences the mobility. In this section, some of these influences are discussed in more detail.

6.3.1. Ordering of Polymers

As pointed out earlier, polymers can interact through their dipole moment. The degree of interaction is directly linked to the polarity of the molecule. Though the dipole-dipole interaction is a weak force, the polymer chains can align locally. This local ordering can lead to an increased mobility value [109, 129, 130].

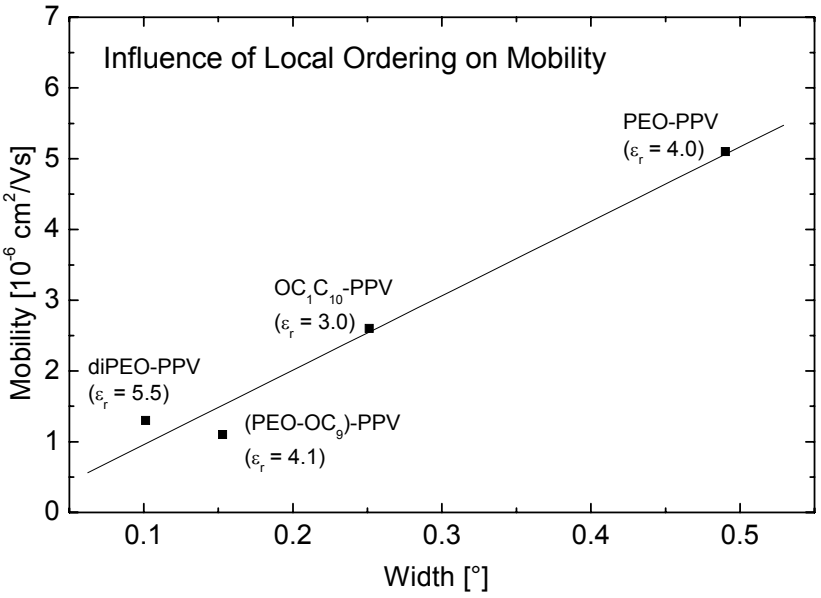

Figure 6.1:
Plot of the mobility against the width of the first order refraction peak of a XRD measurement at 150°C.

In section 5.2, XRD measurements were performed to assess the degree of ordering. The width of the refraction peak was used as a measure for the size of the ordered domains. Therefore, in figure 6.1 the mobility was plotted against the width. The width values were taken for a temperature of 150°C, because at room temperature the peak was either not present (OC_1C_{10}-PPV and PEO-PPV) or not well-defined ((PEO-OC_9)-PPV and diPEO-PPV). For the mobility, the results of the first-principle impedance spectroscopy approach were taken. The observed trend is opposite to the expected one. The smaller the width, the larger the ordered domains, hence the bigger the mobility. However, the largest mobility values were observed for the least ordered material (PEO-PPV). The labels of the depicted mobility values in figure 6.1 show also the relative permittivity of the polymers. As already explained in section 5.2, an influence of the polarity on the ordering was not observed.

In order to verify, whether this behaviour is caused by another overlapping trend, e.g. the polymer chain length, or whether it is a genuine effect of the ordering, it is proposed to perform measurements on polymer batches with equal molecular properties like chain length, poly dispersity, etc.

6.3.2. Influence of Molecular Structure on Mobility

Reference [132] states that the substitution pattern (symmetrical vs. asymmetrical) and the nature of the side chains (linear vs. branched) of PPVs has an influence on the charge carrier mobility. It is further argued that the increased regularity of PPVs with two identical side chains can increase the mobility by a factor of ten. In addition replacing branched side chain by linear side chains further improves the mobility.

Following the explanation of the paragraph above, diPEO-PPV should exhibit the largest mobility, while OC_1C_{10}-PPV should yield the lowest value, because of its asymmetrical and branched $OC_{10}H_{21}$ side chain. However, in all measurements except for the first-principle impedance spectroscopy, OC_1C_{10}-PPV showed the highest mobility, i.e. the effect of the molecular structure suggested by [132] could not be observed. However, the dramatic increase of mobility values in [132] was mainly observed after annealing the samples beyond the glass transition temperature. As shown in section 2.5.3, annealing the polymers had a detrimental effect on the mobility of the PPVs

studied in this work. Only the mobility value of (PEO-OC_9)-PPV remained the same after annealing (see table 2.7). Thus, the effect could not be confirmed. The results of this study indicate that other factors, than the molecular structure, have a larger influence for as-prepared samples.

6.4. Bias Stress Effect

In section 2.5.1 it was demonstrated, that applying a voltage can have a huge influence on the FET characteristics of polymers. This applies of course not only to FET measurements, but also to any kind of electrical characterisation technique, where a voltage is applied continuously. Therefore, the exact measurement procedure, i.e. the delay between subsequent measurements, the integration time, etc., influences the extracted mobility value. Hence, if bias stress is the determining factor, pulsed measurements are suggested to circumvent these measurement artefacts [27].

In contrast to OC_1C_{10}-PPV, the PEOs studied in this work exhibited a rather small bias stress effect. Since the bias stress effect is attributed to the trapping of charges, this result indicates that either the trap concentration of the PEOs is lower than for OC_1C_{10}-PPV or the release rate of the charges is much higher, leading to a continuous recovery even in darkness. In section 2.4 it was demonstrated for all four PPVs that the mobility is gate voltage-dependent. This was explained by a rather high trap concentration. Hence, the small bias stress effect of the PEOs must be caused by a rather quick release of trapped charges. This would also explain why only OC_1C_{10}-PPV exhibited a strong light dependence. For the PEOs light-assisted release of trapped charges would be negligible, since the release rate is already rather high in darkness.

6.5. Conclusion

The variety of extracted mobility values for each of the four studied PPVs shows, that the choice of measurement technique and extraction procedure is crucial for the absolute mobility value extracted. While SCLC measurements and impedance spectroscopy yield similar results, the FET mobility is one order of magnitude higher. Therefore, when dealing with devices like solar cells and

OLEDs, it is proposed to use SCLC and impedance spectroscopy as techniques to determine the mobility. SCLC measurement is a straightforward and thus easy to apply measurement technique. Though the first-principle approach applied on the impedance spectroscopy data is more elaborate and it yields additional information on the charge carrier transport, such as the degree of dispersion. Since both types of measurement can be performed on the same samples, they can complement one another.

Relating material properties to the extracted mobility values has shown to be very difficult since there are many different factors that can influence the mobility, e.g. the polarity, the molecular weight, the molecular structure, etc. Thus, when comparing the mobility of different sources, the values must be interpreted carefully.

7. Morphological Study of PPV:C_{60} Blends

In the previous chapters, the electrical and optical properties of pure polymer films were characterised. In this chapter the morphology of polymer films blended with a fullerene derivative are studied. Such blends exhibit a complex morphology, which is influenced by a number of different parameters. Some of these parameters like the polarity of the constituent molecules, the polarity and the boiling point of the solvent and the influence of additives are studied in the following sections.

While characterising pure polymer films is sufficient when developing organic LEDs or transistors, devices such as bulk heterojunction solar cells, the realisation of which is the aim of the present work, require a material blend of an electron donor and an electron acceptor. For a detailed discussion of the layout and working principle of bulk heterojunction solar cells see section 8.1.3. The solar cells prepared and characterised in chapter 8 consist of several layers. The photovoltaic active film consists of a blend of one of the PPVs studied so far (electron donor) and a fullerene derivative (electron acceptor).

7.1. Preparation Details

The samples were usually prepared on glass substrates covered with indium tin oxide. The glass substrates underwent the cleaning process described in section 2.2. However, except for the few samples, which were later used as solar cells, the UV/ozone treatment was not necessary and thus skipped. Depending of the surface tension, 100µl to 300µl of the solution was evenly spread on the substrate before starting the spin coating programme. Since the thickness of the films was not important, the same set of spin coating parameters were used for all samples (see table 7.1), resulting in thicknesses ranging from ~50nm to ~350nm. Finally, the samples were stored for several hours in vacuum to ensure complete evaporation of the solvent. The morphology of the samples was then studied by means of atomic force microscopy (AFM). The subsequent AFM images of figure 7.2 to figure 7.13 all show a 4µm × 4µm area (columns on left hand side) to assess the uniformity

of the film. The 1µm × 1µm images (columns on right hand side) are a magnification of the centre of the larger areas, to study nanoscale features as they appear upon phase separation. For the measurements, two different AFM systems were used. The images depicted in figure 7.2 to figure 7.4, figure 7.6 to figure 7.9 and figure 7.13 were acquired with Veeco's multimode microscope equipped with a Nanoscope III controller. The remaining images were recorded with a Park CP Autoprobe AFM. For all measurements, an etched silicon cantilever-tip was used, with an estimated tip radius of 5nm to 10nm. The tips for the Veeco system were purchased from Nanosensors GmbH (PPP-NCHR) and the tips for the Park device from MicroMash (Ultrasharp NCS11-B).

	Step 1	**Step 2**	**Step 3**
Lid	*open*	*closed*	*open*
Speed [rpm]	*500*	*1500*	*500*
Acceleration [rpm/s]	*500*	*1000*	*500*
Time [s]	*4*	*4*	*180*

Table 7.1:
Standard set of spin coating parameters for sample preparation.

7.2. Effect of Polymer

In section 5.1 it was shown, that the four studied PPVs differ quite a lot in polarity. OC_1C_{10}-PPV with a relative permittivity of ~3 was the least polar material and diPEO-PPV with a relative permittivity of ~5.5 the most polar one. It is expected, that the differing polarity of the PPVs has a large influence on the morphology of blended films. The samples compared in this section were prepared from chlorobenzene solutions of mixtures of one of the studied PPVs with the fullerene derivative [6,6]-phenyl C_{61}-butyric acid methyl ester PCBM (see figure 7.1), purchased from Solenne B. V.

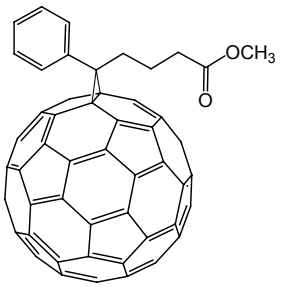

HOMO = -5.53eV

LUMO = -3.96eV

Figure 7.1:
Chemical structure of [6,6]-phenyl C_{61}-butyric acid methyl ester PCBM (left and side) and electrochemically determined HOMO and LUMO levels (right hand side).

Figure 7.2 to figure 7.5 show AFM images of different blend ratios ranging from 1:1 to 1:4. The OC_1C_{10}-PPV:PCBM samples (figure 7.2) show the typical morphology with no phase separation at low PCBM concentrations and a nicely phase separated film, as required for solar cells, at a ratio of 1:4 (for an explanation what qualifies as a good morphology see chapter 8). The bright regions correspond to PCBM-rich clusters, which appear upon phase separation [133]. As expected, the root mean square surface roughness of 1.3nm is slightly higher for the phase-separated morphology than for the non-phase-separated films. The indicated surface roughness depends of course on the position where the images were acquired. However, for smooth films the obtained values should vary only insignificantly over the surface of a sample. For the PEOs, phase separation starts already at lower PCBM concentrations. This is a direct result of the increased polarity of the polymers. PEO-PPV (figure 7.3) exhibits at a ratio of 1:1 the most suitable morphology for solar cells. The surface roughness of ~1nm is comparable to the OC_1C_{10}-PPV:PCBM sample. For higher PCBM concentration bigger clusters are formed, increasing the surface roughness up to ~7nm. For (PEO-OC_9)-PPV (figure 7.4) and diPEO-PPV (figure 7.5) even the 1:1 blend shows already rather large clusters. Consequently, the surface roughness exceeds 10nm and even reaches up to ~50nm for the 1:1 diPEO-PPV:PCBM sample. Due to overlapping of the PCBM clusters (see figure 7.5), the surface roughness of the diPEO-PPV samples decreases with increasing PCBM concentration. This is opposite to the trend observed for the other PPVs.

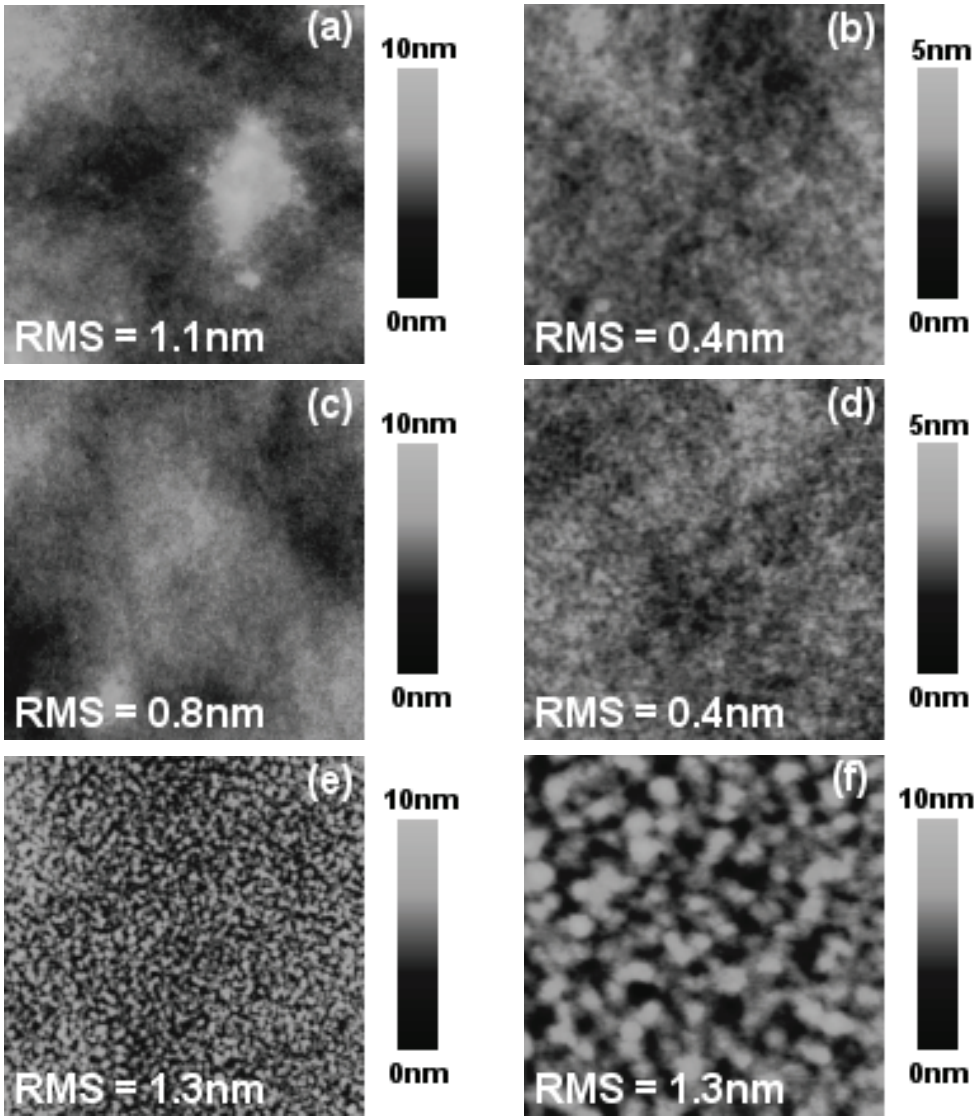

Figure 7.2:

AFM images of OC_1C_{10}-PPV:PCBM films with ratios of 1:1 (a and b), 1:2 (c and d) and 1:4 (e and f). The images in the left column show an area of 4µm × 4µm; the images in the right column show an area of 1µm × 1µm. The indicated values denote the root mean square surface roughness RMS.

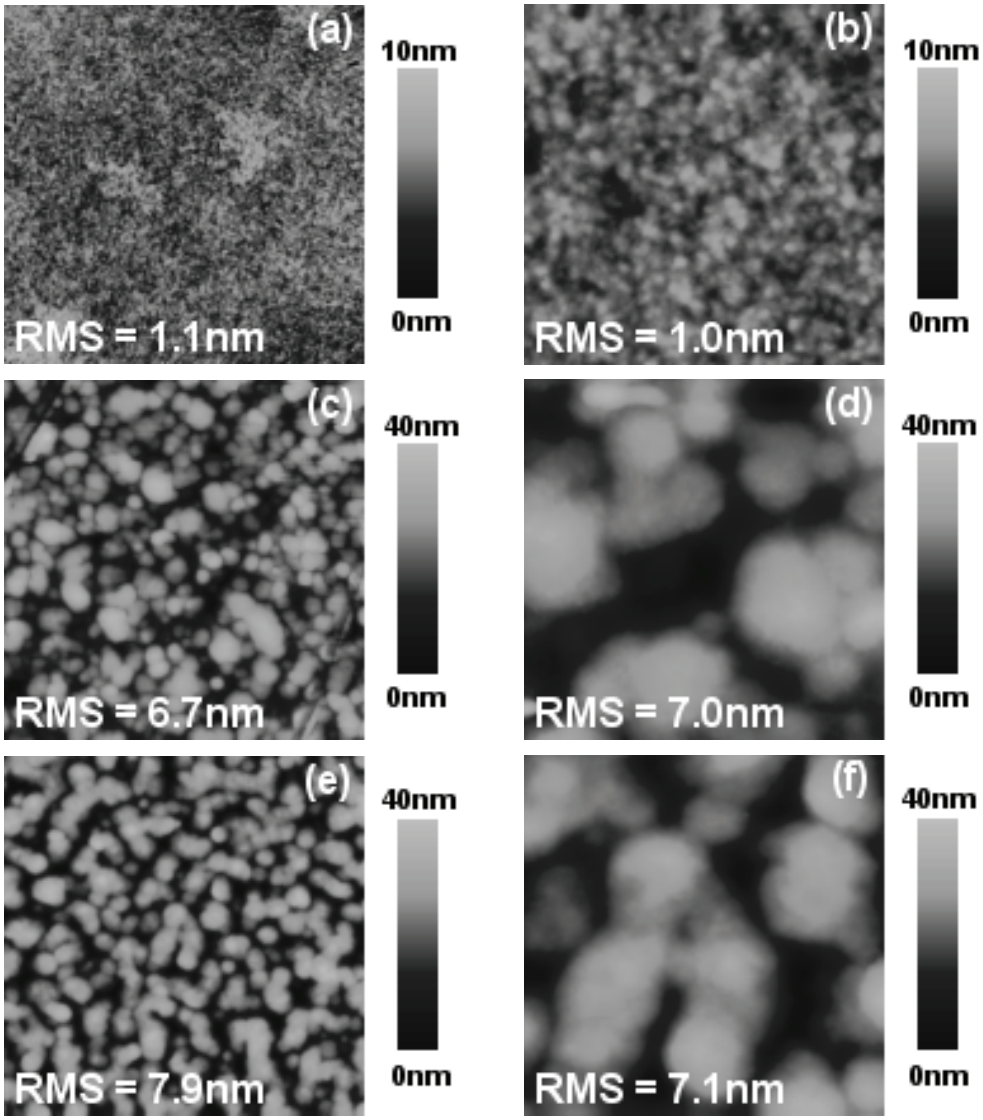

Figure 7.3:

AFM images of PEO-PPV:PCBM films with ratios of 1:1 (a and b), 3:7 (c and d) and 1:4 (e and f). The images in the left column show an area of 4μm × 4μm; the images in the right column show an area of 1μm × 1μm. The indicated values denote the root mean square surface roughness RMS.

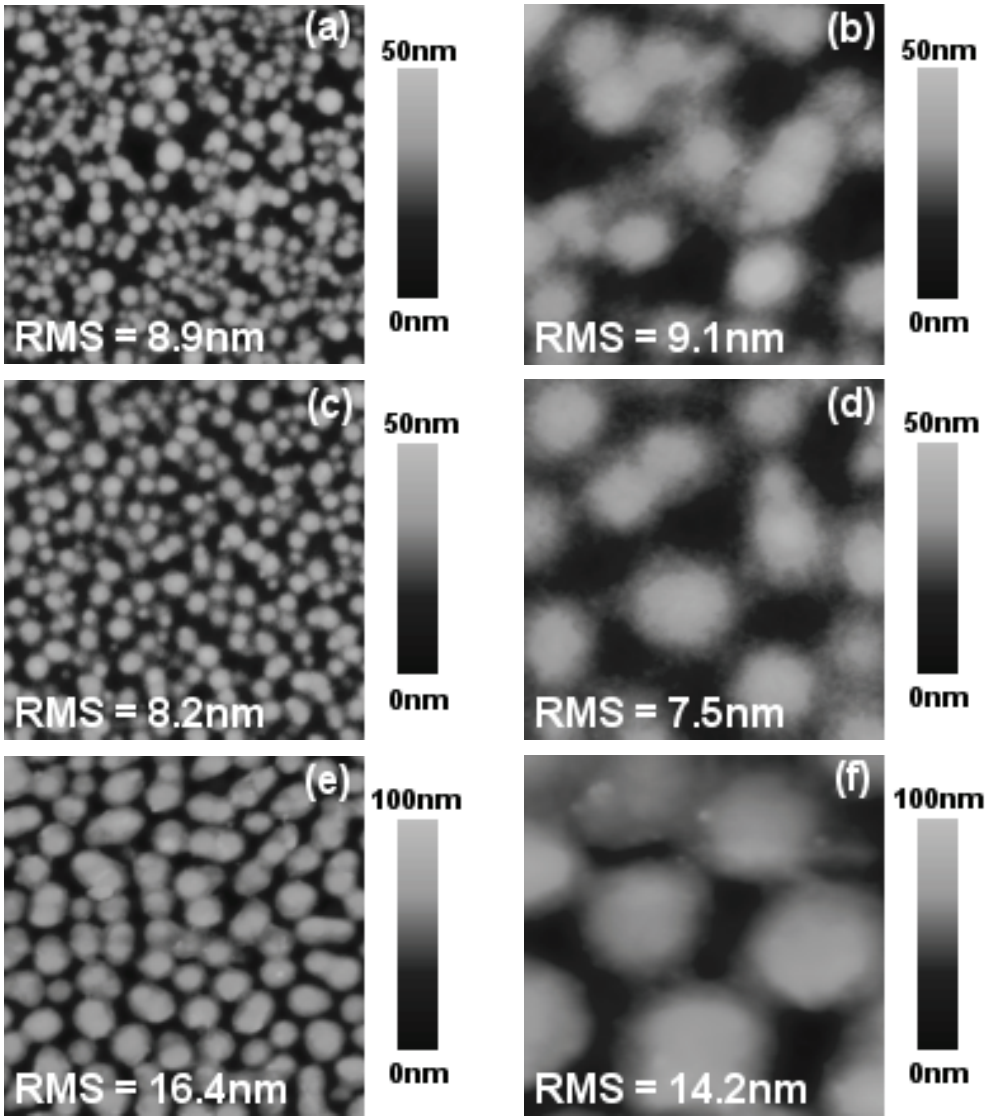

Figure 7.4:

AFM images of (PEO-OC_9)-PPV:PCBM films with ratios of 1:1 (a and b), 1:2 (c and d) and 1:4 (e and f). The images in the left column show an area of 4µm × 4µm; the images in the right column show an area of 1µm × 1µm. The indicated values denote the root mean square surface roughness RMS.

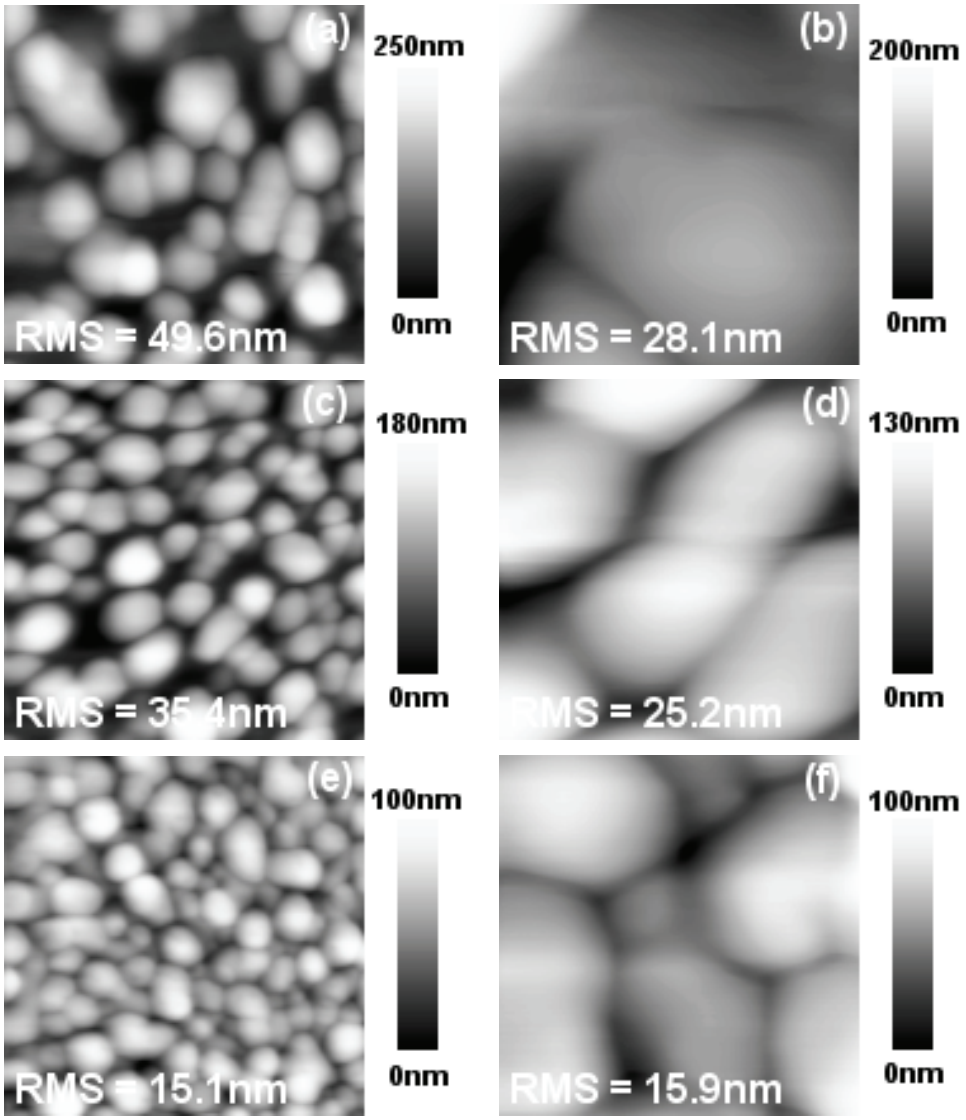

Figure 7.5:

AFM images of diPEO-PPV:PCBM films with ratios of 1:1 (a and b), 1:2 (c and d) and 1:4 (e and f). The images in the left column show an area of 4µm × 4µm; the images in the right column show an area of 1µm × 1µm. The indicated values denote the root mean square surface roughness RMS.

Polymer	ε_r	RMS Surface Roughness [nm]			Phase Separation
		1:1	1:2	1:4	
OC_1C_{10}-PPV	*3.01*	*1.1*	*0.8*	*1.3*	*none*
PEO-PPV	*4.0*	*1.1*	*6.7*	*7.9*	*starting*
(PEO-OC_9)-PPV	*4.1*	*8.9*	*8.2*	*16.4*	*present*
diPEO-PPV	*5.5*	*49.6*	*35.4*	*15.1*	*present*

Table 7.2:

Comparison of relative permittivity ε_r of the four PPVs and the root mean square (RMS) surface roughness of their blends with PCBM. The rightmost column indicates the degree of phase separation at a blend ratio of 1:1.

The comparison of PEO-PPV and (PEO-OC_9)-PPV shows that derivatives with almost equal polarity (ε_r = 4.0 vs. ε_r = 4.1) can exhibit different behaviour (see table 7.2). This can be explained by the different length of the polymer chains, i.e. the number of repeating units. Where PEO-PPV consists of polymer chains with an average of ~550 units, (PEO-OC_9)-PPV is much shorter with only ~50 units (see table 1.1). It is suggested that the chain length influences the diffusion of PCBM and thus the formation of clusters upon phase separation.

7.3. Effect of Solvent

In this section, a closer look is taken on the influence of the solvent on the morphology. Solutions of OC_1C_{10}-PPV and PCBM with ratios of 1:1, 1:2 and 1:4 were prepared for five different solvents. The solvents differed in boiling point and polarity (see table 7.3). The boiling point is taken as a measure for the rate of evaporation during spin coating. For instance, chloroform with a boiling point of only 61°C evaporates much quicker than chlorobenzene with a boiling point of 181°C. The figures below show the morphology of films prepared from five different solvents, chlorobenzene (figure 7.2), chloroform (figure 7.6), toluene (figure 7.7), m-dichlorobenzene (figure 7.8) and o-dichloro-benzene (figure 7.9). The chloroform samples show phase separation for all three ratios. At a ratio of 1:2, the degree of phase separation is comparable to

the 1:4 sample prepared from chlorobenzene. The surface roughness of these samples is also comparable (1.6nm vs. 1.3nm). Although the polarity of chloroform is slightly lower than for chlorobenzene, the main difference is the boiling point. With a boiling point of 61°C, chloroform evaporates much quicker than chlorobenzene. Thus the time for forming separated phases is limited, suggesting that phase separation occurs already in the solution. The merely changing morphology with increasing PCBM concentration confirms that the chloroform samples show just the "frozen" phase separation already present in the solution.

Solvent	**Boiling Point [°C]**	**Relative Permittivity**	**RMS Roughness [nm]**
chlorobenzene	*181*	*5.6*	*1.3*
chloroform	*61*	*4.8*	*2.4*
toluene	*110*	*2.4*	*6.6*
m-dichlorobenzene	*173*	*5.0*	*2.6*
o-dichlorobenzene	*180*	*9.9*	*0.9*

Table 7.3:
Material parameters of the used solvents (values were taken from [134]). The last column denotes the root mean square (RMS) surface roughness of a 1:4 blend of OC_1C_{10}-PPV and PCBM.

The toluene-based samples depicted in figure 7.7 exhibit a rather atypical behaviour. At a blend ratio of 1:1 no phase separation occurs. However, increasing the PCBM concentration to 2/3, suddenly a strong phase separation emerges, with big clusters separated from each other. Increasing the PCBM concentration further, the size of the clusters is reduced and the film becomes smoother. In contrast to all other solvents used, toluene has a much lower relative permittivity and dipole moment (see table 7.3). This probably influences the solubility as well as the phase separation process, leading to the distinct features observed.

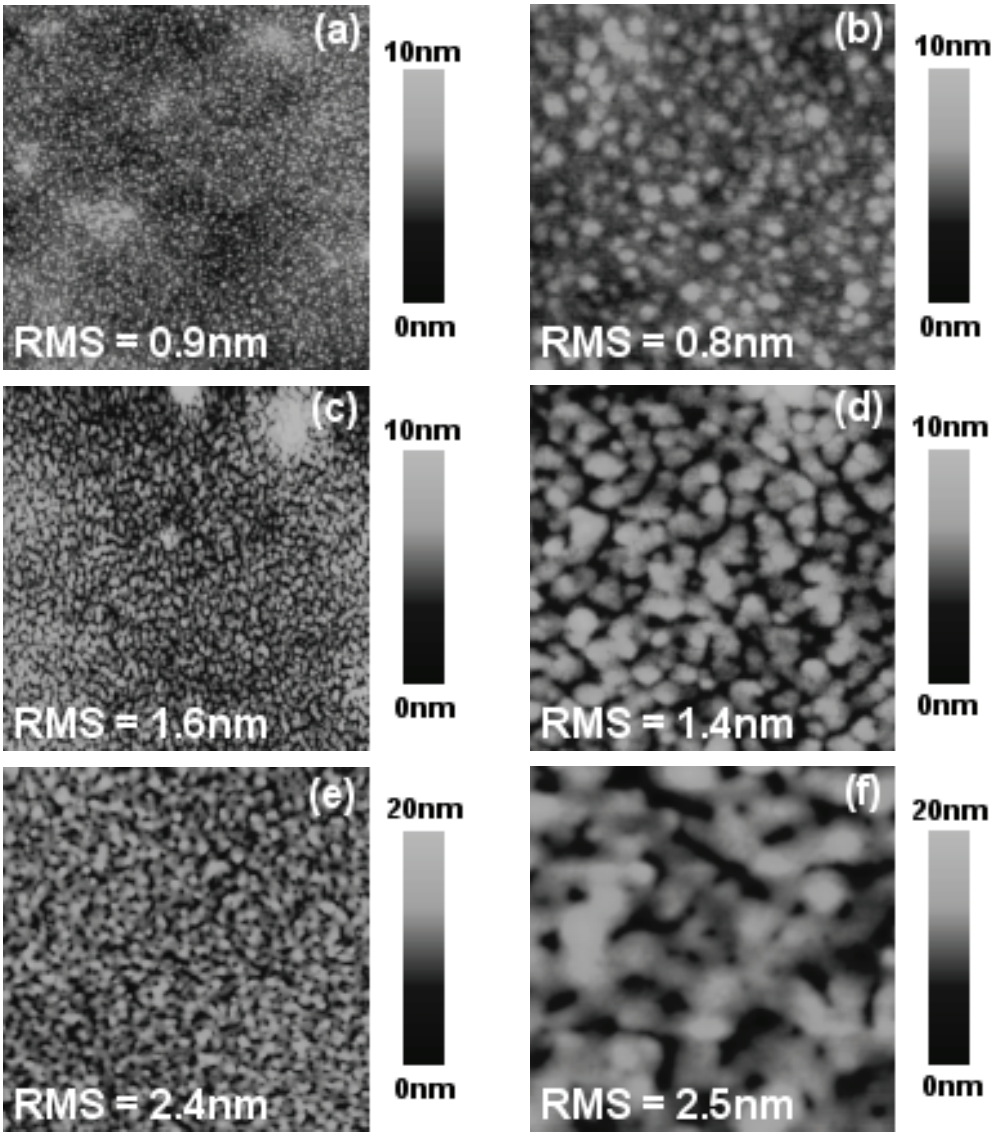

Figure 7.6:

AFM images of OC_1C_{10}-PPV:PCBM films with ratios of 1:1 (a and b), 1:2 (c and d) and 1:4 (e and f) spin coated from chloroform solutions. The images in the left column show an area of 4μm × 4μm; the images in the right column show an area of 1μm × 1μm. The indicated values denote the root mean square surface roughness RMS.

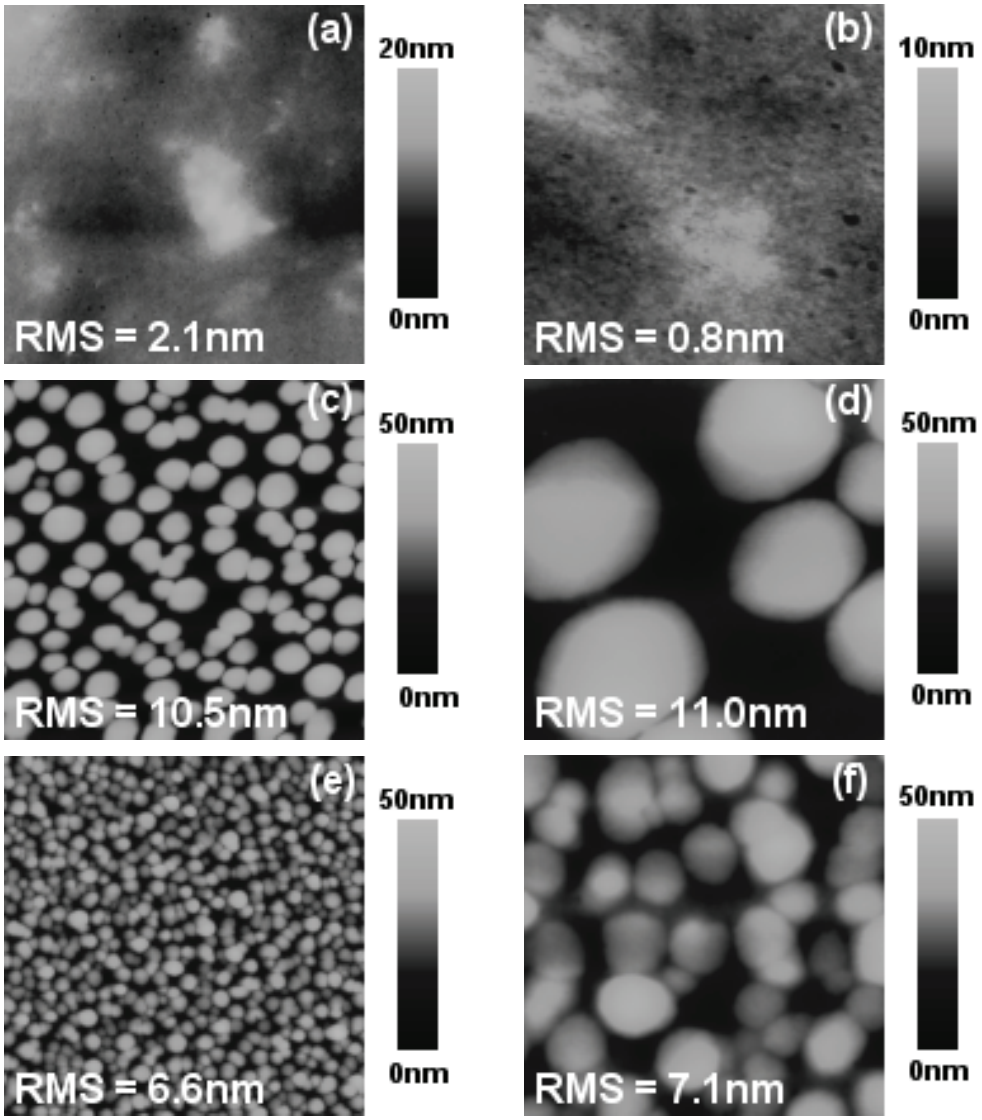

Figure 7.7:

AFM images of OC_1C_{10}-PPV:PCBM films with ratios of 1:1 (a and b), 1:2 (c and d) and 1:4 (e and f) spin coated from toluene solutions. The images in the left column show an area of 4μm × 4μm; the images in the right column show an area of 1μm × 1μm. The indicated values denote the root mean square surface roughness RMS.

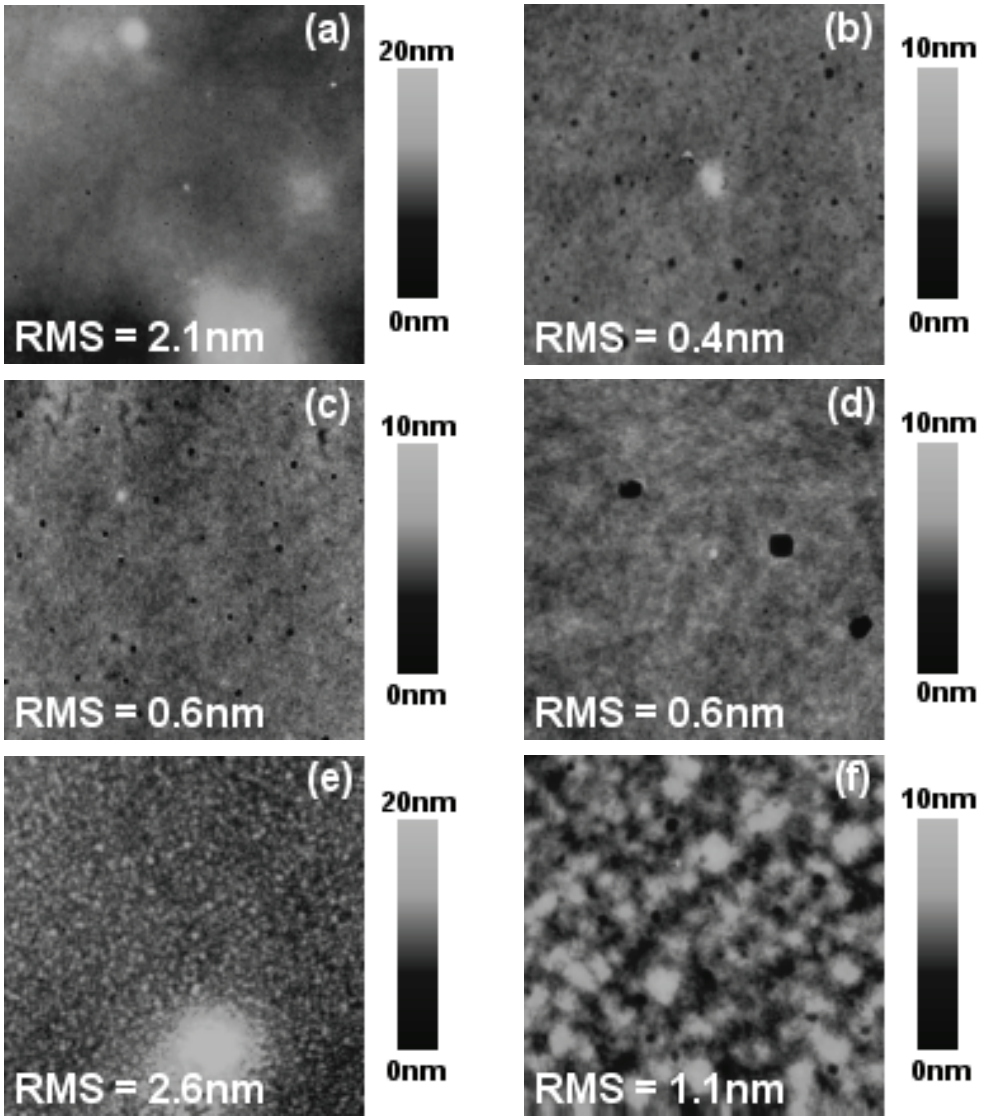

Figure 7.8:

AFM images of OC_1C_{10}-PPV:PCBM films with ratios of 1:1 (a and b), 1:2 (c and d) and 1:4 (e and f) spin coated from m-dichlorobenzene solutions. The images in the left column show an area of 4μm × 4μm; the images in the right column show an area of 1μm × 1μm. The indicated values denote the root mean square surface roughness RMS.

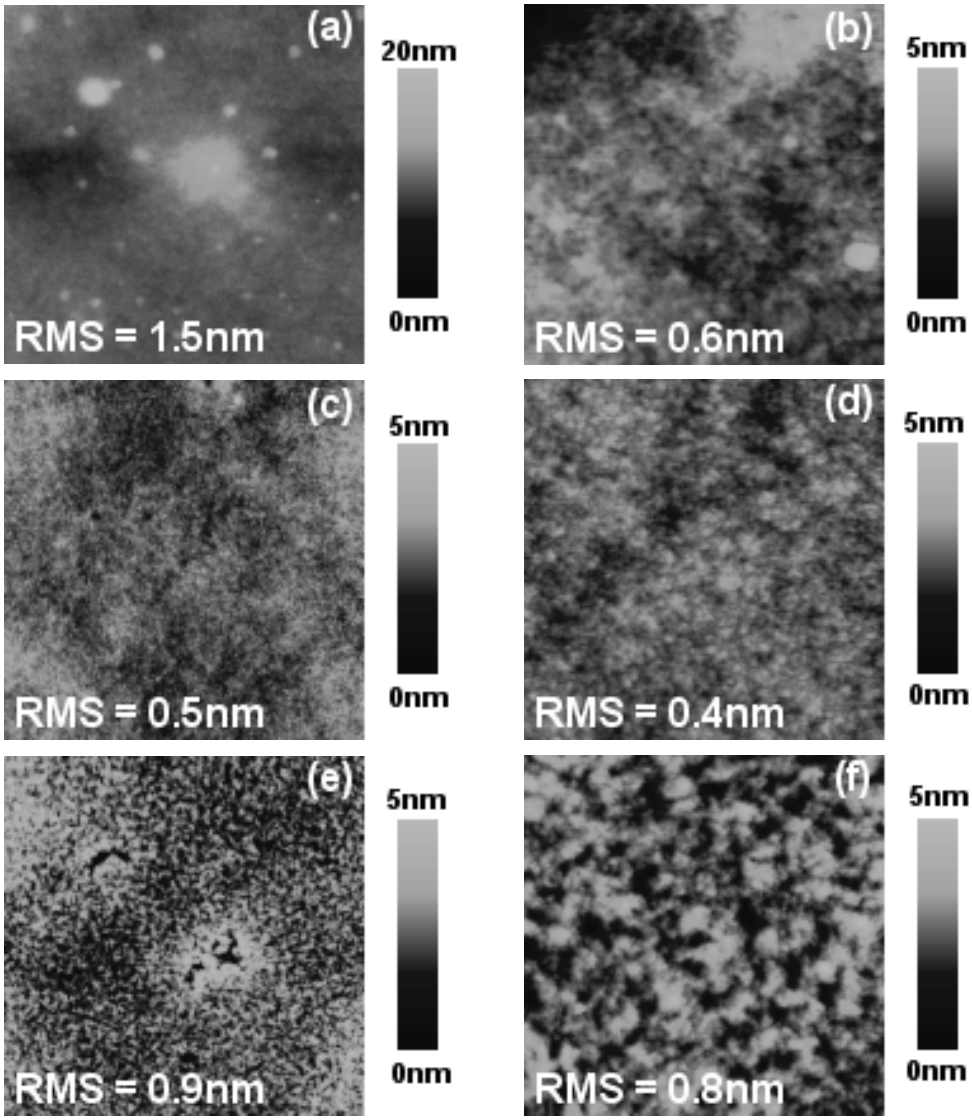

Figure 7.9:

AFM images of OC_1C_{10}-PPV:PCBM films with ratios of 1:1 (a and b), 1:2 (c and d) and 1:4 (e and f) spin coated from o-dichlorobenzene solutions. The images in the left column show an area of 4µm × 4µm; the images in the right column show an area of 1µm × 1µm. The indicated values denote the root mean square surface roughness RMS.

Finally, the dichlorobenzene samples (figure 7.8 and figure 7.9) exhibit a similar behaviour as the chlorobenzene samples. At low PCBM concentration no phase separation occurs. At higher PCBM concentrations, the phase separation is comparable to the chlorobenzene samples. Although the polarity of m-dichlorobenzene and o-dichlorobenzene differ significantly (see table 7.3), the morphology of the samples was very similar. It is therefore concluded, that other parameters of the solvent are more important for the morphology. For instance, chlorobenzene, m-dichlorobenzene and o-dichlorobenzene share a similar boiling point, which influences how quickly the solvent evaporates. Since the morphology of the samples based on these three solvents is quite similar, it is suggested that the evaporation of the solvent has a much larger impact on the film morphology than other parameters. Thus, it is concluded that a similar boiling point of the solvent leads to a similar morphology.

7.4. Effect of Fullerene Derivative

So far, the polarity of the PPVs and of the solvents was studied. In this section, PEO-PPV:C_{60} blends were prepared using fullerene derivatives with more polar side chains. The C_{60} derivatives depicted in figure 7.10 were provided by the University of Padova[6]. Note, that C_{60}-5 has three PEO side chains attached to the benzene ring and is therefore by far the most polar fullerene derivative used. The PEO-PPV:C_{60} blends were dissolved in chlorobenzene with ratios of 1:1, 1:2 and 1:4.

[6] Michele Maggini, Department of Chemical Science, University of Padova, Italy

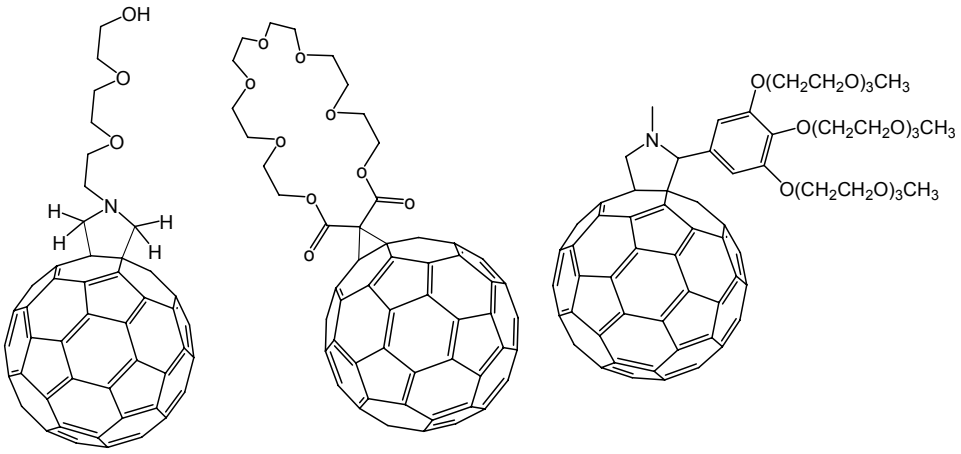

Figure 7.10:
Three fullerene derivatives with different side chains. In this work the molecules are referred to as C_{60}-2 (left hand side), C_{60}-4 (middle) and C_{60}-5 (right hand side).

Figure 7.11 shows the AFM images of the C_{60}-2 blends. Already at a blend ratio of 1:1 a strong phase separation occurs, leading to a film with a high surface roughness of ~50nm. Increasing the C_{60}-2 concentration results in the formation of big separated clusters. Unlike the toluene samples of the previous section, these clusters are not circular. The irregularly shaped clusters may indicate that they were already present in solution and represent chunks of undissolved material. Consequently the film between the clusters contains only few C_{60}-2, resulting in a very smooth surface with a surface roughness of 0.5nm (see marked area in figure 7.11 f).

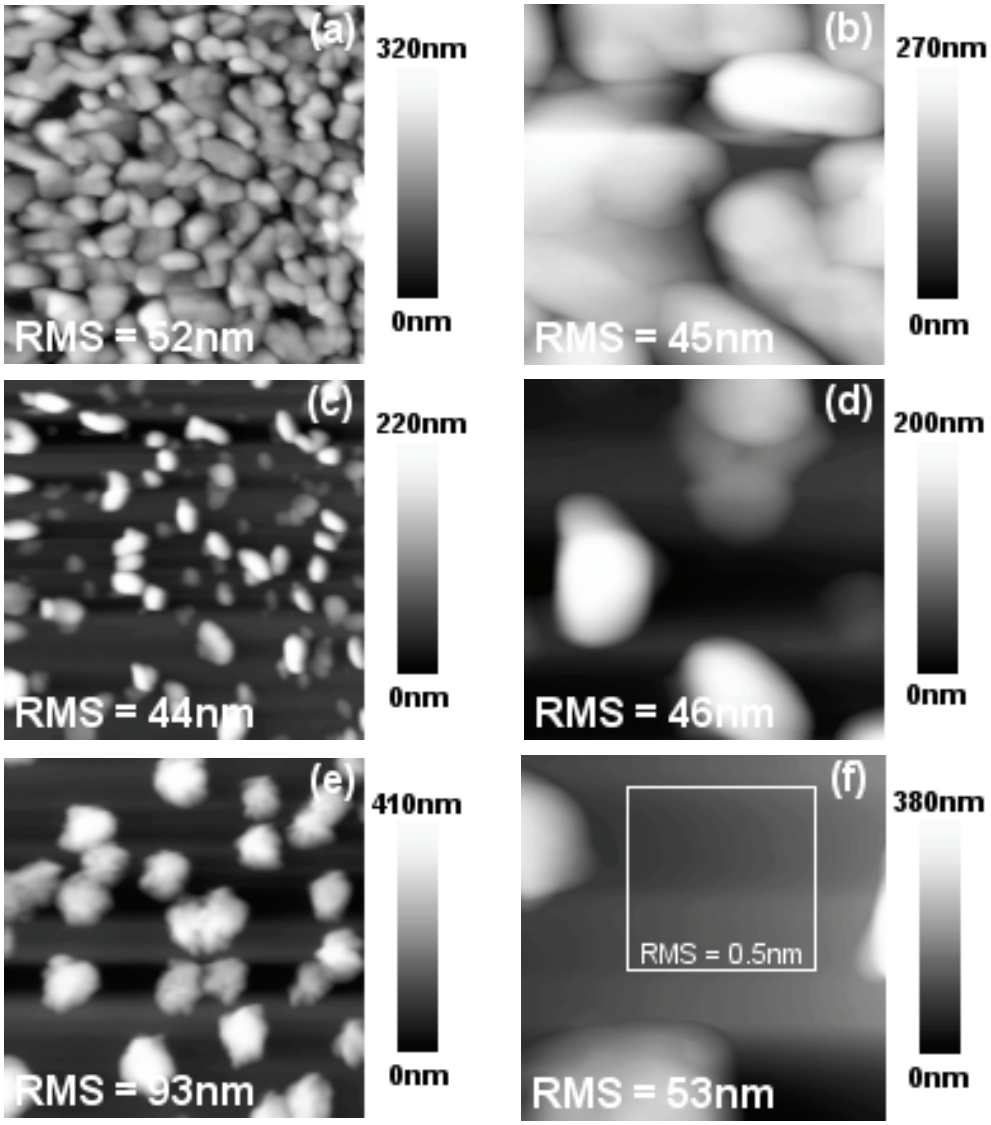

Figure 7.11:

AFM images of PEO-PPV:C_{60}-2 films with ratios of 1:1 (a and b), 1:2 (c and d) and 1:4 (e and f). The images in the left column show an area of 4μm × 4μm; the images in the right column show an area of 1μm × 1μm. The indicated values denote the root mean square surface roughness RMS.

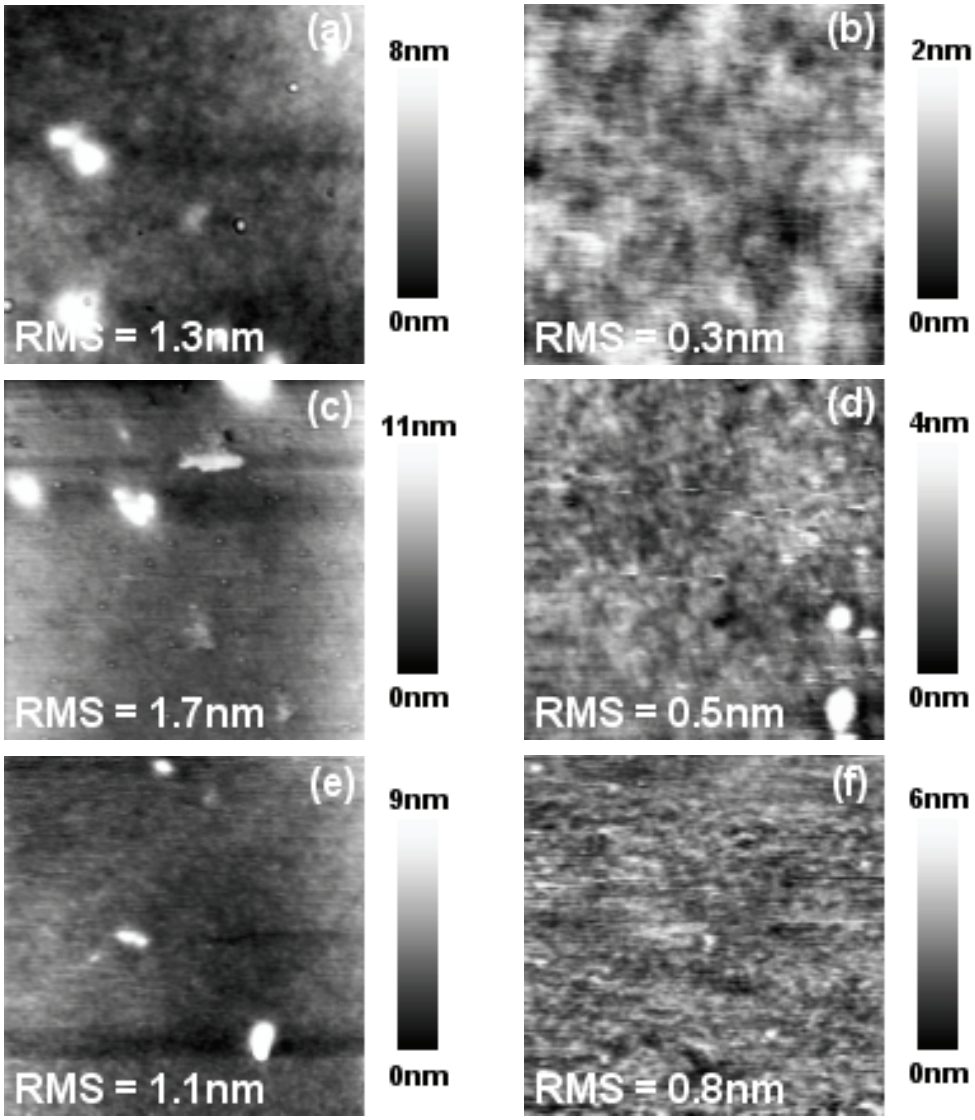

Figure 7.12:

AFM images of PEO-PPV:C_{60}-4 films with ratios of 1:1 (a and b), 1:2 (c and d) and 1:4 (e and f). The images in the left column show an area of 4μm × 4μm; the images in the right column show an area of 1μm × 1μm. The indicated values denote the root mean square surface roughness RMS.

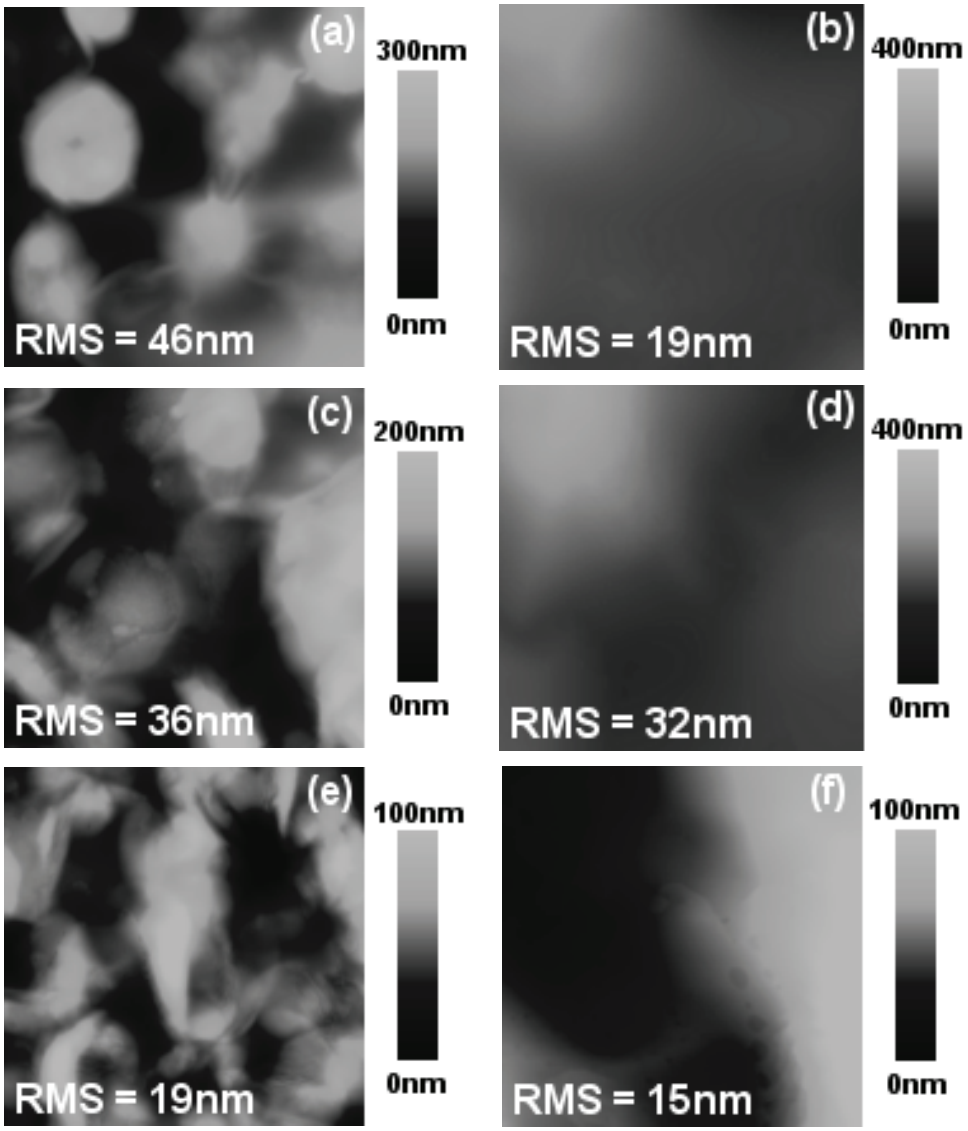

Figure 7.13:

AFM images of PEO-PPV:C_{60}-5 films with ratios of 1:1 (a and b), 1:2 (c and d) and 1:4 (e and f). The images in the left column show an area of 4μm × 4μm; the images in the right column show an area of 1μm × 1μm. The indicated values denote the root mean square surface roughness RMS.

C_{60}	Phase Separation	RMS Roughness [nm]		
		1:1	1:2	1:4
PCBM	*starts at 1:1*	*1.1*	*6.7*	*7.9*
C_{60}-2	*strong at 1:1*	*52*	*44*	*93*
C_{60}-4	*none for all ratios*	*1.3*	*1.7*	*1.1*
C_{60}-5	*no genuine structure for all ratios*	*46*	*36*	*19*

Table 7.4:
Comparison of phase separation and root mean square (RMS) roughness of four different PEO-PPV:C_{60} blends.

C_{60}-4 and C_{60}-5 show a better solubility in chlorobenzene, yielding films with fewer chunks. The PEO-PPV:C_{60}-4 blends (figure 7.12) exhibited no phase separation at the studied scale. The surface is rather smooth (surface roughness greater than 1nm) and comparable to the OC_1C_{10}-PPV:PCBM samples in figure 7.2 before phase separation starts. It is assumed that not even at higher C_{60}-4 concentrations, phase separation would occur. The C_{60}-5 samples showed no genuine structure whatsoever. However, on large scale (4µm × 4µm images in the left hand column of figure 7.13) the surface roughness seems to decrease with higher C_{60}-5 concentrations. Nevertheless, it is doubtful whether at C_{60}-5 concentrations beyond 80% phase separation would start.

7.5. Effect of Surfactant

Finally, another possibility of influencing the film morphology is briefly discussed. A 1:1 blend of PEO-PPV and C_{60}-4 was dissolve in chlorobenzene. Then two samples were prepared, one from the pristine solution, the other after adding 1% vol. of a surfactant. The surfactant (pentaethylene glycol monododecyl ether) was purchased from Sigma-Aldrich. The chemical structure is depicted in figure 7.14. Even at the rather low concentration of 1% vol., the surfactant has a large impact, which is expected to increase during evaporation of the solvent.

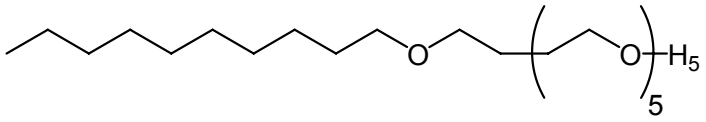

Figure 7.14:
Chemical structure of pentaethylene glycol monododecyl ether, used as a non-ionic surfactant in the prepared solution.

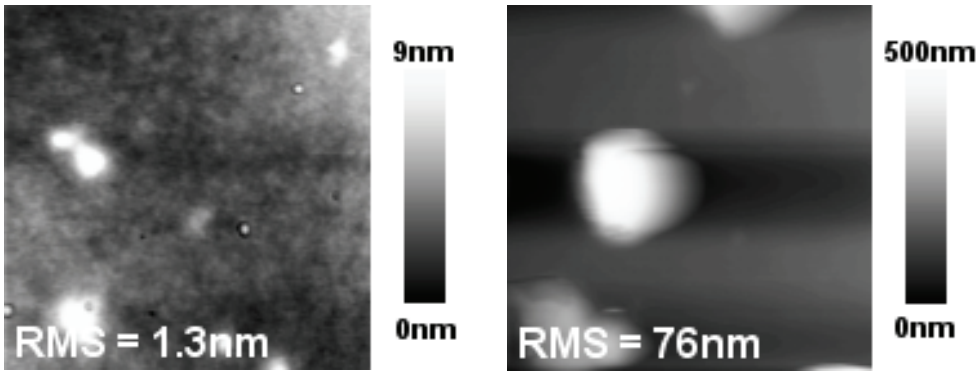

Figure 7.15:
Comparison of a PEO-PPV:C_{60}-4 1:1 blend without (left hand side) and with 1% vol. of the non-ionic surfactant pentaethylene glycol monododecyl ether (right hand side). The images show an area of 4µm × 4µm. The indicated values denote the root mean square surface roughness RMS.

Figure 7.15 shows the pristine film (left hand side) and the film prepared from the solution with surfactant (right hand side). Adding the surfactant leads to large clusters, increasing the surface roughness dramatically. Figure 7.15 proofs that adding a surfactant is an alternative way to influence the morphology of blends. However, a deeper understanding is necessary to pick a suitable surfactant. Furthermore, the effect of the surfactant becomes predominant when the solvent evaporates and the relative concentration of the surfactant becomes comparable to the dissolved specimen.

7.6. Conclusion

Several parameters that influence the morphology of PPV:C_{60} blends were studied in this chapter. With the regard to the development of bulk heterojunction solar cells, it is crucial to obtain films with a suitable phase separation. Further, the surface roughness should not exceed a few nanometres. These requirements render the samples prepared from alternative fullerene derivatives inadequate for solar cells. Hence, the following chapter resorts to the well-known fullerene derivative PCBM as an electron acceptor.

8. Solar Cell Characterisation

In this chapter an introduction to photovoltaics in general and to organic solar cells in specific is given. The working principle of the bulk heterojunction solar cells fabricated in this work is explained and a simple model to estimate solar cell parameters is discussed. Finally experimental results of solar cells prepared from PPV:PCBM blends are presented.

8.1. Introduction

8.1.1. General Introduction to Photovoltaics

Photovoltaics describes the process of converting solar radiation into electricity. Independently from the design of a particular solar cell, photovoltaics is based on the photo effect, which was first observed by Alexandre-Edmond Becquerel as early as 1839 [135]. However, it took until the beginning of the 20th century before it was theoretically explained by applying quantum mechanical principles[7] [136].

To understand the working principle of a solar cell better, the individual physical processes involved are briefly described. The first step of solar energy conversion is the absorption of the incident sunlight. The lower the band gap of the material, the more photons can be absorbed. However, lowering the band gap also lowers the output voltage. Hence, there is an optimal band gap, which depends on the spectrum. In figure 8.1 the standard spectrum AM1.5g (left hand side) and the maximum efficiency dependent on the band gap are depicted. The band gaps of silicon (Si) and gallium arsenide (GaAs), which are used in conventional solar cells, are indicated.

For a material with a given band gap, the absorption can be maximised by increasing the thickness of the absorber to reduce transmission losses and by applying an anti-reflection coating to minimise reflection. In principle, both optimisations can be applied to all solar cell concepts. Nonetheless, in the case

[7] Albert Einstein Nobel prize in physics 1921

of thin devices (layer thicknesses in the order of the coherence length of sunlight) interference effects must also be taken into account.

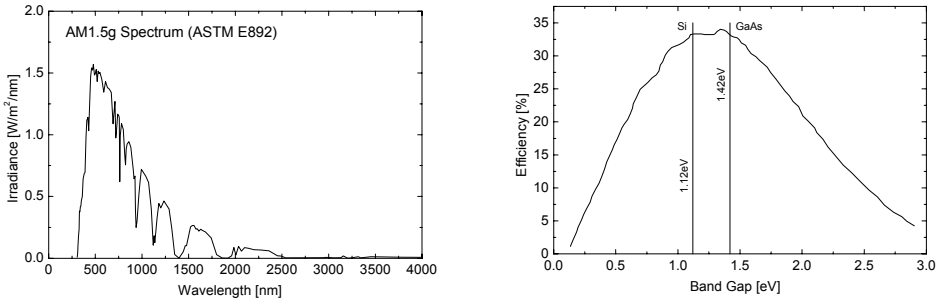

Figure 8.1:
Solar spectrum AM1.5g (left hand side) and maximum efficiency for a single junction device (right hand side). For both plots, the standard spectrum according to ASTM E892 was used.

In conventional solar cells, the absorbed sunlight excites an electron from the valence band to the conduction band of the material. The created electron-hole pair is thermally dissociated and the free charge carriers can diffuse in the solar cell. The charge carriers are driven towards opposite electrodes by the different gradients of the quasi-Fermi energies in the p-type and the n-type layer.

The I-V characteristic of solar cell can be described by a simple equivalent circuit. Figure 8.2 (left hand side) depicts the so-called one diode model. The solar cell is represented by a diode with a parallel shunt resistance R_{SH}, which takes the finite resistance of the device into account. The series resistance R_S originating in the contact resistance is represented by an additional series resistance R_S. Finally the photo current I_{ph} is realised by a parallel current source, with a current opposite to the forward direction of the diode. The resulting I-V characteristic of the equivalent circuit is shown in figure 8.2 (right hand side). The intersection of the I-V curve with the coordinate axes define the short circuit current I_{SC} and the open circuit voltage V_{OC}. The maximum power point (MPP) and the corresponding voltage V_{MPP} and current I_{MPP} are

also denoted in the plot.

A measure of the ideality of the solar cell is the fill factor FF as defined in the following equation:

$$FF = \frac{I_{MPP} \cdot V_{MPP}}{I_{SC} \cdot V_{OC}} \tag{8.1}$$

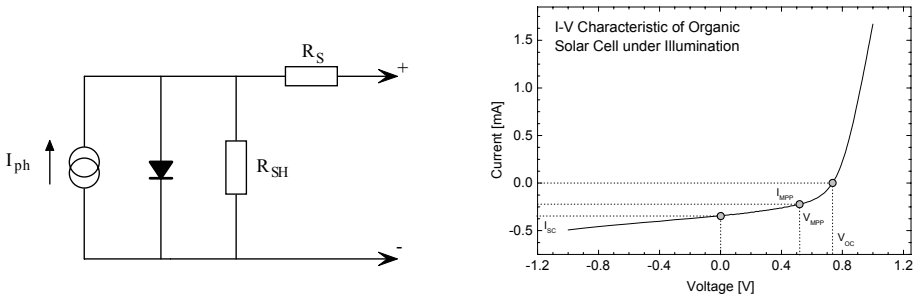

Figure 8.2:
One diode model of a solar cell (left hand side) and typical I-V characteristic of an organic solar cell under illumination (right hand side).

Note, that solar cells with a very high series resistance exhibit a flat, quasi-Ohmic behaviour [137]. Consequently, the fill factor is then 25%, which is virtually the lower limit for a device that shows a photovoltaic effect.

8.1.2. Organic Solar Cells

Organic solar cells take advantage of organic semiconductors. For a detailed introduction to organic semiconductors, see chapter 1. Upon absorption of a photon with sufficient energy, an electron is excited from the HOMO to the LUMO of the absorbing material. In contrast to inorganic semiconductors, the electron-hole pair (exciton) is not dissociated immediately. Due to the low relative permittivity of organic semiconductors and the small delocalisation length of the charge carriers [138], the exciton binding energy of 0.1eV to

2eV [139-145] exceeds the energy of thermal phonons considerably (~26meV at 300K). Thus, a strong electric field is necessary to split the exciton. Such a field is present at the interface of an electron donor and an electron acceptor material. If the exciton reaches during its lifetime through diffusion such an interface, the electron can be transferred from the LUMO of the donor to the LUMO of the acceptor if it is energetically preferable. Once the electron and the hole are separated from each other, the further process is similar to conventional solar cells.

The high absorption coefficient of organic semiconductors (see section 5.3) enables the fabrication of very thin devices with film thicknesses in the range of 100nm. However, the exciton diffusion length is only in the range of ~10nm [146, 147], which means that conventional bi-layer devices are very ineffective in dissociating excitons. In the following section an alternative approach is described, which circumvents this problem.

8.1.3. Bulk Heterojunction Solar Cells

As mentioned in the previous section the conventional bi-layer approach is not suitable for organic solar cells. In this section, the bulk heterojunction concept is introduced and the working principle is explained.

The basic idea of the bulk heterojunction concept is to blend a donor and an acceptor material. The traditional bi-layer of a solar cell is replaced by such a blended layer, in order to create a three-dimensional distributed donor-acceptor interface. The nanoscopic blending ensures that generated excitons reach a donor-acceptor interface within their lifetime [27], leading to an ultra fast photo-induced charge transfer and an internal quantum efficiency of almost 100% [148, 149]. Figure 8.3 shows the basic layout of a bulk heterojunction solar cell, as prepared within this work. The solar cell consists of a glass substrate (white), with a transparent electrode made of indium tin oxide ITO (light grey). In between the ITO and the active layer (red), an additional conducting layer is applied (blue). The active layer of the solar cells prepared and characterised in this work consisted of a blend of a PPV derivative and PCBM. Finally, the active layer is connected by an aluminium electrode (dark grey). The intersection of the two electrodes defines the surface area of the solar cell. A more detailed explanation of the individual

layer is given below.

The front electrode of the solar cell consists of indium tin oxide ITO. ITO is a highly doped degenerated n-type semiconductor. The most important property of ITO that makes it interesting for the application in solar cells is its transparency. Thus, shadowing effects caused by the front electrode as known from traditional solar cell designs are avoided. Yet the conductivity is rather high and lies in the range of 10^6S/m [150-154].

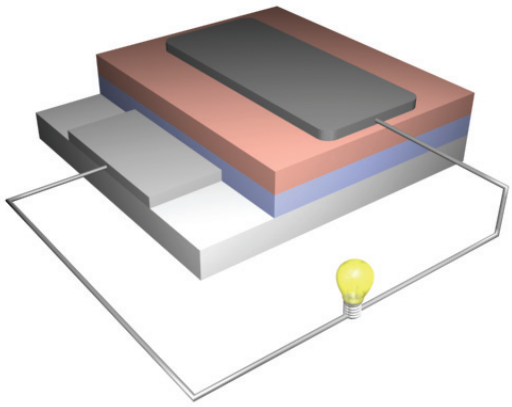

Figure 8.3:
Schematic drawing of a bulk heterojunction solar cell, consisting of a glass substrate (white), an ITO electrode (light grey), a PEDOT:PSS layer (blue), an active layer (red) and an aluminium electrode (dark grey). In this drawing, the sunlight is incident from the bottom. Note that the drawing is not true to scale.

The next layer consists of poly(3,4-ethylenedioxythiophene) PEDOT highly doped with polystyrenesulfonate PSS. The chemical structure is depicted in figure 8.4. PEDOT:PSS is a commercially available conducting polymer. The PEDOT:PSS layer serves two purposes. First, it smoothens the rough surface of the ITO layer, reducing the possibility of shortcuts. Second, it promotes the transfer of holes between the ITO electrode and the HOMO of the donor material [66, 148]. The conductivity of an annealed PEDOT:PSS film

perpendicular to the film plane lies in the range of 10^{-4}S/m, while the in-plane conductivity is about two orders of magnitude higher [155].

Figure 8.4:
Chemical structure of poly(3,4-ethylenedioxythiophene) PEDOT (left hand side) and polystyrenesulfonate PSS (right hand side).

As already mentioned, the active layer consists of a blend of a PPV derivative and PCBM. At the interface of the two materials the excitons, which were generated in the polymer, can dissociate. The holes travel by means of a hopping process (see section 1.4) through the PPV derivative to the PEDOT:PSS layer. The electrons percolate through the PCBM to the aluminium electrode.

8.2. Simulation of Solar Cells

In this section, a simple empirical model is presented, to estimate the performance of a solar cell based on the material properties of the involved materials. First, the theoretical background is explained and then the model is applied to the four PPVs studied.

8.2.1. Theoretical Introduction

The model described here to estimate the efficiency, is based on reference [156]. The efficiency η of a solar cell is given by the ratio of the electrical output power P_{out} and the optical power of the incident light P_{in}:

$$\eta = \frac{P_{out}}{P_{in}} \tag{8.2}$$

The output power can be expressed in terms of the short circuit current I_{SC}, the open circuit voltage V_{OC} and the fill factor FF. Equation (8.2) can then be rewritten as follows:

$$\eta = \frac{FF \cdot I_{SC} \cdot V_{OC}}{P_{in}} \tag{8.3}$$

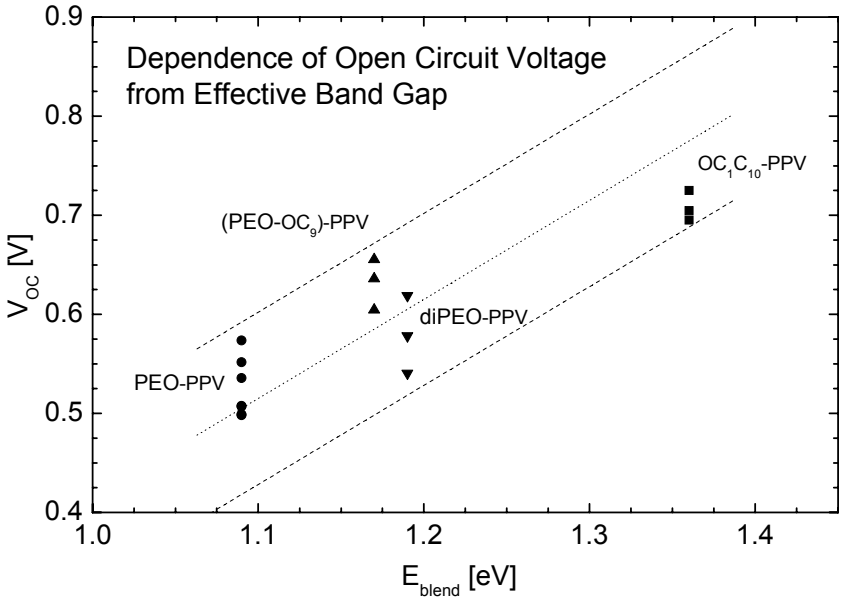

Figure 8.5:
Comparison between the experimentally obtained open circuit voltage V_{OC} and the effective band gap of the blend E_{blend}. The dotted line denotes a least-square fit and the dashed lines the 90% prediction band.

In reference [156] a linear dependence of the open circuit voltage with the effective band gap E_{blend} of the material blend used is proposed, i.e. the difference between the LUMO of the electron acceptor material and the HOMO of the electron donor material.

$$E_{blend} = \left| E_D^{HOMO} - E_A^{LUMO} \right| \tag{8.4}$$

Figure 8.5 shows a plot of experimentally determined open circuit voltages against the effective band gap for different solar cells prepared from PPV:PCBM blends. The plot confirms the linear dependence. From a linear least-square fit with slope 1V/eV (dotted curve), an offset voltage of -0.58V ± 0.01V is extracted. The dashed lines denote the 90% prediction band. Note that the experimentally obtained V_{OC} varies up to 75mV for a given material system. Using the fit result, the open circuit voltage can be estimated by the following expression:

$$V_{OC} = \frac{1}{q} \cdot \left(E_{blend} - 0.58eV \right) \tag{8.5}$$

with the effective band gap E_{blend} in electronvolts and the elementary charge q. Note that the determined offset voltage differs from the one in [156]. The reason is a difference in the LUMO value used for PCBM. This raises the question, whether the offset is of genuine physical origin or whether it is a measurement artefact of cyclic voltammetry, which was used to determine the LUMO level. In cyclic voltammetry, the absolute HOMO and LUMO value depend on the work function of the used reference electrode and the exact extraction procedure.

The short circuit current density can be estimated by integrating the product of the external quantum efficiency EQE(λ) and the spectrum S(λ) from the start of the spectrum λ_0 to the optical band gap of the polymer λ_{gap}.

$$j_{SC} = q \cdot \int_{\lambda_0}^{\lambda_{gap}} EQE(\lambda) \cdot S(\lambda)\, d\lambda \tag{8.6}$$

Thereby it is assumed that the light is mainly absorbed by the polymer and not by the electron acceptor (here PCBM). For the calculations, the standard spectrum AM1.5g normalised to 1000W/m^2 was converted into photon flux per wavelength. As a realistic estimation for an optimised organic solar cell, a constant external quantum efficiency of 65% is assumed.

Typically, an optimised organic solar cell reaches a fill factor of 65%. Using this value with equations (8.3) to (8.6), an estimate for the efficiency of a solar cell can be calculated.

8.2.2. Results and Conclusions

The model described in the previous section was applied to the four PPVs studied blended with PCBM. For the LUMO of PCBM a value of -3.96eV was used, as determined from cyclic voltammetry. The HOMO values and the optical band gap of the PPVs can be found in table 1.1. The calculated solar cell parameters are listed in table 8.1.

Polymer	V_{OC} [eV]	j_{SC} [mA/cm^2]	η [%]
OC_1C_{10}-PPV:PCBM	*0.78*	*7.9*	*4.0*
PEO-PPV:PCBM	*0.51*	*8.2*	*2.7*
(PEO-OC_9)-PPV:PCBM	*0.59*	*7.9*	*3.0*
diPEO-PPV:PCBM	*0.61*	*8.2*	*3.2*

Table 8.1:
Simulated solar cell parameters for a solar cell prepared from a blend of one of the four studied PPVs with PCBM.

The estimated short circuit density was ~8mA/cm^2 for all PPVs. This is a result of the almost identical optical band gap of the four polymers. The open circuit voltage however differed significantly. While OC_1C_{10}-PPV yielded the highest V_{OC} of 0.78V, the PEOs suffered from the lower absolute value of there HOMO levels. Consequently, the efficiency was lower. The expected efficiency of an OC_1C_{10}-PPV:PCBM solar cell is 4%, while the maximum efficiency for PEO:PCBM solar cell is expected to be around 3%.

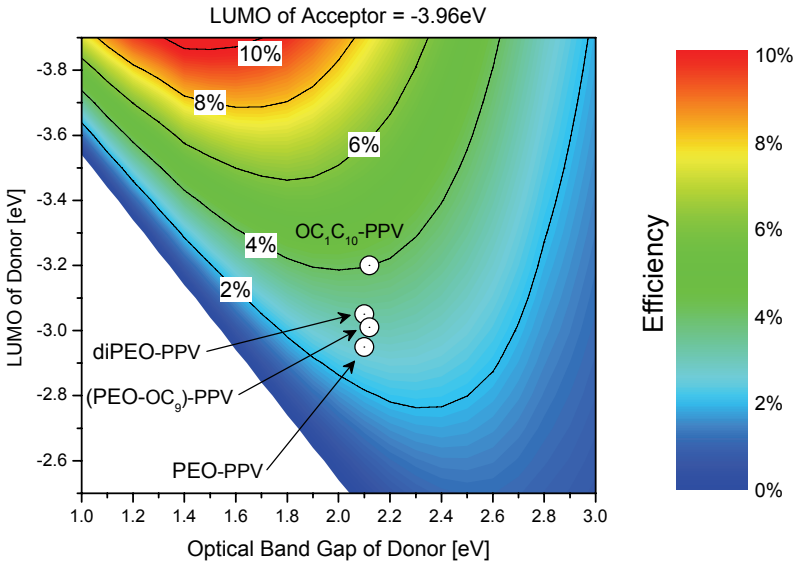

Figure 8.6:
Simulated efficiency of solar cells with varying band gap and LUMO level of the electron donor material (absorber). The LUMO level of the electron acceptor was assumed to be -3.96eV (PCBM).

Figure 8.6 shows an efficiency map of solar cells with varying band gap and LUMO level for the electron donor material (absorber). For the acceptor material, the LUMO of PCBM was used. The contour plot shows, that the efficiency exceeds 10% when the difference of the two LUMO levels tends to

zero. However, it must be noted that a minimal energy difference between the LUMO of the electron donor and the LUMO of the electron acceptor is necessary in order to dissociate the excitons. Thus, it is crucial to decrease the difference of the LUMO levels and to minimise the dissociation energy of the excitons at the same time, in order to increase the open circuit voltage and thus the efficiency. The circles in figure 8.6 denote the projected efficiency for the four studied PPVs.

8.3. Experimental Details

For the solar cells prepared in this work, glass substrates covered with a 10nm silica layer and 100nm ITO were purchased from Merck. The substrates were cut to a size of 25mm × 25mm and the ITO was patterned to obtain a layout with four 10mm × 10mm ITO pads in the corners of the substrates (see left hand side in figure 8.7). The cleaning of the substrates was identical to the procedure described in section 3.2. A detailed description of the entire preparation process can be found in appendix 10.1.4.

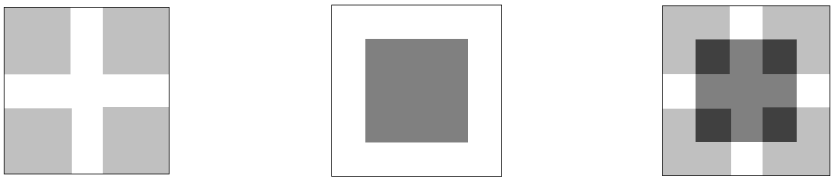

Figure 8.7:
The light grey area indicates the patterned ITO layer (left hand side). The dark grey square (middle) depicts the aluminium electrode. The intersections of the two electrodes (right hand side) define four solar cells with a size of 5mm × 5mm each.

Before preparing the active layer, PEDOT:PSS (Baytron P purchased from H. C. Starck) was spin coated on the substrates. Since PEDOT:PSS is dissolved in water, the PEDOT:PSS film was annealed on a hotplate after it was spin coated (15 minutes at 110°C). The annealing ensures that the water is evaporated completely. Next, the active layer was spin coated. The samples

were then placed in an evaporator. During evacuation, residual solvent could evaporate. The preparation of the solar cells was completed by evaporating a ~50nm aluminium electrode on top of the samples. Figure 8.7 (middle) shows the aluminium electrode (dark grey). The intersection of the ITO pads and the aluminium electrode defined four solar cells with a size of 5mm × 5mm (see right hand side of figure 8.7).

Before contacting the solar cells, the four corners of the substrate were cleaned and silver paste was applied on ITO and aluminium electrodes. The sample was then placed in a holder and contacted with spring contact probes. The solar cells were illuminated by a 150W Oriel solar simulator. The intensity of the AM1.5g-like spectrum was adjusted to yield roughly 1000W/m^2. Before acquiring an I-V characteristic, the lamp was given 30 minutes to heat up. The I-V curve was measured with a Keithley 2400. The voltage was swept from -1V to 0V in 0.1V steps and from 0V to 1V in 0.01V steps. The preparation and characterisation took place in an inert nitrogen atmosphere.

The open circuit voltage and the short circuit current were extracted as intersection with the coordinate axes. The reciprocal of the slope at these two points was taken as an estimate for the series resistance R_S and the shunt resistance R_{SH}. The fill factor FF was calculated from the maximum power point, the open circuit voltage and the short circuit current.

8.4. Experimental Results

8.4.1. Comparison of Different PPV:PCBM Blends

Figure 8.8 shows the I-V characteristics of PPV:PCBM solar cells under illumination. The blend ratio was varied from 1:1, over 1:2 to 1:4. The OC_1C_{10}-PPV:PCBM solar cells show the well-known behaviour. The 1:1 blend clearly gives the worst solar cell performance. At higher PCBM concentrations, phase separation sets in (see figure 7.2) and the I-V curve improves. Finally at the highest PCBM concentration (80%) an optimal balance between absorption and percolation paths is reached [157].

For the PEO-PPV:PCBM blends phase separation starts at much lower PCBM concentrations (see figure 7.3). Consequently, the best solar cell was obtained

for the 1:1 blend. However, it is not clear why the 1:4 blend performed much worse than the 3:7 blend. The morphology depicted in figure 7.3 did not differ noticeably and the reduced absorption because of the lower polymer concentration (20% vs. 30%) cannot fully explain such a big difference of the current density. The (PEO-OC_9)-PPV:PCBM solar cells performed similar for all three tested ratios. This is a direct consequence of the similar morphology of the three blends (see figure 7.4). The degree of phase separation is similar to the PEO-PPV:PCBM samples with a blend ratio of 1:2 and 1:4 (compare figure 7.3 and figure 7.4). Consequently, this results in a comparable short circuit current density in the range of 0.9mA/cm^2 to 1.3mA/cm^2. This shows, that replacing a polymer by another polymer with similar electrical and optical properties (see chapter 2 to 5) the solar cell performance does not change, as long as the same morphology is guaranteed.

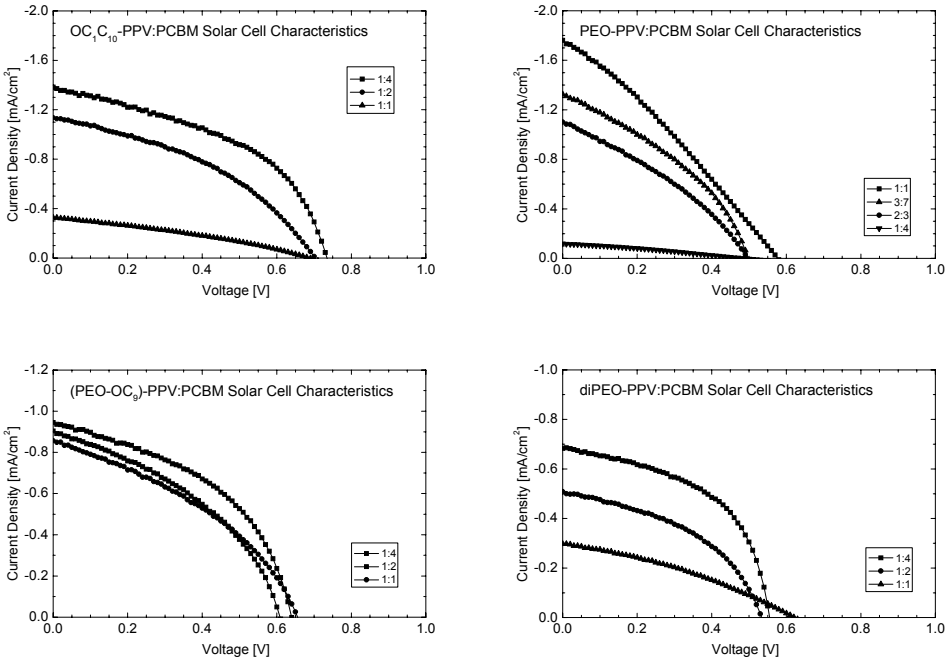

Figure 8.8:
Solar cell characteristics of various PPV:PCBM blends under illumination.

Finally, the diPEO-PPV:PCBM solar cells show a surprisingly good solar cell characteristic, given the bad morphology depicted in figure 7.5. The solar cell with a 1:1 blend ratio however results in a much lower current density. This is attributed to the reduced donor-acceptor interface area, which results from the large PCBM clusters.

In general, the short circuit current density was somewhat lower than expected from the simulations of section 8.2. The calculations predicted a short circuit current density of ~8mA/cm^2. This value was obtained for a rather high fill factor of 65%. The fill factors of the characterised solar cells however ranged from ~30% to ~50%. Thus, replacing the original value for the fill factor by the experimentally obtained values, would lead to a more realistic estimate of the short circuit current density.

Polymer	**OC_1C_{10}-PPV**	**PEO-PPV**	**(PEO-OC_9)-PPV**	**diPEO-PPV**
PPV:PCBM Ratio	*1:4*	*1:1*	*1:4*	*1:4*
V_{OC} [V]	*0.73*	*0.57*	*0.64*	*0.58*
j_{SC} [mA/cm^2]	*1.20*	*1.45*	*0.88*	*0.66*
V_{MPP} [V]	*0.52*	*0.29*	*0.45*	*0.43*
j_{MPP} [mA/cm^2]	*0.73*	*0.81*	*0.57*	*0.44*
FF [%]	*43.5*	*28.1*	*45.8*	*50.1*
R_S [kΩ]	*0.4*	*1.2*	*0.5*	*0.5*
R_{SH} [kΩ]	*5.5*	*2.4*	*9.5*	*13.0*

Table 8.2:
Averaged solar cell parameters for the best ratio of the four individual PPV:PCBM solar cells.

Further it is noted, that the simulation assumed complete absorption of the sunlight with photon energies above the band gap. This can only be reached by increasing the thickness of the active layer. However, in a real solar cell an

increased film thickness is detrimental to the charge carrier transport. Consequently, the trade-off for a higher absorption is the worse charge transport.

Table 8.2 lists the averaged solar cell parameters for the best blend ratio of the four individual PPV:PCBM blends. The measured open circuit voltage V_{OC} lies notably close to the values predicted by the model of section 8.2. A look at the series resistance R_S reveals the reason for the rather low fill factors [137]. The extracted series resistances of 0.5kΩ to 1kΩ are too big to allow a good solar cell performance. Since the same behaviour was observed for all four PPV derivatives and for quite different film morphologies, it is assumed, that a problem of the preparation causes the high series resistance. A possible reason is the aluminium electrode, the evaporation of which has shown to be critical before.

8.4.2. Optimisation of PEO-PPV:PCBM Based Solar Cells

In the previous section it was shown, that the most promising replacement for OC_1C_{10}-PPV is PEO-PPV. Further, the best solar cells were obtained for a blend ratio of 1:1. In order to improve the solar cell performance further, the thickness of the active layer was optimised. Figure 8.9 shows I-V characteristics of PEO-PPV:PCBM solar cells of various thicknesses. The thicknesses ranged from ~70nm to almost 450nm. Interestingly the I-V curves differed only slightly. Only the sample with a thickness of ~360nm showed a higher short circuit current density and the ~445nm sample a somewhat smaller open circuit voltage. The solar cell parameters were extracted and averaged for each thickness over several solar cells. In figure 8.10, the resulting solar cell parameters are plotted against the thickness of the active layer. For sake of better comparison, the relative values are plotted. Except for the series resistance, the highest value obtained was set to 100%.

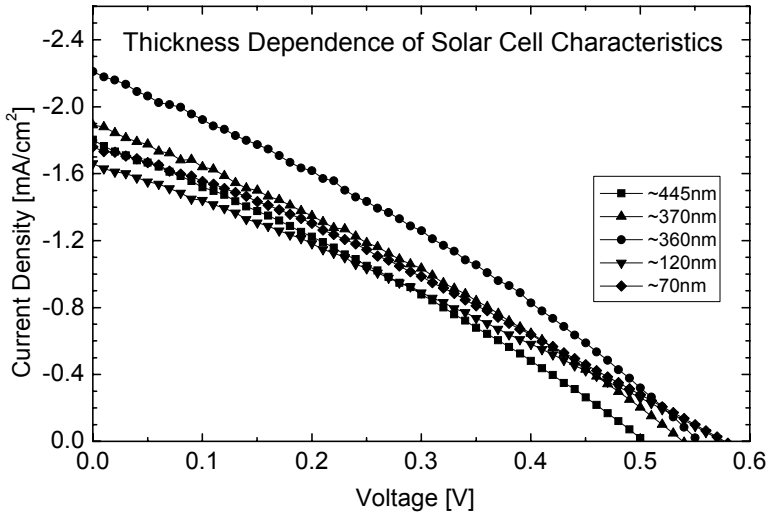

Figure 8.9:
I-V characteristics of PEO-PPV:PCBM 1:1 solar cells under illumination.

The highest open circuit voltage V_{OC} was obtained for the ~120nm sample, while the highest voltage at the maximum power point V_{MPP} was obtained for ~360nm film. For the ~370nm device the short circuit current density j_{SC} and the current density at the maximum power point j_{MPP} was maximal. The highest shunt resistance R_{SH} was surprisingly obtained for the thinnest solar cell. The best series resistance R_S was again obtained for the ~360nm device. As expected the fill factor exhibited therefore its maximum for the same thickness. Consequently, the solar cell with an active layer thickness of ~360nm yielded the highest efficiency. A detailed list of all solar cell parameters is given in table 8.3 for the individual thicknesses. Again, the rather high series resistance must be noted, which leads to a poor fill factor of around 30%. In order to optimise the solar cell performance, it is therefore crucial to reduce the series resistance. If the aluminium electrode causes the high resistance, introduction of an intermediate layer of LiF could improve the device [149, 158, 159]. Further annealing of the samples could also enhance the contacts [160, 161].

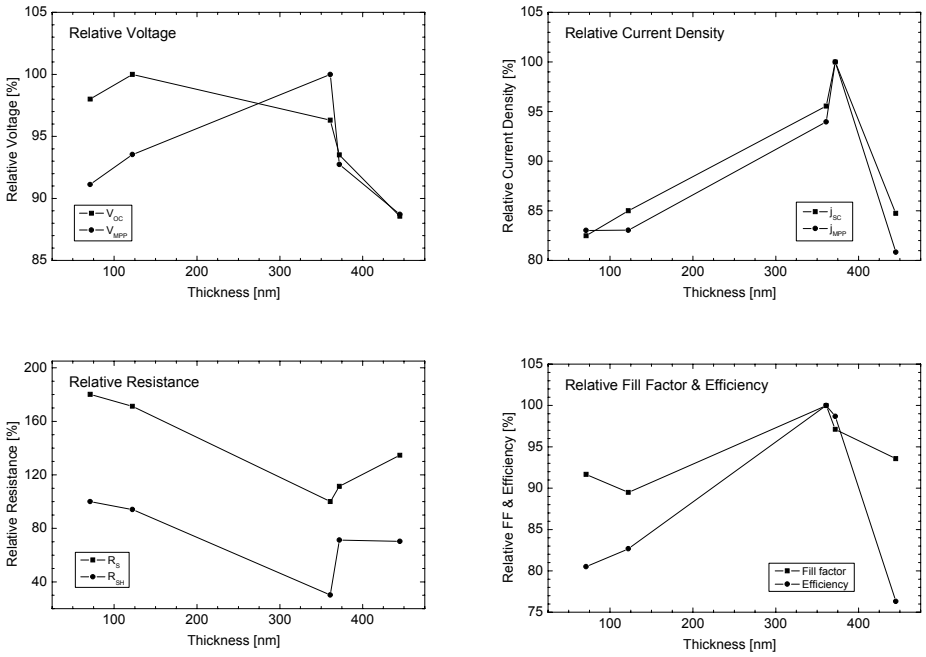

Figure 8.10:
Relative averaged solar cell parameters plotted against the film thickness of the active layer of a PEO-PPV:PCBM solar cell with 1:1 blend ratio.

It is surprising that the maximum of the efficiency appears at such a high thickness. Given the rather high absorption coefficient of PEO-PPV compared to OC_1C_{10}-PPV (see section 5.3) and the high polymer concentration of 50%, it was expected, that sufficient absorption of the sunlight is already reached at a smaller film thickness. However, since the optical behaviour depends also on the intermolecular interaction, the results obtained for pure polymer films are not directly comparable with the situation present in blends. It is suggested, that the reason for the maximum of the efficiency at ~360nm origins in the smaller series resistance. As mentioned before the high series resistance could be related to problems of the preparation during the evaporation of the aluminium electrode. However, since the aluminium electrode of several devices with differing film thickness was evaporated at the same time, it is not clear, why thicker devices had a lower series resistance.

Thickness	~70nm	~120nm	~360nm	~370nm	~445nm
V_{OC} [V]	*0.56*	*0.57*	*0.55*	*0.54*	*0.51*
j_{SC} [mA/cm^2]	*1.43*	*1.48*	*1.66*	*1.74*	*1.47*
V_{MPP} [V]	*0.28*	*0.29*	*0.31*	*0.29*	*0.28*
j_{MPP} [mA/cm^2]	*0.81*	*0.81*	*0.92*	*0.97*	*0.79*
FF [%]	*28.4*	*27.8*	*31.0*	*30.1*	*29.0*
R_S [kΩ]	*1.2*	*1.2*	*0.7*	*0.8*	*0.9*
R_{SH} [kΩ]	*2.5*	*2.4*	*0.8*	*1.8*	*1.8*

Table 8.3:
Averaged solar cell parameters for different thicknesses of the active layer of a PEO-PPV:PCBM solar cell with a 1:1 blend ratio.

Nevertheless, it was demonstrated that through optimisation of blend ratio and film thickness the solar cell performance increased significantly (see figure 8.10).

9. Summary and Outlook

9.1. Summary

The scope of this work was to gain deeper insight in the charge carrier transport of organic semiconductors and to understand the influence of different material parameters on electrical properties, the morphology of polymer:fullerene blends and the performance of bulk heterojunction solar cells. Furthermore, the objective was to understand how to interpret the variety of mobility values obtained for the same material from different measurement techniques. In the following sections, the obtained results are summarised.

9.1.1. Electrical Characterisation

In chapter 2 to 4, three different characterisation techniques and a total of ten different extraction methods were employed to determine the charge carrier mobility of polymer films. Chapter 2 used field-effect transistors to probe the mobility in the plane of the spin coated film. In chapter 3 and 4, sandwich devices were prepared and the mobility perpendicular to the spin coated film was determined. Due to the high disorder of the polymers, a direction dependence was no observed. However the different extraction methods used, lead to different mobility values of the same material, depending on the effects, which were taken into account for the extraction.

It is well-known that the charge carrier mobility follows an exponential behaviour when increasing the electric field. This is usually neglected when performing FET measurements. When the mobility is extracted from either the transconductance (section 2.3.1) or the conductance (section 2.3.2) in the linear regime, it is implicitly assumed that for the low source-drain voltages applied, the field-independent part of the mobility is probed. For the mobility values extracted from the transfer characteristic in the saturation regime (section 2.3.3), this assumption is clearly not true anymore. In this case it was ensured, that the electric field was at least kept constant.

However, the chosen field of 2MV/m was entirely arbitrary. To overcome these problems an alternative approach was used (section 2.4). The source-drain voltage was kept constant, i.e. the mobility was extracted for one specific field. Repeating the measurement for several different source-drain voltages the field dependence could be taken into account. The same approach was used, when extracting the mobility from impedance spectroscopy (chapter 4). The applied DC bias voltage was constant during measurement and repetitive measurements at different voltages yielded the field-dependent mobility. Alternatively the field dependence can be directly included in the applied models, for instance as carried out for the results of space-charge limited current measurements (chapter 3). The comparison between results of techniques that implicitly assume a constant mobility and the results of techniques that explicitly take the field dependence into account show, that the initial assumption that the mobility is constant in the linear regime of FETs is not correct.

Another important factor, which has to be considered when extracting the mobility, is the series resistance of the characterised device. All devices prepared within this work exhibited are rather large series resistance, most probably originating in the contact between metal and polymer. Neglecting this series resistance when extracting the mobility from the transconductance, lead to an underestimation of the mobility value. There are two possibilities to take the series resistance into account. Either the series resistance is directly included in the applied model or the mobility values are corrected afterward by comparing the results obtained for different device geometries (i.e. channel lengths). The latter approach was applied to the FET measurements of section 2.3.2 and 2.3.3. The disadvantage of this technique is the fact, that several devices must be characterised and compared. In case of a varying series resistance, the results are afflicted with a relatively large error. Taking the series resistance directly into account as in section 2.4 rectifies this shortcoming for the FET measurements. In the SCLC measurements, the series resistance was included by introducing an offset voltage in the Mott-Gurney law. Although the resulting equation described the measurement data well, it is noted that this is an empirical approach, which is mathematically not correct. For impedance spectroscopy the used equivalent circuit accounted for the series resistance and thus for possible voltage drops.

Finally, for the FET measurements the gate voltage dependence must be considered. The gate voltage determines the charge carrier concentration in the channel. For high concentrations of trap levels, this has a large influence on the charge carrier mobility. This effect is neglected for the extraction methods that use the linear regime. For the extraction of the mobility from the transfer characteristic in the saturation regime, the gate voltage is limited to the range, where the effect is rather small. Only the extended approach of section 2.4 takes the gate voltage dependence directly into account. This leads to much lower FET mobility values. A comparison with SCLC measurements and impedance spectroscopy shows that the gate voltage is not negligible.

Space-charge limited current measurements are a simple alternative to FET measurements. They circumvent the problems with a gate voltage-dependent mobility. In chapter 3, it was demonstrated that the naive approach (section 3.3.1) to incorporate the field dependence into the Mott-Gurney law yields reasonable results. However it was also shown, that a more sophisticate approach (section 3.3.2) leads to smaller errors for the fit parameters. It was therefore suggested to use exclusively the extended approach in order to obtain accurate results.

In chapter 4, it was demonstrated that impedance spectroscopy is a powerful tool to determine the charge carrier mobility. However, the standard approach has to resort to a "semi-empiric" correction factor in order to convert the characteristic time extracted from the negative differential susceptance to the transit time. However, this correction factor depends on the degree of dispersion of the transport (see section 4.3.2). Hence, for highly dispersive transport, the correction factor can vary quit a bit. Consequently it is more accurate to employ the first-principle approach (section 4.3), which does not need to introduce such a correction factor. Additionally this approach yields detailed information on the degree of dispersion in form of the two dispersion parameters M and α.

In summary, it was shown that it is important to take the field dependence, the series resistance and the gate voltage dependence into account. If one or several of these effects are neglected, the obtained mobility values are not comparable anymore. It is therefore crucial to document precisely the procedure that was used to extract the mobility.

9.1.2. Electrooptical Properties and Polarity of PPVs

While chapters 2 to 4 dealt with the ambiguities of the electrical characterisation, chapter 5 treated the electrooptical properties of the polymers. From the chemical structures of the PPVs depicted in figure 1.3, it was expected that the PEOs were more polar. The relative permittivity extracted from impedance spectroscopy clearly confirmed this assumption (section 5.1). However, it showed to be difficult to predict the experimental results based on the molecular structure. It seems that the macroscopic permittivity is influenced by other factors then only the molecular structure of the polymer unit. For instance, regioregularity, chain length, entanglement, etc. can influence the macroscopic permittivity and lead to a more complicated connection with the microscopic polarisability than suggested by the Clausius-Mosotti law.

Evidently, the increased polarity of the PEOs leads to the question, whether the ordering behaviour of the polymers is affected by possible dipole-dipole interactions. In section 5.2, this question was studied by XRD measurements. It was shown that the polarity had not the expected effect on the ordering behaviour. Instead, it was suggested that other effects screen a possible dependence on the polarity. It was demonstrated that the number of repeating units, i.e. the chain length clearly influences the ordering behaviour. Alignment of longer chains appears to be hampered by the entanglement with other polymers.

Finally, the optical absorption coefficient of the PPVs was studied. Since the optical band gap is almost identical for all of the four studied PPVs, the absorption increases dramatically at the corresponding wavelength. Further, the maximum absorption is reached at roughly the same wavelength. However, the PEOs exhibited a higher absorption, with diPEO-PPV being nearly twice as absorbing as OC_1C_{10}-PPV at the peak. This indicates that the polar side chains of the PEOs lead to an increased intermolecular interaction that clearly influences the optical properties of the polymers in the bulk. For application of the PEOs in solar cells, this promises an increased light absorption of thinner films, which should be beneficial for the efficiency.

9.1.3. Morphology of PPV:PCBM Blends

After having studied the pure polymers, they were blended with fullerene derivatives. In chapter 7, the morphology of the blends was investigated.

The impact of several factors on the blend morphology was studied by means of atomic force microscopy. The combination of polymer, fullerene derivative and solvent is a very complex and dynamic system. This is further amplified by the fact, that the solvent is evaporating during spin coating and thus the composition of the solution is constantly changing. In chapter 7 the influence of the different polymers, the solvent used and the type of fullerene derivative on the morphology of the film was investigated. For the well-known combination of OC_1C_{10}-PPV and PCBM dissolved in chlorobenzene, it is known that a blend ratio of 1:4 yields a morphology that is most suitable for bulk heterojunction solar cells, i.e. the degree of phase separation ensures short pathways for the excitons to the next donor-acceptor interface as well as a sufficient percolation network for the electrons to reach the electrode. For the PEOs, it was demonstrated that this ideal ratio can vary a lot. PEO-PPV showed the best morphology for a blend ratio of 1:1, while for the other two PPVs it was not possible to reach a comparing morphology within the investigate range of blend ratios (from 20% PPV to 50% PPV). diPEO-PPV did not even exhibit a sufficient phase separation. There are several options to solve this problem. In section 7.3 the effect of the used solvent was studied. The results obtained from OC_1C_{10}-PPV:PCBM blends suggest that the boiling point of the solvent is one of the most important parameters for the phase separation process. This is addressed to the fact that solvents with a lower boiling point like chloroform evaporate more quickly. In contrast, the polarity of the solvent seems to have less influence, as long as the materials dissolve properly.

As mentioned before the more polar PEOs exhibited a significantly different behaviour upon phase separation. It was therefore studied, whether the intermixing behaviour of the PEOs can be improved by replacing PCBM with more polar fullerene derivatives. Especially the most polar fullerene derivative studied C_{60}-5 had a large impact on the phase separation. In fact, no phase separation could be observed for this specimen. An additional problem was caused by what appears to be a clustering of the C_{60} molecules when they are still in solution. These clusters persist in the spin coated film, resulting in a bad

morphology. Finally, a similar effect was observed when adding a surfactant to the solution. The prepared films were very rough, because most of the C_{60} clustered together, to form large chunks located in a rather smooth polymer matrix.

From the large number of morphology experiments carried out, it was concluded that the combination of PEO-PPV:PCBM in chlorobenzene with a blend ratio of 1:1 was most suitable to prepare solar cells. The morphology was comparable with OC_1C_{10}-PPV:PCBM 1:4 blends. The rather high polymer concentration of 50% in contrast to 20% for OC_1C_{10}-PPV increases the optical absorption and should be beneficial to solar cells. Further, the results of the optical characterisation showed that PEO-PPV had a higher absorption coefficient than OC_1C_{10}-PPV.

9.1.4. Solar Cell Characterisation

In chapter 8, the results obtained from the characterisation of the pure polymers and the blends were used to prepare solar cells. The previous results directed the focus on a combination of PEO-PPV and PCBM in chlorobenzene with a ratio of 1:1. Additionally the other PPVs were used to prepare solar cells, which served as a reference and which confirmed the inferior performance expected from the material characterisation. A simple model proofed to predict the open circuit voltage with acceptable accuracy. Further, the simulation results suggested that solar cells prepared from a PEO and PCBM cannot achieve the same performance as OC_1C_{10}-PPV:PCBM solar cells. This is related to the slightly smaller effective band gap and the resulting loss in open circuit voltage. Nevertheless, leaving an optimised donor material to later optimisation, the performance of PEO-PPV:PCBM solar cells was improved by increasing the film thickness to ~360nm. The rather large film thickness was surprising, given the better absorption properties of PEO-PPV discussed earlier. It was therefore suggested, that the performance is strongly affected by the series resistance as already observed for the pure polymer.

The next section gives an overview over possible ways to improve the performance of PEO-based solar cells. It is expected that the gap between PEO-based solar cells and OC_1C_{10}-PPV-based solar cells will narrow, once more experience is gained with these novel materials.

9.2. Outlook

9.2.1. Electrical Characterisation

In this section, some suggestions are made how to improve or extend the measurement techniques employed in this work.

In general, additional information could be obtained by introducing temperature-dependent measurements. For FET measurements, the gate voltage dependence was modelled by an empirical equation. The suggested physical approach (see section 2.4) however requires measurements at different temperatures. The physical model would yield additional information about charge carrier concentration and trap concentration. Moreover, the demonstrated problems of a high series resistance and the influence of annealing could be investigated more closely by measurements at different temperatures.

Further using electron-only devices the electron mobility could be extracted from SCLC measurements and impedance spectroscopy. For electron-only devices, the electrode material has to have a low work function close to the LUMO of the polymer under investigation. The commonly used calcium has shown to be critical because of its easy diffusion into the polymer film. Approaches that are more sophisticated can be used, e.g. a self-assembled monolayer [162] can tune the work function of a metal like silver to match the LUMO of the polymer.

Alternatively, impedance spectroscopy enables the extraction of the hole and the electron mobility at the same time. This is in particular interesting when studying the mobility in blends. However initial measurements have shown, that electron mobility and hole mobility of the studied blends differ by several orders of magnitude, making it impossible to probe both within the frequency window that is given by the current measurement equipment.

The suggested changes would not only improve the accuracy of the obtained results, but would also yield additional information, which would lead to a deeper insight. Further FET measurements could be simplified by switching from continuous measurements to pulsed measurements to avoid the observed strong bias stress effect (section 2.5.1).

9.2.2. Solar Cell Optimisation

It was demonstrated that PEOs are an interesting alternative to OC_1C_{10}-PPV for bulk heterojunction solar cells. The superior absorption property promises thinner active layers. However, the prepared solar cells could not benefit from this advantage. One reason is certainly the rather high series resistance. Therefore, it is crucial to reduce the series resistance as much as possible. It was noted, that the quality of the aluminium electrode left room for improvement. Further experiments have to be carried out in order to clarify whether the bad contacts are of principle nature or caused by a problem of the preparation process. Further, it has to be examined whether the series resistance can be reduced by introducing an intermediate LiF layer and annealing.

In reference [163], chloroform was used as an alternative solvent for PEO-based solar cells. This could be of interest for (PEO-OC_9)-PPV- and diPEO-PPV-based solar cells, where it was difficult to obtain the desired morphology. Further, the simulation results suggested that PCBM with a LUMO of -3.96eV is not ideal for the PEOs as an electron acceptor. The slightly bigger effective band gap of the PEOs leads to a loss in open circuit voltage. Therefore, it is suggested to replace PCBM by a fullerene derivative with an adjusted LUMO level.

10. Appendix

10.1. Preparation Details

10.1.1. Preparation Details for FETs

Solution Parameters:

All polymers were dissolved in chlorobenzene. The solutions were heated to 50°C and stirred at 1500rpm. Finally, the warm solutions were filtered through a 0.45µm filter.

Polymer	Batch ID	Solution No.	Concentration [% wt./vol.]	Preparation Time [h]
OC_1C_{10}-PPV	*PDO 121*	*271*	*0.5*	*16.5*
PEO-PPV	*PEO1-FMX-EP*	*268*	*0.8*	*13*
(PEO-OC_9)-PPV	*Pol67*	*265*	*0.8*	*16*
diPEO-PPV	*PEO2-FMX-pol*	*269*	*0.8*	*13*

Table 10.1:
Preparation details of the solutions used for preparation of the FET samples.

Spin Coating Parameters:

After the solution was cooled down to room temperature, 250µl were evenly spread before starting the spin coating programme. The spin coating programme consisted of three steps and was identical for all polymers.

	Step 1	Step 2	Step 3
Lid	*open*	*closed*	*open*
Speed [rpm]	*500*	*2000*	*500*
Acceleration [rpm/s]	*500*	*1000*	*500*
Time [s]	*4*	*4*	*180*

Table 10.2:
Spin coating parameters for the films used for FET characterisation.

Film Thickness:

After the samples were characterised the film thickness was determined. The film was partly removed by scratching it with a stylus. At several positions along the scratch, the thickness was measured with a surface profiler (Sloan Dektak^{3}ST). The film thickness varied by roughly 1nm across the entire surface of the chip.

Polymer	Sample	Thickness [nm]	Standard Deviation [nm]
OC_1C_{10}-PPV	*441-FET-271*	*32.4*	*0.9*
PEO-PPV	*442-FET-268*	*46*	*1*
(PEO-OC_9)-PPV	*439-FET-265*	*67*	*1*
diPEO-PPV	*440-FET-269*	*51*	*1*

Table 10.3:
Film thickness as determined with a surface profiler. The thicknesses varied by roughly 1nm across the entire surface of a sample.

10.1.2.Preparation Details for Sandwich Devices

Evaporation of Metal Contacts:

An Inficon XTC/2 deposition controller was used to evaporate the two metal electrodes. The palladium pellets (Kurt J. Lesker Company EVMPD35SHOT;

purity 99.95%) were placed on a tungsten boat (Kurt J. Lesker Company EVS22010W). Shadow masks were used to define the electrode layout (see figure 3.2). The evaporation chamber was then evacuated to a base pressure of 10^{-6}mbar. Since palladium sublimes, it was not possible to automatise the evaporation process. Instead, the power level was controlled manually. Especially for the top contact the deposition rate was kept as low as possible, in order to prevent penetration of palladium atoms through the polymer film, which would cause short cuts. The evaporation was interrupted when a nominal thickness of roughly 50nm was reached.

Solution Parameters:

The same solutions as in appendix 10.1.1 were used to prepare the polymer films (see table 10.1 for details).

Preparation of Polymer Film:

After the solution was cooled down to room temperature, 500µl were evenly spread before starting the spin coating programme (for OC_1C_{10}-PPV 300µl were sufficient because of the lower viscosity). The spin coating programme consisted of one step only and was identical for all polymers. The sample was accelerated at a rate of 1000rpm/s to a velocity of 1000rpm. The speed was kept constant for a few seconds to spin off excess solution. Then the spin coater was stopped and the sample was removed after it had dried completely. Hence, the process is more comparable to drop casting than spin coating. By keeping the spin coating process short, it was ensured that the films were sufficiently thick to avoid short cuts.

Film Thickness:

After the samples were characterised the film thickness was determined. The film was partly removed by scratching it with a stylus. At several positions along the scratch, the thickness was measured with a surface profiler (Sloan Dektak^{3}ST). The film thickness varied by a few nanometres across the surface of a capacitor. Due to the preparation technique, the variation over the entire substrate was much bigger.

Polymer	Sample	Electrode	Thickness [nm]	Std. Dev. [nm]
OC_1C_{10}-PPV	*451-FET-271*	*9*	*37*	*1*
		10	*70*	*3*
PEO-PPV	*428-FET-268*	*2*	*142*	*5*
		10	*972*	*5*
(PEO-OC_9)-PPV	*430-FET-265*	*9*	*135*	*2*
		10	*200*	*4*
diPEO-PPV	*429-FET-269*	*2*	*108*	*3*
		10	*230*	*2*

Table 10.4:

Film thickness as determined with a surface profiler. The thicknesses varied quite a lot over the entire substrate (up to a factor of 8). However, across the characterised electrodes the standard deviation ranged only from 1nm to 5nm.

10.1.3.Preparation Details for Reflection/Transmission Measurements

Solution Parameters:

All polymers were dissolved in chlorobenzene. The solutions were heated to 50°C and stirred at 1500rpm.

Polymer	Batch ID	Solution No.	Concentration [% wt./vol.]	Preparation Time [h]
OC_1C_{10}-PPV	*PDO 121*	*200*	*0.5*	*15.75*
PEO-PPV	*PEO1-FMX-EP*	*201*	*1.1*	*15.75*
(PEO-OC_9)-PPV	*Pol67*	*202*	*0.8*	*15.75*
diPEO-PPV	*PEO2-FMX-pol*	*203*	*0.5*	*15.75*

Table 10.5:

Preparation details of the solutions used to spin coat the films for transmission and reflection measurements.

Substrate Cleaning:

The glass substrates were thoroughly cleaned. First, the glass was cleaned with a 1:20 soap solution (Buehler Ultramet 2 Sonic Cleaning Solution). Then the substrate was placed in the same solution in an ultrasonic bath for 20 minutes. Afterwards it was rinsed with deionised water to remove soap residues. Subsequently it was sonicated in acetone for another 10 minutes. The cleaning process was completed by placing the sample for 10 minutes in boiling isopropanol and blowing it dry afterwards.

Spin Coating Parameters:

After the solution was cooled down to room temperature, 750µl were evenly spread before starting the spin coating programme. The spin coating programme consisted of three steps. The spin coating parameters were identical for all polymers, except for the speed of the second step. (PEO-OC_9)-PPV was spin coated at 500rpm, PEO-PPV and diPEO-PPV at 1000rpm and OC_1C_{10}-PPV at 1500rpm.

	Step 1	**Step 2**	**Step 3**
Lid	*open*	*closed*	*open*
Speed [rpm]	*500*	-	*500*
Acceleration [rpm/s]	*500*	*500*	*500*
Time [s]	*4*	*4*	*180*

Table 10.6:
Spin coating parameters used to prepare the film used for transmission and reflection measurements. The speed of the second step was different for each polymer (see text).

Film Thickness:

After the samples were characterised the film thickness was determined. The film was partly removed by scratching it with a stylus. At several positions along the scratch, the thickness was measured with a surface profiler (Sloan

Dektak^{3}ST). The film thickness varied by roughly 1nm to 2nm across the entire surface of the sample.

Polymer	Sample	Thickness [nm]	Standard Deviation [nm]
OC_1C_{10}-PPV	*336-MISC-200*	*62.5*	*0.8*
PEO-PPV	*337-MISC-201*	*113*	*1*
(PEO-OC_9)-PPV	*338-MISC-202*	*55.4*	*0.9*
diPEO-PPV	*339-MISC-203*	*31*	*2*

Table 10.7:
Film thickness as determined with a surface profiler. The thicknesses varied by roughly 1nm to 2nm across the entire surface of a sample.

10.1.4.Preparation Details for Solar Cells

Solution Parameters:

All polymers were blended with PCBM purchased from Solenne B. V. The blends were dissolved in chlorobenzene and the solutions were heated to 50°C and stirred at 1500rpm. The polymer:PCBM ratio is listed in table 10.8 along with other preparation parameters.

Solution No.	Polymer (Batch ID)	Blend Ratio	Concentration [% wt./vol.]	Preparation Time [h]
272	*PEO-PPV (PEO1-FMX-EP)*	*1:1*	*3*	*18*
272*	*PEO-PPV (PEO1-FMX-EP)*	*1:1*	*1.5*	*18*
273	*PEO-PPV (PEO1-FMX-EP)*	*2:3*	*3*	*18*
274	*PEO-PPV (PEO1-FMX-EP)*	*3:7*	*3*	*18*

Solution No.	Polymer (Batch ID)	Blend Ratio	Concentration [% wt./vol.]	Preparation Time [h]
276	*OC_1C_{10}-PPV (PDO 121)*	*1:4*	*2.5*	*18.5*
277	*OC_1C_{10}-PPV (PDO 121)*	*1:2*	*3*	*18.5*
278	*OC_1C_{10}-PPV (PDO 121)*	*1:1*	*3*	*18.5*
279	*(PEO-OC_9)-PPV (Pol67)*	*1:4*	*3*	*18.5*
280	*(PEO-OC_9)-PPV (Pol67)*	*1:2*	*3*	*18.5*
281	*(PEO-OC_9)-PPV (Pol67)*	*1:1*	*3*	*18.5*
282	*diPEO-PPV (PEO2-FMX-pol)*	*1:4*	*3*	*18.5*
283	*diPEO-PPV (PEO2-FMX-pol)*	*1:2*	*3*	*18.5*
284	*diPEO-PPV (PEO2-FMX-pol)*	*1:1*	*3*	*18.5*

Table 10.8:
Preparation details of the solutions used to spin coat the films for solar cells.

Substrate Cleaning:

For a description of the cleaning process, see the corresponding paragraph in section 10.1.3. The cleaning process was completed by a 15 minute UV/ozone treatment.

Preparation of PEDOT:PSS Layer:

A volume of 300µl of an aqueous PEDOT:PSS solution was evenly spread on the substrate. The spin coating programme consisted of only one 60 second step with a speed of 3000rpm at an acceleration of 1000rpm/s. After spin coating, the sample was placed for 15 minutes on a hotplate at 110°C to ensure complete evaporation of the water.

Preparation of Active Layer:

After the solutions were cooled down to room temperature, a small amount of 300µl to 500µl was evenly spread before starting the spin coating programme. The spin coating programme consisted of one step for the PEO-PPV:PCBM samples and of three steps for the remaining PPV:PCBM blends (see table 10.9 and table 10.10).

Sample No.	Lid	Speed [rpm]	Acceleration [rpm/s]	Time [s]
447-sol-272	*open*	*1000*	*1000*	*30*
448-sol-272	*open*	*3000*	*1000*	*60*
449-sol-272	*open*	*2000*	*1000*	*30*
457-sol-273	*open*	*2000*	*1000*	*15*
458-sol-274	*open*	*2000*	*1000*	*10*
459-sol-274	*open*	*1000*	*1000*	*5*
460-sol-272*	*open*	*2000*	*1000*	*60*
461-sol-272*	*open*	*3000*	*1000*	*60*

Table 10.9:
Spin coating programmes for PEO-PPV:PCBM samples.

For the remaining PPV:PCBM blends the first and last step of the spin coating programme were identical. The speed of the first and last step was 500rpm at an acceleration of 500rpm/s. The first step took 4 seconds, while the last step took 180 seconds. Both steps were performed with an open lid. The parameters of the second step are listed in the following table.

Sample No.	Lid	Speed [rpm]	Acceleration [rpm/s]	Time [s]
462-sol-276	*closed*	*1800*	*1000*	*4*
463-sol-277	*closed*	*2400*	*1000*	*4*
464-sol-278	*closed*	*3000*	*1000*	*4*
465-sol-279	*closed*	*1800*	*1000*	*4*
466-sol-280	*closed*	*2400*	*1000*	*4*
467-sol-281	*closed*	*3000*	*1000*	*4*
468-sol-282	*closed*	*1800*	*1000*	*4*
469-sol-283	*closed*	*2400*	*1000*	*4*
470-sol-284	*closed*	*3000*	*1000*	*4*

Table 10.10:
Parameters for the second step of the spin coating programme.

Evaporation of Metal Contacts:

The evaporation followed the same procedure as described in the corresponding paragraph of section 10.1.2. The aluminium pellets were purchased from Kurt J. Lesker Company (EVMAL40EX; purity 99.99%). A shadow mask was used to define the electrode layout (see figure 8.7). The evaporation was controlled manually and stopped when a thickness of roughly 50nm was reached.

Film Thickness:

After the samples were characterised the film thickness was determined. The film was partly removed by scratching it with a stylus. The thickness was determined at several positions. Since the measured thickness is the combined thickness of the PEDOT:PSS layer and the active layer, the PEDOT:PSS thickness was measured on a separate sample without active layer. The thickness measurement yielded 111nm ± 2nm for the PEDOT:PSS film. The values listed in table 10.11 are thicknesses of the active layers corrected for

the thickness of the PEDOT:PSS layer.

Polymers	Corrected Thickness [nm]	Standard Deviation [nm]
447-sol-272	*445*	*9*
448-sol-272	*361*	*11*
449-sol-272	*372*	*8*
457-sol-273	*291*	*5*
458-sol-274	*230*	*4*
459-sol-274	*210*	*5*
460-sol-272*	*122*	*7*
461-sol-272*	*71*	*7*
462-sol-276	*188*	*4*
463-sol-277	*288*	*3*
464-sol-278	*336*	*5*
465-sol-279	*162*	*4*
466-sol-280	*175*	*3*
467-sol-281	*170*	*4*
468-sol-282	*205*	*3*
469-sol-283	*241*	*4*
470-sol-284	*321*	*4*

Table 10.11:

Film thicknesses of the active layer, corrected for the thickness of the PEDOT:PSS layer.

10.2. Mathematical Derivations

10.2.1.I-V Characteristic of a Thin Film Transistor in the Linear Regime

In figure 2.1 the layout of a thin film transistor is depicted. The z-axis points perpendicular to the x- and y-axes to form a right-handed coordinate system. The following examination assumes a p-type channel, which is operated in the enhancement mode. Further, the gradual channel approximation [83] is used, where the gate field is perpendicular to the plane of the channel, i.e. it points in y-direction. This assumption is reasonable since the channel length L is usually much larger than the thickness of the insulating layer d_i. Therefore if the source-drain voltage is not much bigger than the gate voltage, the related fields behave correspondingly and the resulting gate field is almost perpendicular to the plane of the film. The voltage V(x) then increases gradual from 0V at the source contact to $|V_{SD}|$ at the drain contact. The gate voltage V_G does not depend on the x-position since the gate is highly-doped and thus very conductive.

In order to calculate the source-drain current $I_{SD}(x)$ the current density $j_{SD}(x, y, z)$ has to be integrated over y and z:

$$I_{SD}(x) = \iint j_{SD}(x, y, z)\, dy\, dz \tag{10.1}$$

The current density $j_{SD}(x)$ is given by the conductivity σ(x, y) and the electric field $E_x(x)$:

$$\begin{aligned} j_{SD}(x) &= \sigma(x, y) \cdot E_x(x) \\ &= -\sigma(x, y) \cdot \frac{dV(x)}{dx} \end{aligned} \tag{10.2}$$

After executing the integration over z and inserting equation (10.2) into equation (10.1), the following equation is obtained:

$$I_{SD}(x) = -W \int_{y=0}^{d(x)} \sigma(x,y) \frac{dV(x)}{dx}\, dy \tag{10.3}$$

with the x-dependent thickness d(x) of the induced conducting channel. The conductivity can be replaced by introducing the charge carrier concentration p(x, y) and the mobility μ(x):

$$\sigma(x,y) = q \cdot p(x,y) \cdot \mu(x) \tag{10.4}$$

with the elementary charge q. Equation (10.3) and (10.4) combine to:

$$\begin{aligned} I_{SD}(x) &= -W \cdot \mu(x) \int_{y=0}^{d(x)} q \cdot p(x,y)\, dy \cdot \frac{dV(x)}{dx} \\ &=: -W \cdot \mu(x) \cdot Q(x) \cdot \frac{dV(x)}{dx} \end{aligned} \tag{10.5}$$

Q(x) is the total charge per area in the channel. Q(x) can be determined by solving the Poisson equation for a specific problem. Below a simplified approach is followed in order to obtain a closed formula for the source-drain current. The total charge concentration can be split into an intrinsic part $Q_0(x)$ that is present before applying a gate voltage and an induced part ΔQ(x).

$$Q(x) = Q_0(x) + \Delta Q(x) \tag{10.6}$$

The induced charge depends of course on the capacitance c_i of the insulating layer and the voltage:

$$\Delta Q(x) = -c_i \cdot \left(V_G - V(x)\right) \tag{10.7}$$

After inserting equation (10.6) and (10.7) into equation (10.5) the following expression is obtained:

$$I_{SD}(x) = -W \cdot \mu(x) \cdot \left[Q_0(x) - c_i \cdot \left(V_G - V(x) \right) \right] \cdot \frac{dV(x)}{dx} \qquad (10.8)$$

In the stationary situation $I_{SD}(x)=I_{SD}$, integrating the left hand side over dx and the right hand side over dV(x) results in the well-known expression for the linear regime of a TFT [11-13, 18, 75, 90, 110, 111]:

$$\begin{aligned} I_{SD}\left(V_{SD}\right) &= \frac{W}{L} \cdot c_i \cdot \mu \left[\left(V_G - V_T \right) - \frac{V_{SD}}{2} \right] \cdot V_{SD} \\ V_T &:= \frac{Q_0}{c_i} \end{aligned} \qquad (10.9)$$

Note, that it was implicitly assumed that both, the mobility μ and the intrinsic charge concentration Q_0, are constant through out the channel. The threshold voltage V_T is positive if there are already mobile charges available before applying a gate voltage. However if the charges are trapped, the threshold voltage becomes negative. Note, that in contrast to inorganic, i.e. crystalline semiconductors the threshold voltage is not well-defined for organic materials. Therefore, it is better to think of it more as an additional fitting parameter rather than a physical quantity. Consequently, some authors denote it as V_0 instead of V_T [21, 81, 82, 111]. Nevertheless, throughout this work the parameter is always referred to as threshold voltage V_T.

If $|V_G-V_T|$ is large compared to $|V_{SD}|$ the charger carrier concentration along the channel is homogeneous. If $|V_{SD}|$ increases the voltage drop between gate and channel varies with x, because the source and drain are at significantly different potential. Since the drain potential is negative like the gate potential, the charge carrier concentration close to the drain contact becomes smaller than at the source contact. Eventually if $|V_{SD}| > |V_G-V_T|$ a depletion region is formed and the channel is pinched off. Since the depletion region increases

linearly with V_{SD}, the current saturates.

10.2.2.I-V Characteristic of a Thin Film Transistor in Saturation Regime

The equation derived in the previous section is only true for $|V_G-V_T| > |V_{SD}|$. For source-drain voltages larger than $|V_G-V_T|$ the channel is pinched off, i.e. equation (10.9) holds only true for source-drain voltages up to V_G-V_T. Inserting this boundary value into equation (10.9) yields:

$$I_{SD}\left(V_G - V_T\right) = \frac{1}{2} \cdot \frac{W}{L} \cdot c_i \cdot \mu \cdot \left(V_G - V_T\right)^2 \tag{10.10}$$

This equation does not only describe the I-V characteristic at this particular point, but for the entire saturation regime with $|V_G-V_T| < |V_{SD}|$ [8, 11, 12, 19, 21, 75, 85, 111, 112].

10.2.3.Correction of Mobility for Series Resistance

As already mentioned in equation (2.6) the total resistance R_{TOT} can be written as the sum of the series resistance R_S and the resistance of the channel R_{CH} itself:

$$R_{TOT} = R_S + R_{CH} \tag{10.11}$$

The channel resistance is determined by its geometry (length L, width W and film thickness t) and the conductivity σ:

$$R_{CH} = \frac{1}{\sigma} \cdot \frac{L}{W \cdot t} \tag{10.12}$$

The conductivity can be rewritten by using the mobility μ_0 and the charge carrier concentration p:

$$\sigma = q \cdot p \cdot \mu_0 \tag{10.13}$$

with the elementary charge q. Combining equation (10.12) and (10.13) yields:

$$R_{CH} = \frac{1}{q \cdot p \cdot \mu_0} \cdot \frac{L}{W \cdot t} \tag{10.14}$$

The same expression holds true for the total resistance and the channel length-dependent mobility μ(L) as determined in section 2.3:

$$R_{TOT} = \frac{1}{q \cdot p \cdot \mu(L)} \cdot \frac{L}{W \cdot t} \tag{10.15}$$

By inserting equation (10.14) and (10.15) into (10.11) and solving for μ(L) one obtains:

$$\mu(L) = \mu_0 \cdot \frac{1}{1 + \frac{R_S}{R_{CH}}} \tag{10.16}$$

or more convenient for channels with different width:

$$\mu(L) = \mu_0 \cdot \frac{1}{1 + \frac{W}{L} \cdot \frac{R_S}{R_{SHEET}}} =: \mu_0 \cdot \frac{1}{1 + \frac{W}{L} \cdot r} \tag{10.17}$$

with the sheet resistance R_{SHEET} of the film.

10.2.4.Electric Field at Collecting Electrode for SCLC

In section 3.1, an expression for the space-charge limited current SCLC was derived. The underlying equations were the Poisson equation:

$$\frac{dE}{dx} = \frac{\rho}{\varepsilon} \tag{10.18}$$

and the expression for the current density:

$$j = \rho \cdot \mu(E) \cdot E \tag{10.19}$$

This set of equations is completed by the very definition of the electric potential:

$$E = \frac{dV}{dx} \tag{10.20}$$

Note the uncommon sign convention of equation (10.20) (see reference [122] and references therein for details). Combining equation (10.18) and (10.19) and integrating over dx from the injecting electrode x = 0 to the collecting electrode x = t (t – film thickness) yields the already known equation:

$$j = \frac{\varepsilon}{t} \cdot \int_0^{E_C} \mu(E) \cdot E \, dE \tag{10.21}$$

Combining equation (10.19) and (10.20) yields:

$$j \cdot V = \varepsilon \cdot \int_0^{E_C} \mu(E) \cdot E^2 \, dE \tag{10.22}$$

The previous two equations can be merged by calculating the derivative of j·V in respect to j.

$$\frac{d}{dj}(j \cdot V) = t \cdot \frac{d \int_0^{E_C} \mu(E) \cdot E^2 \, dE}{d \int_0^{E_C} \mu(E) \cdot E \, dE} \tag{10.23}$$

The right hand side obviously reduces to $t \cdot E_C$ while the left hand side can be written as:

$$\frac{d}{dj}(j \cdot V) = V \cdot \left(1 + \frac{1}{\frac{d \ln j}{d \ln V}}\right) \tag{10.24}$$

The electric field at the collecting electrode E_C can then be expressed as:

$$E_C = \frac{V}{t} \cdot \left(1 + \frac{1}{\frac{d \ln j}{d \ln V}} \right) \tag{10.25}$$

Note, that in reference [122] also an expression for the field-dependent mobility is given.

10.2.5.Analytical Expression for the Impedance of a Sandwich Device

In this section, the impedance Z of a device consisting of a semiconductor sandwiched between two electrodes is derived. The derivation follows the approach described in reference [123].

The anode is supposed to form an Ohmic contact, while the cathode blocks electrons from being injected. Hence, the device exhibits a single carrier transport. A DC voltage is applied, superposed by a small AC perturbation. The mobility is assumed to be unaffected by the small AC voltage. In order to separate the DC from the AC contribution, the electric field E(x, t), the charge carrier density ρ(x, t) and the current density j(t) are split into a DC part (subscript DC) and an AC part (Greek letters on the right hand side):

$$\begin{aligned} E(x,t) &= E_{DC}(x) + \varepsilon(x,t) \\ \rho(x,t) &= \rho_{DC}(x) + \vartheta(x,t) \\ j(t) &= j_{DC} + \iota(t) \end{aligned} \tag{10.26}$$

The charge carrier density is given by the Poisson equation:

$$\frac{\partial E(x,t)}{\partial x} = \frac{q}{\varepsilon_0 \cdot \varepsilon_r} \cdot \rho(x,t) \tag{10.27}$$

with the elementary charge q, the permittivity of vacuum ε_0 and the relative

permittivity ε_r of the semiconductor. Further, the current density can be written as:

$$j(t) = q \cdot \rho(x,t) \cdot \mu \cdot E(x,t) + \varepsilon_0 \cdot \varepsilon_r \cdot \frac{\partial E(x,t)}{\partial t} \tag{10.28}$$

Inserting equation (10.26) and (10.27) into equation (10.28), the current density can be split into three contributions:

$$j(t) = j_{AC \to DC} + j_{AC} + j_{DISP} \tag{10.29}$$

$j_{AC \square DC}$ is the response of the DC current density on the AC perturbation, j_{AC} is the additional current density due to the AC voltage and j_{DISP} is the displacement current density due to carrier relaxation:

$$\begin{aligned} j_{AC \to DC} &= q \cdot \mu \cdot \rho_{DC}(x) \cdot \varepsilon(x,t) \\ j_{AC} &= \varepsilon_0 \cdot \varepsilon_r \cdot \mu \cdot E_{DC}(x) \cdot \frac{\partial \varepsilon(x,t)}{\partial x} \\ j_{DISP} &= \varepsilon_0 \cdot \varepsilon_r \frac{\partial \varepsilon(x,t)}{\partial t} \end{aligned} \tag{10.30}$$

In the set of equations of (10.30), higher order terms of $\varepsilon(x, t)$ were neglected.

The Fourier transform of equation (10.29) can be solved for $\varepsilon(x, \omega)$ by using the solutions of $E_{DC}(x)$ and $\rho_{DC}(x)$ of the corresponding DC problem (ω – circular frequency of AC voltage). Integration of the electric field from anode to cathode yields then the voltage $v_{AC}(\omega)$. The impedance Z is then obtained as ratio between v_{AC} and the current density j times the surface A of the

electrodes:

$$Z(\Omega) = \frac{\tau_{DC}}{C_{geo}} \cdot \frac{1}{\Omega^3} \cdot \left[\frac{9}{8} \cdot i \cdot \tilde{\mu}^2(\Omega) \cdot \left\{ 1 - e^{-\frac{4}{3} \cdot i \cdot \frac{\Omega}{\tilde{\mu}(\Omega)}} \right\} + \frac{3}{2} \cdot \tilde{\mu}(\Omega) \cdot \Omega - i \cdot \Omega^2 \right] \quad (10.31)$$

with the DC transit time τ_{DC} of the charge carriers, the geometric capacitance C_{geo} of the structure, the normalised circular frequency Ω of the AC voltage:

$$\Omega = \omega \cdot \tau_{DC} \quad (10.32)$$

and the normalised mobility $\tilde{\mu}(\Omega)$:

$$\tilde{\mu}(\Omega) = \frac{\mu(\Omega)}{\mu_{DC}} \quad (10.33)$$

10.3. Abbreviations

π	bonding molecular pi orbital
π^*	anti-bonding molecular pi orbital
σ	bonding molecular sigma orbital
σ^*	anti-bonding molecular sigma orbital
AC	alternating current
AM1.5g	global solar spectrum at 1.5 airmasses
ASTM	American Society for Testing and Materials
ASTM E892	ASTM standard for AM1.5g spectrum
C_{60}	Buckminster fullerene
	fullerene derivative
C_{60}-2	fullerene derivative (chem. structure see figure 7.10 on p. 125)
C_{60}-4	fullerene derivative (chem. structure see figure 7.10 on p. 125)
C_{60}-5	fullerene derivative (chem. structure see figure 7.10 on p. 125)
CDM	correlated disorder model
D	drain electrode of a FET
DC	direct current
diPEO-PPV	poly[2,5-bis-(triethoxymethoxy)-1-4-phenylene vinylene]
DOS	density of states
FET	field-effect transistor
FF	fill factor
G	gate electrode of a FET
GaAs	gallium arsenide

GDM	Gaußian disorder model
GPC	gel permeation chromatography
HMDS	hexamethyldisilazane
HOMO	highest occupied molecular orbital
ITO	indium tin oxide
I-V	current-voltage
LED	light-emitting diode
LiF	lithium fluoride
lin	refers to linear regime of a FET
LUMO	lowest unoccupied molecular orbital
MOSFET	metal-oxide-semiconductor FET
MPP	maximum power point
n-Si	n-doped silicon
$O(CH_2CH_2O)_3CH_3$	triethoxymethoxy side chain
$OC_{10}H_{21}$	3-7-dimethyloctyloxy side chain
OC_1C_{10}-PPV	poly[2-(3'-7'-dimethyloctyloxy)-5-methoxy-1-4-phenylene vinylene]
OC_9H_{19}	*n*-nonyloxy side chain
OCH_3	methoxy side chain
OC_nH_{2n+1}	alkyloxy side chain with n carbon atoms
OLED	organic light-emitting diode
p	atomic p orbital
PCBM	[6,6]-phenyl C_{61}-butyric acid methyl ester
PD	polydispersity
PEDOT	poly(3,4-ethylenedioxythiophene)

PEDOT:PSS	polystyrenesulfonate doped poly(3,4-ethylenedioxythiophene)
PEO	$O(CH_2CH_2O)_3CH_3$ side chain
(PEO-OC_9)-PPV	poly[2-(*n*-nonyloxy)-5-(triethoxymethoxy)-1-4-phenylene vinylene]
PEO-PPV	poly[2-methoxy-5-(triethoxymethoxy)-1,4-phenylene vinylene]
PEOs	refers to PPV derivative with at least one PEO side chain
PPV	poly(*p*-phenylene vinylene)
	poly(*p*-phenylene vinylene) derivative
PPVs	refers to PPV derivative
PSS	polystyrenesulfonate
RMS	root mean square
	root mean square surface roughness
S	source electrode of a FET
s	atomic s orbital
sat	refers to saturation regime of a FET
SCLC	space-charge limited current
SI	Le Système international d'unités
Si	silicon
SiO_2	silicon dioxide
TFT	thin film transistor
trans	refers to transfer characteristic of a FET
UV	ultraviolet
vol.	volume as in % vol.
VRH	variable range hopping
wt.	weight as in % wt.
XRD	x-ray diffraction

10.4. Nomenclature

α	$[m^2 \cdot V^{-1} \cdot s^{-1} \cdot V^{-\beta}]$	prefactor for gate voltage-dependent mobility
	[1]	dispersion parameter for normalised mobility
	$[m^{-1}]$	optical absorption coefficient
α(E)	$[m^2 \cdot V^{-1} \cdot s^{-1} \cdot V^{-\beta}]$	field-dependent mobility parameter
α(I)	$[m^2 \cdot V^{-1} \cdot s^{-1} \cdot V^{-\beta}]$	light-dependent mobility parameter
α_0	$[m^2 \cdot V^{-1} \cdot s^{-1} \cdot V^{-\beta}]$	field-independent part of mobility parameter
	$[m^2 \cdot V^{-1} \cdot s^{-1} \cdot V^{-\beta}]$	mobility parameter in darkness
α_{lin}^{trans}	$[m^2 \cdot V^{-1} \cdot s^{-1} \cdot V^{-\beta}]$	mobility parameter extracted from the transfer characteristic in the linear regime
β	[1]	exponent for gate voltage-dependent mobility
Γ	$[m^{-1}]$	inverse localisation length
Δ	[J]	zero-field activation energy
-ΔB	[S]	negative differential susceptance
ΔQ(x)	$[C \cdot m^{-2}]$	induced charge density in a FET
ε	$[F \cdot m^{-1}]$	permittivity of a material
ε(x, t)	$[V \cdot m^{-1}]$	position- and time-dependent electric field of AC voltage
ε(x, ω)	$[V \cdot m^{-1}]$	Fourier transform of ε(x, t)
ε_0	$[F \cdot m^{-1}]$	permittivity of vacuum
ε_i, ε_j, ε_n, ε_{n+1}	[J]	site energy

ε_r	[1]	relative permittivity of a material
η	[1]	solar cell efficiency
θ	[°]	diffraction angle for XRD measurements
$\vartheta(x, t)$	[m^{-3}]	AC contribution of position- and time-dependent charge carrier concentration
$\imath(t)$	[$A \cdot m^{-2}$]	AC contribution of time-dependent current density
λ_0	[m]	starting wavelength of AM1.5g spectrum
λ_{gap}	[m]	wavelength corresponding to band gap
μ	[$m^2 \cdot V^{-1} \cdot s^{-1}$]	mobility
$\mu(E)$	[$m^2 \cdot V^{-1} \cdot s^{-1}$]	field-dependent mobility
$\mu(E, T)$	[$m^2 \cdot V^{-1} \cdot s^{-1}$]	field- and temperature-dependent mobility
$\mu(L)$	[$m^2 \cdot V^{-1} \cdot s^{-1}$]	length-dependent mobility
$\mu(V_G)$	[$m^2 \cdot V^{-1} \cdot s^{-1}$]	gate voltage-dependent mobility
$\mu(x)$	[$m^2 \cdot V^{-1} \cdot s^{-1}$]	position-dependent mobility
μ_0	[$m^2 \cdot V^{-1} \cdot s^{-1}$]	zero-field mobility
	[$m^2 \cdot V^{-1} \cdot s^{-1}$]	trap-free mobility
	[$m^2 \cdot V^{-1} \cdot s^{-1}$]	mobility corrected for series resistance
μ_{00}	[$m^2 \cdot V^{-1} \cdot s^{-1}$]	trap-free zero-field mobility
μ_∞	[$m^2 \cdot V^{-1} \cdot s^{-1}$]	zero-field mobility in infinite temperature limit
μ_{DC}	[$m^2 \cdot V^{-1} \cdot s^{-1}$]	mobility in the DC case
μ_{FET}	[$m^2 \cdot V^{-1} \cdot s^{-1}$]	FET mobility

μ_{IMP}	$[m^2 \cdot V^{-1} \cdot s^{-1}]$	mobility extracted from impedance spectroscopy
μ_{SCLC}	$[m^2 \cdot V^{-1} \cdot s^{-1}]$	SCLC mobility
$\mu_{lin}^{g_m}$	$[m^2 \cdot V^{-1} \cdot s^{-1}]$	mobility extracted from transconductance in linear regime
$\mu_{lin}^{g_d}$	$[m^2 \cdot V^{-1} \cdot s^{-1}]$	mobility extracted from conductance in linear regime
μ_{sat}^{trans}	$[m^2 \cdot V^{-1} \cdot s^{-1}]$	mobility extracted from transfer characteristic in saturation regime
$\tilde{\mu}$, $\tilde{\mu}$ (Ω)	[1]	normalised mobility
ν, ν_0	[Hz]	hopping rate
ν_{max}	[Hz]	frequency at maximum of -ΔB
Ξ	[1]	function describing degree of positional disorder
ρ	[Ω·m]	resistivity of a material
	$[C \cdot m^{-3}]$	charge density
	$[m^{-3}]$	charge carrier concentration
ρ(x, t)	$[m^{-3}]$	position- and time-dependent charge carrier concentration
$\rho_{DC}(x)$	$[m^{-3}]$	DC contribution of position-dependent charge carrier concentration
σ	[J]	width of density of states
	$[S \cdot m^{-1}]$	conductivity of a material
σ(x, y)	$[S \cdot m^{-1}]$	position-dependent conductivity
Σ	[1]	degree of positional disorder
τ_{DC}	[s]	DC transit time
τ_{max}	[s]	reciprocal value of ν_{max}

ω	$[s^{-1}]$	circular frequency of AC voltage
ω_{max}	$[s^{-1}]$	circular frequency of AC voltage at maximum of Nyquist plot
Ω	[1]	normalised circular frequency of AC voltage

a	[m]	average site spacing
A	$[m^2]$	surface area of capacitor
	[1]	absorption
B	$[J \cdot m^{1/2} \cdot V^{-1/2}]$	characteristic parameter describing temperature dependence of mobility
	[S]	susceptance
B(ω)	[S]	circular frequency-dependent susceptance
B’	[S]	susceptance corrected for series resistance
c	$[m^{1/2} \cdot V^{-1/2}]$	constant depending on site spacing
c_i	$[F \cdot m^2]$	capacitance per area of silicon oxide
C	[F]	capacitance
C(ω)	[F]	circular frequency-dependent capacitance
C_{geo}	[F]	geometric capacitance
C_{ref}	[F]	reference capacitance
d	[m]	film thickness film
	[m]	spacing between “crystal” planes

$d(x)$	[m]	position-dependent thickness of accumulation layer in a FET
d_i	[m]	thickness of silicon dioxide in a FET
E	[$V \cdot m^{-1}$]	electric field
$E(x)$	[$V \cdot m^{-1}$]	position-dependent electric field
$E(x, t)$	[$V \cdot m^{-1}$]	position- and time-dependent electric field
E_0	[$V \cdot m^{-1}$]	characteristic electric field describing field dependence of mobility
E_A^{LUMO}	[J]	energy of LUMO of acceptor material
E_{blend}	[J]	effective band gap of blend
E_C	[$V \cdot m^{-1}$]	electric field at collecting electrode
E_D^{HOMO}	[J]	energy of HOMO of donor material
$E_{DC}(x)$	[$V \cdot m^{-1}$]	DC contribution of position-dependent electric field
E_{gap}	[J]	band gap
$E_x(x)$	[$V \cdot m^{-1}$]	x-component of position-dependent electric field
$EQE(\lambda)$	[1]	external quantum efficiency
FF	[1]	fill factor of solar cell
g_d	[S]	conductance of a FET
g_m	[S]	transconductance of a FET
G	[S]	conductance (real part of Y)
i	[1]	imaginary unit ($i^2 = -1$)
	[1]	index

I	[lx]	illuminance
$I(d)$	[$W \cdot m^{-2}$]	depth-dependent intensity
I_0	[lx]	characteristic illuminance
	[$W \cdot m^{-2}$]	initial intensity
I_{MPP}	[A]	current at maximum power point
I_{ph}	[A]	photo current
I_{SC}	[A]	short circuit current
I_{SD}	[A]	source-drain current
$I_{SD}(x)$	[A]	position-dependent source-drain current
j	[$A \cdot m^{-2}$]	current density
	[1]	index
$j(t)$	[$A \cdot m^{-2}$]	time-dependent current density
j_{AC}	[$A \cdot m^{-2}$]	current density due to AC voltage
$j_{AC\square DC}$	[$A \cdot m^{-2}$]	additional DC current density due to AC voltage
j_{DC}	[$A \cdot m^{-2}$]	DC current density
j_{DISP}	[$A \cdot m^{-2}$]	current density due to relaxation of displacement charges
j_{MPP}	[$A \cdot m^{-2}$]	current density at maximum power point
j_{SC}	[$A \cdot m^{-2}$]	short circuit current density
$j_{SD}(x)$, $j_{SD}(x, y, z)$	[$A \cdot m^{-2}$]	position-dependent source-drain current density
k_B	[$J \cdot K^{-1}$]	Boltzmann constant
L	[m]	channel length of FET
M	[1]	dispersion parameter for normalised mobility

M_N	[kg·mol^{-1}]	numeric average molecular mass
M_W	[kg·mol^{-1}]	weight average molecular mass
n	[1]	index
n(x)	[m^{-3}]	total charge carrier concentration
n_0(x)	[m^{-3}]	concentration of free charge carriers
n_T(x)	[m^{-3}]	trap concentration
N_C	[m^{-2}]	effective DOS at band edge
N_T	[m^{-2}]	trap concentration
p, p(x, y)	[m^{-3}]	hole concentration
P	[m^3·mol^{-1}]	molar dielectric polarisation
P_i	[m^3·mol^{-1}]	group contribution to molar dielectric polarisation
P_{in}	[W]	incident optical power of a solar cell
P_{out}	[W]	electrical output power of solar cell
q	[C]	elementary charge
Q(x)	[C·m^{-2}]	total charge density in a FET
Q_0(x)	[C·m^{-2}]	intrinsic charge density in a FET
r, $r_{g_d}^{calc}$, $r_{g_d}^{fit}$, r_{sat}^{fit}	[1]	ratio of series resistance and sheet resistance
r_{ij}	[m]	spatial distance between site i and j
R	[1]	optical reflection
	[Ω]	resistance
R_{CH}	[Ω]	channel resistance
R_{DRN}	[Ω]	series resistance at the drain side
R_P	[Ω]	parallel resistance

R_S	[Ω]	series resistance
R_{SH}	[Ω]	shunt resistance
R_{SHEET}	[Ω]	sheet resistance
R_{SRC}	[Ω]	series resistance at the source side
R_{TOT}	[Ω]	total resistance of device
RMS	[m]	root mean square surface roughness
S(λ)	[$m^{-3} \cdot s^{-1}$]	solar spectrum
t	[m]	film thickness
T	[K]	absolute temperature
	[1]	optical transmission
T_0	[K]	characteristic parameter describing temperature dependence of mobility
T_C	[K]	critical temperature describing gate voltage-dependent mobility
v_{AC}, $v_{AC}(\omega)$	[V]	AC voltage in impedance spectroscopy
V, V(x)	[V]	voltage
	[$m^3 \cdot mol^{-1}$]	total amorphous molar volume
V_0	[V]	trap-dependent voltage for gate voltage-dependent mobility
	[V]	offset voltage for SCLC
V_G	[V]	gate voltage
V_i	[$m^3 \cdot mol^{-1}$]	group contribution to amorphous molar volume
V_{MPP}	[V]	voltage at maximum power point
V_{OC}	[V]	open circuit voltage
V_{SD}	[V]	source-drain voltage

V_T	[V]	threshold voltage
W	[m]	channel width of FET
W_{ij}, $W_{n+1,n}$	[s^{-1}]	transition rate for hopping process
x	[m]	x-coordinate
y	[m]	y-coordinate
Y	[S]	admittance
z	[m]	z-coordinate
Z, Z(Ω)	[Ω]	impedance

11. Publications and Conference Contributions

11.1. Publications

Breban, L., Breselge, M., Lutsen, L., Manca, J., Cleij, T. J. and Vanderzande, D., Correlation Between the Molecular Structure and the Charge Carrier Mobility in Poly(Arylene Vinylene) Derivatives, Abstracts of Papers of the American Chemical Society, 2006 Mar 26; 231

Breselge, M., Van Severen, I., Lutsen, L., Adriaensens, P., Manca, J., Vanderzande, D. and Cleij, T., Comparison of the electrical characteristics of four 2,5-substituted poly(p-phenylene vinylene) derivatives with different side chains, Thin Solid Films, 2006 Jul 26, 511-512, 328

Douhéret, O., Lutsen, L., Swinnen, A., Breselge, M.; Vandewal, K., Goris, L. and Manca, J., Nanoscale electrical characterization of organic photovoltaic blends by conductive atomic force microscopy, Applied Physics Letters, 2006 Jul 17, 89, (3): 032107-3

Douhéret, O., Swinnen, A., Breselge, M., Van Severen, I., Lutsen, L., Vanderzande, D. and Manca, J., High Resolution Electrical Characterisation of Organic Photovoltaic Blends, Microelectronic Engineering, 2007 Mar, 84, (3): 431

Van Severen, I., Breselge, M., Fourier, S., Adriaensens, P., Manca, J., Lutsen, L., Cleij, T. J. and Vanderzande, D., 2,5-Substituted PPV-Derivatives with Different Polarities: The Effect of Side Chain Polarity on Solubility, Optical and Electronic Properties, Macromolecular Chemistry and Physics, 2007, 208, (2): 196

Breselge, M., Aguirre, A., Janssen, G., Douhéret, O., Lutsen, L., Vanderzande, D., Manca, J., Wagner, P. and Goovaerts, E., Effect of Polarity Tuning of 2,5-Substituted Poly(*p*-Phenylene Vinylene) Derivatives and Their Blends with PCBM on Electro-Optical, Morphological and Photovoltaic Properties, Advanced Functional Materials, 2007, submitted

11.2. Conference Contributions

Breselge, M., van Severen, I., Lutsen, L., Adriaensens, P., Manca, J., Vanderzande, D, Cleij, T., Comparison of the Electrical Characteristics of Four 2,5-Substituted Poly(P-Phenylene Vinylene) Derivatives with Different Side Chains, poster presentation, symposium F, E-MRS Spring Meeting 2005, Strasbourg (France)

Breban, L., Lutsen, L., Breselge, M., D'Haen, J., Vanhoyland, G., Manca, J., Vanderzande, D., Adriaensens, P., Thermally Induced Order in PPV-Derivatives, poster presentation, symposium F, E-MRS Spring Meeting 2005, Strasbourg (France)

Banishoeib, F., Breselge, M., Manca, J., Cleij, T., Lutsen, L., Vanderzande, D., Synthesis of low band gap poly(p-thienylenvinylene), PTV, via a soluble precursor route: the dithiocarbamate precursor route, poster presentation, European Conference on Hybrid and Organic Solar Cells ECHOS'2006, Paris (France)

12. References

[1] Pope, M., Kallmann, H. P. and Magnante, P., The Journal of Chemical Physics, vol. 38, no. 8 (1963) p. 2042

[2] Le Blanc, Jr. O. H., The Journal of Chemical Physics, vol. 33, no. 2 (1960) p. 626

[3] Kepler, R. G., Physical Review, vol. 119, no. 4 (1960) p. 1226

[4] Mette, H. and Pick, H., Zeitschrift für Physik A - Hadrons and Nuclei, vol. 134, no. 5 (1953) p. 566

[5] Chiang, C. K., Fincher, C. R., Park, Y. W., Heeger, A. J., Shirakawa, H., Louis, E. J., Gau, S. C. and MacDiarmid, A. G., Physical Review Letters, vol. 39, no. 17 (1977) p. 1098

[6] Burroughes, J. H., Bradley, D. D. C., Brown, A. R., Marks, R. N., Mackay, K., Friend, R. H., Burns, P. L. and Holmes, A. B., Nature, vol. 347, no. 6293 (1990) p. 539

[7] Klauk, H., Schmid, G., Radlik, W., Weber, W., Zhou, L., Sheraw, C. D., Nichols, J. A. and Jackson, T. N., Solid-State Electronics, vol. 47, no. 2 (2003) p. 297

[8] Aleshin, A. N., Sandberg, H. and Stubb, H., Synthetic Metals, vol. 121, no. 1-3 (2001) p. 1449

[9] Knipp, D., Street, R. A., Völkel, A. and Ho, J., Journal of Applied Physics, vol. 93, no. 1 (2003) p. 347

[10] Chua, L.-L., Zaumseil, J., Chang, J.-F., Ou, E. C. W., Ho, P. K. H., Sirringhaus, H. and Friend, R. H., Letters to Nature, vol. 434, no. 7030 (2005) p. 194

[11] Dimitrakopoulos, C. D. and Malenfant, P. R. L., Advanced Materials, vol. 14, no. 2 (2002) p. 99

[12] Dimitrakopoulos, C. D. and Mascaro, D. J., IBM Journal of Research & Development, vol. 45, no. 1 (2001) p. 11

[13] Paasch, G., Scheinert, S. and Tecklenburg, R., European Solid-State Device Research Conference, 2004

[14] Schmechel, R., Ahles, M. and von Seggern, H., Journal of Applied Physics, vol. 98, no. 8 (2005) p. 084511

[15] Bürgi, L., Richards, T. J., Friend, R. H. and Sirringhaus, H., Journal of Applied Physics, vol. 94, no. 9 (2003) p. 6129

[16] Bürgi, L., Friend, R. H. and Sirringhaus, H., Applied Physics Letters, vol. 82, no. 9 (2003) p. 1482

[17] Meijer, E. J., Gelinck, G. H., van Veenendaal, E., Huisman, B.-H., de Leeuw, D. M. and Klapwijk, T. M., Applied Physics Letters, vol. 82, no. 25 (2003) p. 4576

[18] Street, R. A. and Salleo, A., Applied Physics Letters, vol. 81, no. 15 (2002) p. 2887

[19] Zaumseil, J., Baldwin, K. W. and Rogers, J. A., Journal of Applied Physics, vol. 93, no. 10 (2003) p. 6117

[20] Brown, A. R., Jarrett, C. P., de Leeuw, D. M. and Matters, M., Synthetic Metals, vol. 88, no. 1 (1997) p. 37

[21] Horowitz, G., Hajlaoui, R. and Delannoy, P., Journal de Physique III, vol. 5 (1995) p. 355

[22] Vissenberg, M. C. J. M. and Matters, M., Physical Review B, vol. 57, no. 20 (1998) p. 12964

[23] Fuchigami, H., Tsumura, A. and Koezuka, H., Applied Physics Letters, vol. 63, no. 10 (1993) p. 1372

[24] Nagamatsu, S., Tanigaki, N., Yoshida, Y., Takashima, W., Yase, K. and Kaneto, K., Synthetic Metals, vol. 137, no. 1-3 (2003) p. 923

[25] Geens, W., Tsamouras, D., Poortmans, J. and Hadziioannou, G., Synthetic Metals, vol. 122, no. 1 (2001) p. 191

[26] Porzio, W., Destri, S., Pasini, M., Bolognesi, A., Angiulli, A., Di Gianvincenzo, P., Natali, D., Sampietro, M., Caironi, M., Fumagalli, L., Ferrari, S., Peron, E. and Perissinotti, F., Materials Science and Engineering: C, vol. 26, no. 5-7 (2006) p. 996

[27] Salleo, A. and Street, R. A., Journal of Applied Physics, vol. 94, no. 1 (2003) p. 471

[28] Zilker, S. J., Detcheverry, C., Cantatore, E. and de Leeuw, D. M., Applied Physics Letters, vol. 79, no. 8 (2001) p. 1124

[29] Meijer, E. J., De Leeuw, D. M., Setayesh, S., Veenendaal, E. Van, Huisman, B. H., Blom, P. W. M., Hummelen, J. C., Scherf, U. and Klapwijk, T. M., Nature Materials, vol. 2, no. 10 (2003) p. 678

[30] Dimitrakopoulos, C. D., Brown, A. R. and Pomp, A., Journal of Applied Physics, vol. 80, no. 4 (1996) p. 2501

[31] Sirringhaus, H. , Brown, P. J., Friend, R. H., Nielsen, M. M., Bechgaard, K., Langeveld-Voss, B. M. W., Spiering, A. J. H., Janssen, R. A. J., Meijer, E. W., Herwig, P. and de Leeuw, D. M., Nature, vol. 401, no. 6754 (1999) p. 685

[32] Brown, A. R., Pomp, A., Hart, C. M. and de Leeuw, D. M., Science, vol. 270, no. 5238 (1995) p. 972

[33] Koezuka, H., Tsumura, A. and Ando, T., Synthetic Metals, vol. 18, no. 1-3 (1987) p. 699

[34] Martens, H. C. F., Huiberts, J. N. and Blom, P. W. M., Applied Physics Letters, vol. 77, no. 12 (2000) p. 1852

[35] Ding, X. M., Hung, L. M., Cheng, L. F., Deng, Z. B., Hou, X. Y., Lee, C. S. and Lee, S. T., Applied Physics Letters, vol. 76, no. 19 (2000) p. 2704

[36] Marai, F., Romdhane, S., Hassine, L., Majdoub, M. and Bouchriha, H., Synthetic Metals, vol. 132, no. 2 (2003) p. 117

[37] Blom, P. W. M., de Jong, M. J. M. and Breedijk, S., Applied Physics Letters, vol. 71, no. 7 (1997) p. 930

[38] Parker, I. D., Journal of Applied Physics, vol. 75, no. 3 (1994) p. 1656

[39] Scott, J. C., Kaufman, J. H., Brock, P. J., DiPietro, R., Salem, J. and Goitia, J. A., Journal of Applied Physics, vol. 79, no. 5 (1996) p. 2745

[40] Kim, J. S., Granström, M., Friend, R. H., Johansson, N., Salaneck, W. R., Daik, R., Feast, W. J. and Cacialli, F., Journal of Applied Physics, vol. 84, no. 12 (1998) p. 6859

[41] Karg, S., Scott, J. C., Salem, J. R. and Angdopoulos, M., Synthetic Metals, vol. 80, no. 2 (1996) p. 111

[42] Brabec, C. J., Winder, C., Sariciftci, N. S., Hummelen, J. C., Dhanabalan, A., van Hal, P. A. and Janssen, R. A. J., Advanced Functional Materials, vol. 12, no. 10 (2002) p. 709

[43] Blom, P. W. M. and Vissenberg, M. C. J. M., Materials Science and Engineering: R: Reports, vol. 27, no. 3-4 (2000) p. 53

[44] Burrows, P. E., Shen, Z., Bulovic, V., McCarty, D. M., Forrest, S. R., Cronin, J. A. and Thompson, M. E., Journal of Applied Physics, vol. 79, no. 10 (1996) p. 7991

[45] Paasch, G., Riess, W., Karg, S., Meier, M. and Schwoerer, M., Synthetic Metals, vol. 67, no. 1-3 (1994) p. 177

[46] Vissenberg, M. C. J. M. and Blom, P. W. M., Synthetic Metals, vol. 102, no. 1-3 (1999) p. 1053

[47] Campbell, I. H. , Smith, D. L. and Ferraris, J. P., Applied Physics Letters, vol. 66, no. 22 (1995) p. 3030

[48] Meier, M., Karg, S. and Riess, W., Journal of Applied Physics, vol. 82, no. 4 (1997) p. 1961

[49] Li, Y., Gao, J., Yu, G., Cao, Y. and Heeger, A. J., Chemical Physics Letters, vol. 287, no. 1-2 (1998) p. 83

[50] Bisquert, J., Garcia-Belmonte, G., Pitarch, A. and Bolink, H. J., Chemical Physics Letters, vol. 422, no. 1-3 (2006) p. 184

[51] Elschner, A., Bruder, F., Heuer, H. W., Jonas, F., Karbach, A., Kirchmeyer, S., Thurm, S. and Wehrmann, R., Synthetic Metals, vol. 111 (2000) p. 139

[52] Martens, H. C. F., Pasveer, W. F., Brom, H. B., Huiberts, J. N. and Blom, P. W. M., Physical Review B, vol. 63, no. 12 (2001) p. 125328

[53] Pacios, R., Bradley, D. D. C., Nelson, J. and Brabec, C. J., Synthetic Metals, vol. 137, no. 1-3 (2003) p. 1469

[54] Melzer, C., Koop, E. J., Mihailetchi, V. D. and Blom P. W. M., Advanced Functional Materials, vol. 14, no. 9 (2004) p. 865

[55] Niggemann, M., Bläsi, B., Gombert, A., Hinsch, A., Hoppe, H., Lalanne, P., Meissner, D. and Wittwer, V., 17th EU-PVSEC (2001) p. 284

[56] Goris, L., Loi, M. A., Cravino, A., Neugebauer, H., Sariciftci, N. S., Polec, I., Lutsen, L., Andries, E., Manca, J. , De Schepper, L. and Vanderzande, D., Synthetic Metals, vol. 138, no. 1-2 (2003) p. 249

[57] Chirvase, D., Chiguvare, Z., Knipper, M., Parisi, J., Dyakonov, V. and Hummelen, J. C., Synthetic Metals, vol. 138, no. 1-2 (2003) p. 299

[58] Gebeyehu, D., Maennig, B., Drechsel, J., Leo, K. and Pfeiffer, M., Solar Energy Materials & Solar Cells, vol. 79, no. 1 (2003) p. 81

[59] Geens, W., Aernouts, T., Poortmans, J. and Hadziioannou, G., Thin Solid Films, vol. 403-404 (2002) p. 438

[60] Nelson, J., Current Opinion in Solid State & Materials Science, vol. 6, no. 1 (2002) p. 87

[61] Meissner, D., Sariciftci, N. S. and Hoppe, H., Molecular Crystals & Liquid Crystals, vol. 385 (2002) p. 113

[62] Munters, T., Martens, T., Goris, L., Vrindts, V., Manca, J., Lutsen, L., De Ceuninck, W., Vanderzande, D., De Schepper, L., Gelan, J., Sariciftci, N. S. and Brabec, J. C., Thin Solid Films, vol. 403-404 (2002) p. 247

[63] Hoppe, H., Glatzel, T., Niggemann, M., Schwinger, W., Schaeffler, F., Hinsch, A., Lux-Steiner, M. C. and Sariciftci, N. S., Thin Solid Films, vol. 511 (2006) p. 587

[64] Chirvase, D., Chiguvare, Z., Knipper, M., Parisi, J., Dyakonov, V. and Hummelen, J. C., Journal of Applied Physics, vol. 93, no. 6 (2003) p. 3376

[65] Jeranko, T., Tributsch, H., Sariciftci, N. S. and Hummelen, J. C., Solar Energy Materials and Solar Cells, vol. 83, no. 2-3 (2004) p. 247

[66] Aernouts, T., Geens, W., Poortmans, J., Heremans, P., Borghs, S. and Mertens, R., Thin Solid Films, vol. 403-404 (2002) p. 297

[67] Kaydanova, T., Miedaner, A., Curtis, C., Perkins, J., Alleman, J. and Ginley, D., NCPV and Solar Program Review Meeting (2003) p. 919

[68] Schilinsky, P., Waldauf, C. and Brabec, C. J., Applied Physics Letters, vol. 81, no. 20 (2002) p. 3885

[69] Shaheen, S. E., Brabec, C. J., Sariciftci, N. S., Padinger, F., Fromherz, T. and Hummelen, J. C., Applied Physics Letters, vol. 78, no. 6 (2001) p. 841

[70] Yu, G., Pakbaz, K. and Heeger, A. J., Applied Physics Letters, vol. 64, no. 25 (1994) p. 3422

[71] Eastman Kodak Company: http://www.kodak.com

[72] Philips: http://www.philips.com

[73] Samsung: http://www.samsungsdi.com

[74] Sony: http://www.sony.net/

[75] Dimitrakopoulos, C. D., Furman, B. K., Graham, T., Hegde, S. and Purushothaman, S., Synthetic Metals, vol. 92, no. 1 (1998) p. 47

[76] Thin Film Manufacturing: http://www.thinfilmmfg.com

[77] IDTechEX: http://www.idtechex.com

[78] Lebedev, E., Dittrich, Th., Petrova-Koch, V., Karg, S. and Brütting, W., Applied Physics Letters, vol. 71, no. 18 (1997) p. 2686

[79] Campbell, I. H. , Smith, D. L., Neef, C. J. and Ferraris, J. P., Applied Physics Letters, vol. 74, no. 19 (1999) p. 2809

[80] Karl, N., Marktanner, J., Stehle, R. and Warta, W., Synthetic Metals, vol. 42, no. 3 (1991) p. 2473

[81] Horowitz, G., Hajlaoui, R., Fichou, D. and El Kassmi, A., Journal of Applied Physics, vol. 85, no. 6 (1999) p. 3202

[82] Horowitz, G., Hajlaoui, R., Bourguiga, R. and Hajlaoui, M., Synthetic Metals, vol. 101, no. 1-3 (1999) p. 401

[83] Horowitz, G., Lang, P., Mottaghi, M. and Aubin, H., Advanced Functional Materials, vol. 14, no. 11 (2004) p. 1069

[84] Brown, A. R., de Leeuw, D. M., Havinga, E. E. and Pomp, A., Synthetic Metals, vol. 68, no. 1 (1994) p. 65

[85] Bürgi, L., Richards, T., Chiesa, M., Friend, R. H. and Sirringhaus, H., Synthetic Metals, vol. 146, no. 3 (2004) p. 297

[86] Necliudov, Peter V., Shur, Michael S., Gundlach, David J. and Jackson, Thomas N., Solid-State Electronics, vol. 47, no. 2 (2003) p. 259

[87] Horowitz, G. and Delannoy, P., Journal of Applied Physics, vol. 70, no. 1 (1991) p. 469

[88] Peng, X., Horowitz, G., Fichou, D. and Garnier, F., Applied Physics Letters, vol. 57, no. 19 (1990) p. 2013

[89] Dodabalapur, A., Torsi, L. and Katz, H. E., Science, vol. 268, no. 5208 (1995) p. 270

[90] Katz, O., Roichman, Y., Bahir, G., Tessler, N. and Salzman, J., Semiconductor Science and Technology, vol. 20, no. 1 (2005) p. 90

[91] Podzorov, V., Menard, E., Rogers, J. A. and Gershenson, M. E., Physical Review Letters, vol. 95, no. 22 (2005) p. 226601-4

[92] Takamatsu, Y., Sekitani, T. and Someya, T., Applied Physics Letters, vol. 90, no. 13 (2007) p. 133516-3

[93] Fessenden, R. J. and Fessenden, J. S., Organic Chemistry 2 edition, W. Grant Press (1982) 0-87150-752-8

[94] Tremel, W., Seshadri, R. and Finckh, E. W., Chemie in unserer Zeit, vol. 35, no. 1 (2001) p. 42

[95] Breselge, M., Van Severen, I., Lutsen, L., Adriaensens, P., Manca, J., Vanderzande, D. and Cleij, T., Thin Solid Films, vol. 511-512 (2006) p. 328

[96] Van Severen, I., thesis at the Transnationale Universiteit Limburg 2006

[97] Prins, P., Grozema, F. C., Schins, J. M., Savenije, T. J., Patil, S., Scherf, U. and Siebbeles, L. D. A., Physical Review B, vol. 73, no. 4 (2006) p. 045204-10

[98] Gill, W. D., Journal of Applied Physics, vol. 43, no. 12 (1972) p. 5033

[99] Conwell, E. M., Physical Review, vol. 103, no. 1 (1956) p. 51

[100] Mott, N. F., Canadian Journal of Physics, vol. 34, no. 12A (1956) p. 1356

[101] Miller, A. and Abrahams, E., Physical Review, vol. 120, no. 3 (1960) p. 745

[102] Mott, N. F., Journal of Non-Crystalline Solids, vol. 1, no. 1 (1968) p. 1

[103] Bässler, H., Physica Status Solidi B, vol. 175, no. 1 (1993) p. 15

[104] Dunlap, D. H., Parris, P. E. and Kenkre, V. M., Physcial Review Letters, vol. 77, no. 3 (1996) p. 542

[105] Glauber, R. J., Journal of Mathematical Physics, vol. 4, no. 2 (1963) p. 294

[106] Novikov, S. V. , Dunlap, D. H. and Kenkre, V. M, Proceedings of SPIE, vol. 3471 (1998) p. 181

[107] Hamadani, B. H. and Natelson, D., Journal of Applied Physics, vol. 95, no. 3 (2004) p. 1227

[108] Brütting, W., Berleb, S. and Mückl, A. G., Organic Electronics, vol. 2, no. 1 (2001) p. 1

[109] Martens, H. C. F., Brom, H. B., Blom, P. W. M. and Schoo, H. F. M., Physica Status Solidi (b), vol. 218, no. 1 (2000) p. 283

[110] Shur, M., Hack, M. and Shaw, J. G., Journal of Applied Physics, vol. 66, no. 7 (1989) p. 3371

[111] Horowitz, G., Hajlaoui, M. E. and Hajlaoui, R., Journal of Applied Physics, vol. 87, no. 9 (2000) p. 4456

[112] Geens, W., Shaheen, S. E., Wessling, B., Brabec, C. J., Poortmans, J. and Sariciftci, S. N., Organic Electronics, vol. 3, no. 3-4 (2002) p. 105

[113] Ono, S., Wasa, K. and Hayakawa, S., Wave Electron, vol. 3, no. 1 (1977) p. 35

[114] Blanchet, G. B., Fincher, C. R., Lefenfeld, M. and Rogers, J. A., Applied Physics Letters, vol. 84, no. 2 (2004) p. 296

[115] Hamilton, M. C., Martin, S. and Kanicki, J., Materials Research Society Symposium Proceedings, vol. 771 (2003) p. 333

[116] Scott, J. C. and Malliaras, G. G., Chemical Physics Letters, vol. 299, no. 2 (1999) p. 115

[117] Natali, D., Fumagalli, L. and Sampietro, M., Journal of Applied Physics, vol. 101, no. 1 (2007) p. 014501-12

[118] Bürgi, L., Sirringhaus, H. and Friend, R. H., Applied Physics Letters, vol. 80, no. 16 (2002) p. 2913-2915

[119] Bässler, H., Advanced Materials, vol. 5, no. 9 (1993) p. 662

[120] Hulea, I. N., Brom, H. B., Brunner, K., Scheer, R. F. J. v. d. and Michels, M. A. J., Synthetic Metals, vol. 135-136 (2003) p. 5

[121] Blom, P. W. M. , de Jong, M. J. M. and Vleggaar, J. J. M., Applied Physics Letters, vol. 68, no. 23 (1996) p. 3308

[122] Natali, D. and Sampietro, M., Journal of Applied Physics, vol. 92, no. 9 (2002) p. 5310

[123] Tsang, S. W., So, S. K. and Xu, J. B., Journal of Applied Physics, vol. 99, no. 1 (2006) p. 013706-7

[124] Martens, H. C. F., Brom, H. B. and Blom, P. W. M., Physical Review B, vol. 60, no. 12 (1999) p. R8489

[125] Blythe, A. R., Electrical Properties of Polymers Cambridge University Press (1979) 0-521-21902-7

[126] van Krevelen, D. W., Properties of Polymers: Their Correlation with Chemical Structure; Their Numerical Estimation and Prediction from Additive Group Contributions 3 edition, Elsevier (1994) 0-444-88160-3

[127] Winder, C. and Sariciftci, N. S., Journal of Materials Chemistry, vol. 14, (2004) p. 1077

[128] Roncali, J., Chemical Reviews, vol. 97, no. 1 (1997) p. 173

[129] Novikov, S. V. , Dunlap, D. H., Kenkre, V. M., Parris, P. E. and Vannikov, A. V., Physical Review Letters, vol. 81, no. 20 (1998) p. 4472

[130] Martens, H. C. F., Blom, P. W. M. and Schoo, H. F. M., Physical Review B, vol. 61, no. 11 (2000) p. 7489

[131] Senes, A., thesis at the University of Cagliari, Dipartimento di Ingegneria Elettrica ed Elettronica 2006

[132] van Breemen, A. J. J. M., Herwig, P. T., Chlon, C. H. T., Sweelssen, J., Schoo, H. F. M., Benito, E. M., de Leeuw, D. M., Tanase, C., Wildeman, J. and Blom, P. W. M., Advanced Functional Materials, vol. 15, no. 5 (2005) p. 872

[133] Martens, T., Munters, T., Goris, L., D'Haen, J., Schouteden, K., D'Olieslaeger, M., Lutsen, L., Vanderzande, D., Geens, W., Poortmans, J., De Schepper, L. and Manca, J. V., Applied Physics A: Materials Science & Processing, vol. 79, no. 1 (2004) p. 27

[134] Riddick, J. A. , Bunger, W. B., and Sakano, T. K., Organic Solvents: Physical Properties and Methods of Purification 4 edition, John Wiley & Sons Inc. (1986) 0-471-08467-0

[135] Becquerel, A.-E., Comptes rendus hebdomadaires des séances de l'Académie des Sciences, vol. 9, no. 1 (1839) p. 561

[136] Einstein, A., Annalen der Physik, vol. 14, no. S1 (1905) p. 164

[137] Fahrenbruch, A. L. and Bube, R. H., Fundamentals of Solar Cells: Photovoltaic Solar Energy Conversion Academic Press Inc. (1983) 0-12-247680-8

[138] Offermans, T., Meskers, S. C. J. and Janssen, R. A. J., Chemical Physics, vol. 308, no. 1-2 (2005) p. 125

[139] Arkhipov, V. I., Heremans, P. and Bässler, H., Applied Physics Letters, vol. 82, no. 25 (2003) p. 4605

[140] Sylvester-Hvid, K. O. and Ratner, M. A., Journal of Physical Chemistry B, vol. 109, no. 1 (2005) p. 200

[141] Peumans, P. and Forrest, S. R., Chemical Physics Letters, vol. 398, no. 1-3 (2004) p. 27

[142] van der Horst, J. W., Bobbert, P. A., Pasveer, W. F., Michels, M. A. J., Brocks, G. and Kelly, P. J., Computer Physics Communications, vol. 147, no. 1-2 (2002) p. 331

[143] Moses, D., Wang, J., Heeger, A. J., Kirova, N. and Brazovski, S., Proceedings of the National Academy of Sciences of the United States of America, vol. 98, no. 24 (2001) p. 13496

[144] Bittner, E. R. , Ramon, J. G. S. and Karabunarliev, S., The Journal of Chemical Physics, vol. 122, no. 21 (2005) p. 214719

[145] Arkhipov, V. I., Emelianova, E. V. and Bässler, H., Physical Review Letters, vol. 82, no. 6 (1999) p. 1321

[146] Halls, J. J. M., Pichler, K., Friend, R. H., Moratti, S. C. and Holmes, A. B., Applied Physics Letters, vol. 68, no. 22 (1996) p. 3120

[147] Stübinger, T. and Brütting, W., Journal of Applied Physics, vol. 90, no. 7 (2001) p. 3632

[148] Brabec, C. J., Solar Energy Materials & Solar Cells, vol. 83, no. 2-3 (2004) p. 273

[149] Brabec, C. J., Sariciftci, N. S. and Hummelen, J. C., Advanced Functional Materials, vol. 11, no. 1 (2001) p. 15

[150] Wu, C. C., Wu, C. I., Sturm, J. C. and Kahn, A., Applied Physics Letters, vol. 70, no. 11 (1997) p. 1348

[151] Milliron, D. J., Hill, I. G., Shen, C., Kahn, A. and Schwartz, J., Journal of Applied Physics, vol. 87, no. 1 (2000) p. 572

[152] Sugiyama, K., Ishii, H., Ouchi, Y. and Seki, K., Journal of Applied Physics, vol. 87, no. 1 (2000) p. 295

[153] Nüesch, F., Forsythe, E. W., Le, Q. T., Gao, Y. and Rothberg, L. J., Journal of Applied Physics, vol. 87, no. 11 (2000) p. 7973

[154] Lee, K. H., Jang, H. W., Kim, K.-B., Tak, Y.-H. and Lee, J.-L., Journal of Applied Physics, vol. 95, no. 2 (2004) p. 586

[155] Nardes, A. M., Kemerink, M., Janssen, R. A. J., Bastiaansen, J. A. M., Kiggen, N. M. M., Langeveld, B. M. W., van Breemen, A. J. J. M. and de Kok, M. M., Advanced Materials, vol. 19, no. 9 (2007) p. 1196

[156] Scharber, M. C., Mühlbacher, D., Koppe, M., Denk, P., Waldauf, C., Heeger, A. J. and Brabec, C. J., Advanced Materials, vol. 18, no. 6 (2006) p. 789

[157] Mihailetchi, V. D., Koster, L. J. A., Blom, P. W. M., Melzer, C., de Boer, B., van Duren, J. K. J. and Janssen, R. A. J., Advanced Functional Materials, vol. 15, no. 5 (2005) p. 795

[158] Wolf, U. and Bässler, H., Applied Physics Letters, vol. 74, no. 25 (1999) p. 3848

[159] van Gennip, W. J. H., van Duren, J. K. J., Thüne, P. C., Janssen, R. A. J. and Niemantsverdriet, J. W., The Journal of Chemical Physics, vol. 117, no. 10 (2002) p. 5031

[160] Mandoc, M. M., Veurman, W., Sweelssen, J., Koetse, M. M. and Blom, P. W. M., Applied Physics Letters, vol. 91, no. 7 (2007) p. 073518-3

[161] Kim, Y., Choulis, S. A., Nelson, J., Bradley, D. D. C., Cook, S. and Durrant, J. R., Applied Physics Letters, vol. 86, no. 6 (2005) p. 063502-3

[162] de Boer, B. , Hadipour, A., Mandoc, M. M., van Woudenbergh, T. and Blom, P. W. M., Advanced Materials, vol. 17, no. 5 (2005) p. 621

[163] Raffatellu, O., thesis at the University of Cagliari, Dipartimento di Ingegneria Elettrica ed Elettronica 2007

Acknowledgment

This work was carried out within the SBO-project "Nanosolar" (IWT-030220) financed by the IWT (Instituut voor de Aanmoediging van Innovatie door Wetenschap en Technologie in Vlaanderen).

The author gratefully acknowledges Hasselt University for granting a scholarship and the PhD commission, comprising Jean Manca, Dirk Vanderzande, Ward De Ceuninck, Patrick Wagner and Laurence Lutsen for the opportunity to conduct this thesis.

Special thanks goes to Olivier Douhéret for his assiduously AFM characterisation of countless samples and his excellent work reading and correcting the draft of this work. Further, I would like to thank Olivier for the many fruitful and valuable discussions we had.

Many thanks to Vincent Mortet for trying to do Hall measurements on my samples, Bart Ruttens for performing XRD measurements, Kris Vanstreels for SEM measurements and Ineke Van Severen for providing the polymers studied in this work.

Further I woud like to thank Ward De Ceuninck and Jan Mertens for their help and expertise in the field of electrical characterisation techniques. Special thanks go to Jean-Christophe Bolsée for discussing the FET setup and lightening my workload by overtaking third-party measurement requests.

The effort of Wilfried Langenaeker (Silicos NV) to simulate the permittivity of polymers is also much appreciated.

Finally, thanks to all colleagues at Hasselt University, IMEC and IMO.